

# NAVAL POSTGRADUATE SCHOOL MONTEREY, CALIFORNIA



## THESIS

**THE EFFECT OF 300 MB DIVERGENCE  
ON  
SURFACE CYCLOGENESIS**

by

Erika Lauren Sauer

December, 1995

Thesis Advisor:

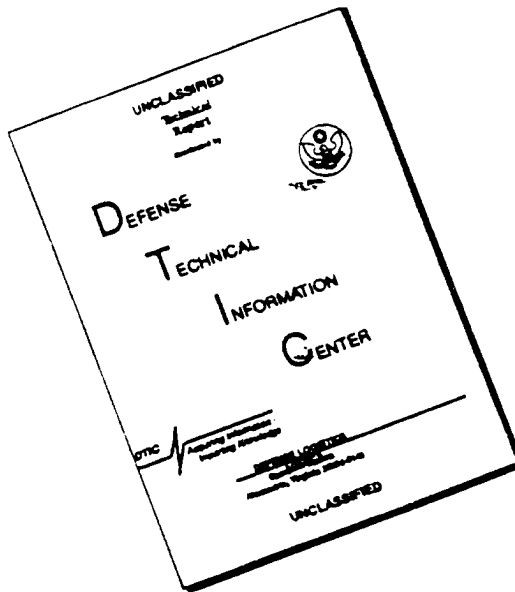
Patricia M. Pauley

Approved for public release; distribution is unlimited.

19960401 019

THIS QUALITY INFORMATION

# DISCLAIMER NOTICE



THIS DOCUMENT IS BEST QUALITY AVAILABLE. THE COPY FURNISHED TO DTIC CONTAINED A SIGNIFICANT NUMBER OF PAGES WHICH DO NOT REPRODUCE LEGIBLY.

REPORT DOCUMENTATION PAGE			Form Approved OMB No. 0704-0188	
Public reporting burden for this collection of information is estimated to average 1 hour per response, including the time for reviewing instruction, searching existing data sources, gathering and maintaining the data needed, and completing and reviewing the collection of information. Send comments regarding this burden estimate or any other aspect of this collection of information, including suggestions for reducing this burden, to Washington Headquarters Services, Directorate for Information Operations and Reports, 1215 Jefferson Davis Highway, Suite 1204, Arlington, VA 22202-4302, and to the Office of Management and Budget, Paperwork Reduction Project (0704-0188) Washington DC 20503.				
1. AGENCY USE ONLY (Leave blank)		2. REPORT DATE December 1995		3. REPORT TYPE AND DATES COVERED Master's Thesis
4. TITLE AND SUBTITLE THE EFFECT OF 300 MB DIVERGENCE ON SURFACE CYCLOGENESIS			5. FUNDING NUMBERS	
6. AUTHOR(S) Erika L. Sauer				
7. PERFORMING ORGANIZATION NAME(S) AND ADDRESS(ES) Naval Postgraduate School Monterey CA 93943-5000			8. PERFORMING ORGANIZATION REPORT NUMBER	
9. SPONSORING/MONITORING AGENCY NAME(S) AND ADDRESS(ES)			10. SPONSORING/MONITORING AGENCY REPORT NUMBER	
11. SUPPLEMENTARY NOTES The views expressed in this thesis are those of the author and do not reflect the official policy or position of the Department of Defense or the U.S. Government.				
12a. DISTRIBUTION/AVAILABILITY STATEMENT Approved for public release; distribution is unlimited.			12b. DISTRIBUTION CODE	
13. ABSTRACT (maximum 200 words) Quantitative predictions of surface extratropical cyclone development are correlated to the degree of upper-level forcing from 500 mb vorticity advection and 300 mb divergence. Although it is difficult to obtain an accurate analysis of upper-level divergence, modern models and data assimilation procedures do produce consistent divergence fields. The divergence field partitioned into the longitudinal (alongstream) and transverse (cross-stream) components approximately estimates the effect of curvature and jet streaks on cyclone intensification. Verification of the Eta model indicated not significant difference in the mean central pressure to a confidence level of 95%, and verification of the 300 mb divergence was very similar to the 500 mb vorticity advection. The presence of subgeostrophic flow in the trough and supergeostrophic flow in the ridge was noted with the longitudinal divergence. Large variability in longitudinal divergence reflected some sensitivity to small-scale perturbations in the height field. Transverse divergence showed greater consistency and projected a similar wind pattern to the classic jet streak model, however, modifications were seen as ageostrophic winds may also be directed toward regions of height falls. The composition of the total divergence from the longitudinal and transverse divergence is about 50:50. However, with very large total divergence values, the dominant contributor is the transverse divergence.				
14. SUBJECT TERMS 300 mb Divergence, Divergent Ageostrophic Wind Components, Longitudinal and Transverse Divergence			15. NUMBER OF PAGES 131	
			16. PRICE CODE	
17. SECURITY CLASSIFICATION OF REPORT Unclassified	18. SECURITY CLASSIFICATION OF THIS PAGE Unclassified	19. SECURITY CLASSIFICATION OF ABSTRACT Unclassified	20. LIMITATION OF ABSTRACT UL	

NSN 7540-01-280-5500

Standard Form 298 (Rev. 2-89)  
Prescribed by ANSI Std. Z39-18 298-102



Approved for public release; distribution is unlimited.

**THE EFFECT OF 300 MB DIVERGENCE ON SURFACE  
CYCLOGENESIS**

Erika Lauren Sauer

Lieutenant, United States Navy

B.A., Rutgers, The State University of New Jersey, 1979

M.S., University of Delaware, 1982

Submitted in partial fulfillment  
of the requirements for the degree of

**MASTER OF SCIENCE IN METEOROLOGY AND PHYSICAL  
OCEANOGRAPHY**

from the

**NAVAL POSTGRADUATE SCHOOL**

**December 1995**

Author:

*Erika L. Sauer*

Erika L. Sauer

Approved by:

*Patricia M. Pauley*

Patricia M. Pauley, Thesis Advisor

*Wendell A. Nuss*

Wendell A. Nuss, Second Reader

*Robert L. Haney*

Robert L. Haney, Chairman

Department of Meteorology



## ABSTRACT

Quantitative predictions of surface extratropical cyclone development are correlated to the degree of upper-level forcing from 500 mb vorticity advection and 300 mb divergence. Although it is difficult to obtain an accurate analysis of upper-level divergence, modern models and data assimilation procedures do produce consistent divergence fields. The divergence field partitioned into the longitudinal (alongstream) and transverse (cross-stream) components approximately estimates the effect of curvature and jet streaks on cyclone intensification. Verification of the Eta model indicated no significant difference in the mean central pressure to a confidence level of 95%, and verification of the 300 mb divergence was very similar to the 500 mb vorticity advection. The presence of subgeostrophic flow in the trough and supergeostrophic flow in the ridge was noted with the longitudinal divergence. Large variability in longitudinal divergence reflected some sensitivity to small-scale perturbations in the height field. Transverse divergence fields showed greater consistency and projected a similar wind pattern to the classic jet streak model, however, modifications were seen as ageostrophic winds may also be directed toward regions of height falls. The composition of the total divergence from the longitudinal and transverse divergence is about 50:50. However, with very large total divergence values, the dominant contributor is the transverse divergence.





## TABLE OF CONTENTS

I. INTRODUCTION .....	1
II. BACKGROUND .....	3
A. SURFACE CYCLONE DEVELOPMENT AND UPPER-LEVEL DIVERGENCE .....	3
B. PRESSURE TENDENCY EQUATION .....	4
C. THE JET STREAM AND AGEOSTROPHIC WIND PATTERNS .....	6
D. ETA MODEL PERFORMANCE .....	6
III. METHODOLOGY .....	9
A. DATA .....	9
B. CALCULATIONS .....	10
IV. RESULTS .....	15
A. CASE STUDIES .....	15
1. Surface Cyclone 216 .....	16
2. Surface Cyclone 165 .....	21
B. STATISTICS .....	26
V. CONCLUSIONS .....	33

APPENDIX .....	37
----------------	----

LIST OF REFERENCES .....	117
--------------------------	-----

INITIAL DISTRIBUTION LIST .....	119
---------------------------------	-----

## ACKNOWLEDGEMENTS

First, a special thanks to my parents, Dr. Harald and Mrs. Ellie Sauer for their endless support during my tour at the Naval Postgraduate School. Second, I want to extend my most sincere thanks to my thesis advisor and mentor, Dr. Patricia M. Pauley for sharing her knowledge and bestowing the proper guidance for the completion of this thesis. I also want to thank Dr. Wendell A. Nuss for his technical expertise pertaining to NCAR graphics and his constructive criticism as my Second Reader. Finally, a thanks is due to Bob Creasey of the Meteorology support staff for his willingness to field any computer related questions.

## I. INTRODUCTION

In its simplest form, the complex process of surface cyclogenesis can be explained by two factors: first, a column of air in the atmosphere exerts a surface pressure that results from the total mass of the air column, and second, when air is removed from the column horizontally there is a decrease in the mass of the column, which results in pressure falls and cyclogenesis. The pressure tendency equation provides a linkage between upper-level wave patterns and surface cyclone development. Falling surface pressures and an increase in low-level cyclonic circulation result from net mass divergence in the column, typically associated with divergence aloft.

Upper-tropospheric flow patterns yield divergence primarily through two mechanisms. First, the structure of upper-level troughs and ridges creates a longitudinal (i.e., parallel to the geostrophic wind) component of the ageostrophic wind that opposes the geostrophic flow in regions of cyclonic curvature and adds to the geostrophic flow in regions of anticyclonic curvature. This yields divergence between a trough and its downstream ridge and convergence between a ridge and its downstream trough. Second, the classic conceptual model of a straight jet streak portrays a transverse ageostrophic wind component, directed toward cyclonic shear in the entrance region of the jet streak and toward anticyclonic shear in the exit region. The entrance and exit region transverse ageostrophic winds accordingly yield areas of convergence in the right-front and left-rear quadrants and divergence in the left-front and right-rear quadrants. Previous research has shown that surface cyclones tend to form in the area of longitudinal divergence downstream of an upper-level trough and are

often associated with the divergent quadrants of jet streaks (i.e., Achtor and Horn 1985; Uccellini and Kocin 1987; and Uccellini 1990).

The objective of this thesis is to quantitatively examine the 300 mb divergence associated with trough-ridge wave patterns and jet streaks in the context of the forcing provided for surface cyclogenesis. To accomplish this, the 300 mb divergent ageostrophic winds computed from Eta model output are partitioned into longitudinal and transverse components to approximately isolate the impact of curvature and jet streak contributions. Model output at analysis and forecast times are used to provide a consistent estimate of divergence, which can be difficult to obtain otherwise.

To meet the stated objective, this thesis is organized as follows. Chapter II presents background information on surface cyclone development concepts, namely the relationship between divergence and surface pressure change, ageostrophic winds associated with upper-level trough-ridge patterns and jet streaks, and Eta model performance. Descriptions of the data and the computational methods used in this study are given in Chapter III. Results are presented in Chapter IV, including two limited case studies of surface cyclone development together with the evolution of associated upper-level trough-ridge and jet streak patterns, as well as a statistical analysis of the complete five-month dataset focusing on the upper-level divergent ageostrophic winds and their effects on surface cyclogenesis. Chapter V contains conclusions and recommendations.

## **II. BACKGROUND**

### **A. SURFACE CYCLONE DEVELOPMENT AND UPPER-LEVEL DIVERGENCE**

The structure and evolution of extratropical cyclones have been studied by meteorologists since the early 1900's. From the 1920's on, the polar front theory has been the accepted conceptual model for depicting the evolution of a surface cyclone from its birth as a wave on the polar front to its decay within a region of cold air (Uccellini 1990). With the advent of routine upper-air data, the existence of an upper-level wave and baroclinicity were identified in conjunction with surface cyclone development. Bjerknes and Holmboe (1944) recognized the relationship between the upper-level isobaric wave pattern and the distribution of divergence. They provided an analytical method for determining longitudinal mass divergence and calculated the level of longitudinal mass nondivergence to exist at approximately 600 mb. This calculation implied that convergence exists between the trough axis and the downstream ridge below 600 mb, and that divergence exists between the trough axis and the downstream ridge above 600 mb.

Numerous studies have verified that cyclogenesis is observed in the presence of this upper-level trough-ridge pattern and that divergence aloft accompanies convergence near the surface. Sanders and Gyakum (1980) noted that typically, when rapid cyclogenesis occurs, an upper-level trough is approximately 740 km west-southwest of the surface cyclone. Additionally, preferential development is favored downstream of a planetary wave trough, and the development is enhanced by an increase in the trough's amplitude. Uccellini (1990)

also noted that the approach of an upper-level trough toward a surface low acts to focus the mass divergence aloft and is conducive to cyclone development. Wash et al. (1991) confirmed that the presence of a well organized upper-tropospheric wave and significant upper-level divergence (properly phased with an incipient system) are crucial for surface low development.

## B. PRESSURE TENDENCY EQUATION

The theoretical link between surface cyclone development and upper-level divergence is provided by the pressure tendency equation. Following Haltiner and Martin (1957), this equation is written as

$$\frac{\partial p}{\partial t} = -V \cdot \nabla_H p - w \frac{\partial p}{\partial z} - \int_0^p \nabla_p \cdot V dp \quad . \quad (2.1)$$

If (2.1) is applied at ground level, then the second term on the right hand side vanishes, since the vertical velocity is zero at ground level. Within a closed low, the pressure advection term (the first term on the right hand side) is of minor influence. Consequently, the pressure tendency of a surface low pressure system is essentially determined by the divergence term (the third term on the right hand side), and the pressure tendency equation in pressure coordinates becomes

$$\frac{\partial p}{\partial t} = - \int_0^{p_s} \nabla_p \cdot V dp \quad . \quad (2.2)$$

The term on the left hand side, the local surface pressure change, is a direct response to the upper-level forcing, the vertically integrated divergence (the term on the right hand side). The local rate of change of pressure may be equated to the system intensification (the quasi-Lagrangian rate of change) when any one or more of the following conditions apply (Haltiner and Martin 1957):

- (i)  $V_{\text{system}} = 0$ , a stationary system;
- (ii)  $\nabla p_{\text{system}} = 0$ , in the center of a low, a high, or a col; or
- (iii)  $V_{\text{system}} \cdot \nabla p_{\text{system}} = 0$ , at a trough or ridge line.

Net mass divergence in a column centered on a surface cyclone therefore yields a negative pressure tendency, falling surface pressures, and cyclone development or deepening. The opposite is true for net mass convergence in the column, which yields a positive tendency, rising surface pressures, and filling in a surface cyclone.

The analysis of divergence is sufficiently difficult that its presence has, therefore, been traditionally inferred through the use of vorticity advection. On the synoptic scale, values of divergence are one order of magnitude smaller than vorticity and so require extreme accuracy in wind observations. The advantage of vorticity advection is that it may be estimated from the geostrophic flow assuming there is geostrophic balance. Today's greatly improved numerical models and data assimilation techniques provide consistent model output divergence fields which were used in this study.



### **C. THE JET STREAM AND AGEOSTROPHIC WIND PATTERNS**

Many studies have emphasized the role of upper-tropospheric forcing in the evolution of cyclone formation and development. Achtor and Horn (1985) noted that in the presence of a definite 300 mb jet streak, surface cyclones developed preferentially in the left-front quadrant, which coincided with upper-level divergence and positive vorticity advection. The comparison of the upper-level flow with a rapidly deepening surface low by Sanders and Gyakum (1980) showed the upper trough axis and 300 mb maximum winds to be upstream of the surface low center on the average. Upper-level forcing by mass divergence from both upper-level trough-ridge and jet streak patterns was noted in detail by Uccellini and Kocin (1987).

The components of the divergent ageostrophic wind are: longitudinal, which arises to a great extent from the upper-level trough-ridge pattern mentioned earlier (Fig. 1); and transverse, which is primarily due to acceleration and deceleration patterns within the classic straight jet streak model (Fig. 2). The presence of a longitudinal component of divergent ageostrophic wind does not necessarily imply the presence of a transverse component, and vice versa. Similarly, the relative strengths of the transverse and longitudinal components, if they exist concurrently, are not necessarily related to or dependent on each other.

### **D. ETA MODEL PERFORMANCE**

The model used in this study is the 80-km 'Early' Eta Model. This version of the Eta model solves the momentum equations on a semi-staggered Arakawa E-grid of 295 x 120

points. It has a horizontal resolution of 80 km and uses the approximately horizontal eta vertical coordinate system with 38 eta levels. A detailed model description is provided in Black et al. (1993) and summarized in Chapter III. Since the Eta model is relatively new, few studies are available which evaluate model performance.

Initially, the National Meteorological Center (NMC) verified the skill of the Eta model forecasts on the Limited-area Fine-mesh Model (LFM) grid using selected observed fields, specifically, North American rawinsonde observations (RAOBs) for height, specific humidity, temperature, wind, and precipitation. The results of these objective verifications indicated the following: 1000 mb Eta forecasts were too wet and too warm, low-level winds were too strong, mid-level heights were too low as a result of lower tropospheric temperatures being too cold, jet stream wind speeds were too low, and precipitation amounts were slightly too large (Black et al. 1993).

Colucci (1994) compared the Eta model 12 h, 24 h, 36 h, and 48 h forecasts to its own analysis and to the Nested-Grid Model (NGM) output for data collected from January through May 1994. The results showed that the Eta model tended to exhibit a positive bias in forecast cyclone central pressures and an overall cold bias in forecast thickness errors. The degree of statistical error seen in the Eta model from these studies indicates an overwhelming improvement over the LFM and a slight improvement over the NGM.



### III. METHODOLOGY

#### A. DATA

The dataset used in this study is comprised of gridded data extracted from NMC Eta model output over a five month period, from 11 January 1994 through 11 May 1994. The Eta model fields archived by NMC were interpolated to the LFM grid, which is a 53 x 45 grid point array on a polar-stereographic projection with a horizontal spacing of 190.5 km. This study used fields of sea-level pressure as well as 500 mb and 300 mb geopotential height and wind components from the initialized analysis and 12 h, 24 h, 36 h, and 48 h forecasts.

The Eta model represents NMC's current focus in terms of short-range regional modeling and subsequent forecasting guidance. Table 1 provides a brief description of the characteristics of the Eta model (Black et al. 1993).

Table 1. Basic Characteristics of the Eta Model.

Coverage Area	Forecast Length	Data Assimilation	Model Grid Characteristics	Numerical Aspects	Physical Parameterizations
Northern Hemisphere	48 hours	First guess: 6h GDAS forecast  Objective Analysis: Regional Optimum Interpolation on eta vertical coordinates	Horizontal Resolution: 80 km  Vertical Resolution: 38 levels  Grid Projection: Lambert Conformal	Semi-staggered Arakawa E grid with split-explicit time differencing	Boundary Layer: Mellor-Yamada level 2.5  Mellor-Yamada level 2 surface flux  Betts-Miller convection scheme  grid scale precipitation  Fels-Schwarzkopf radiation scheme

## B. CALCULATIONS

To assess the surface effects of the upper-level divergence, surface low pressure centers must first be identified. Colucci (1994) described in detail the procedures used to locate the surface lows comprising this study; only a brief description is given here. A sea-level pressure minimum was determined by examining the directional derivatives between a given grid point and the eight surrounding points. A cyclone was then defined as a pressure minimum seen in at least two consecutive analyses 12 hours apart. Cyclones were tracked through their life cycle by manual visual inspection of the analyses (00 h fields). The analyzed low centers were paired with the forecast lows using an objective technique based on an optimum combination of thickness at the centers of the cyclones and/or distance between the lows. The cyclones were numbered and a record of each analysis and matched forecast time was retained. Since the emphasis of this study was on extratropical systems, only lows located north of 25°N were considered.

The computation of upper-level forcing by vorticity and divergence can be performed using numerical procedures, specifically, finite differencing. To ensure the most accurate approximation of vorticity and divergence, the staggered grid, shown in Fig. 3, was utilized in this study. This required averaging the wind components from the unstaggered "p" points (model output) to the "u" and "v" points. Computations were conducted using second-order centered finite differencing in the interior of the domain, and the boundary values were obtained from the adjacent points within the array. Using a staggered grid yields the

improved treatment of the geostrophic adjustment process and the improved computation of small-scale features (Haltiner and Williams 1980).

Relative and planetary vorticity are given by

$$\zeta = m^2 \left( \frac{\partial(\frac{v}{m})}{\partial x} - \frac{\partial(\frac{u}{m})}{\partial y} \right) \quad (3.1)$$

and

$$f = 2 \Omega \sin \theta . \quad (3.2)$$

Given  $\Omega = 7.292 \times 10^{-5} \text{ s}^{-1}$ , planetary vorticity is determined from (3.2) using the latitude  $\theta$  at "p" points. Relative vorticity at "p" points is calculated from the staggered wind components, with the v-component averaged to "u" points and the u-component averaged to "v" points (Fig. 3). Advection of absolute vorticity is written as

$$- V \cdot \nabla(\zeta + f) = - m u \frac{\partial(\zeta + f)}{\partial x} - m v \frac{\partial(\zeta + f)}{\partial y} . \quad (3.3)$$

The 500 mb absolute vorticity advection was computed from (3.3) using the standard staggered winds and the absolute vorticity at "p" points. This procedure yields the first term of (3.3) at "u" points and the second term at "v" points. Both terms were averaged to "p" points and then summed to yield values of absolute vorticity advection.

Horizontal divergence is written as

$$\delta = \nabla \cdot V = m^2 \left( \frac{\partial(\frac{u}{m})}{\partial x} + \frac{\partial(\frac{v}{m})}{\partial y} \right) . \quad (3.4)$$

This can be computed from the standard staggered winds without any additional averaging.

The geostrophic wind components were computed from (3.5) and (3.6) using the staggered geopotential height fields averaged to "z" points.

$$u_g = - \frac{g}{f_o} m \left( \frac{\partial z}{\partial y} \right) \quad (3.5)$$

$$v_g = \frac{g}{f_o} m \left( \frac{\partial z}{\partial x} \right) \quad (3.6)$$

These computations yield  $u_g$  and  $v_g$  at the staggered "u" and "v" points. Once the geostrophic wind is computed, the ageostrophic wind is given merely as the difference between the analyzed/predicted ( $V_{ob}$ ) and geostrophic winds, such that

$$V_{ag} = V_{ob} - V_g . \quad (3.7)$$

In order to meaningfully examine the divergence associated with the longitudinal and transverse ageostrophic winds, the divergent component of the ageostrophic wind must first be isolated. The application of a constant Coriolis parameter renders the geostrophic wind

identically nondivergent,  $\nabla \cdot \mathbf{V}_g = 0$  (Keyser et al. 1989), therefore the divergent portion of the horizontal velocity becomes entirely ageostrophic. The divergence of the ageostrophic wind can be written following Loughie et al. (1994) in terms of a velocity potential  $\phi$  as

$$m^2 \nabla^2 \phi = \delta_{ag} \quad . \quad (3.8)$$

The ageostrophic divergence  $\delta_{ag}$  is computed from (3.4) and used to solve (3.8) for the velocity potential  $\phi$ . Utilizing Dirichlet (i.e., zero) boundary conditions the solution for  $\phi$  at the inner grid points of the array is calculated through standard sequential overrelaxation. The staggered divergent ageostrophic wind components at "u" and "v" points are then calculated from  $\phi$  by

$$u_{ag-d} = \frac{\partial \phi}{\partial x} \quad , \quad v_{ag-d} = \frac{\partial \phi}{\partial y} \quad . \quad (3.9)$$

The partitioning of the ageostrophic wind into longitudinal (along-flow direction) and transverse (cross-flow direction) components is adapted from Achtor and Horn (1985). Initially, the geostrophic and divergent ageostrophic wind components are averaged to "p" points. Then, the divergent ageostrophic wind is projected onto the geostrophic wind to resolve the longitudinal component, and onto the normal of the geostrophic wind to resolve the transverse component. Once the ageostrophic wind is partitioned, the divergence of each



component is calculated. As described by Loughé et al. (1994), partitioning the divergent ageostrophic wind rather than the total ageostrophic wind leads to divergence values which sum to the total divergence with little cancellation.

In order to statistically investigate the impact of vorticity advection, total divergence and divergence from longitudinal and transverse divergent ageostrophic winds upon the surface cyclone, an averaging box is employed. The averaging box is centered over the cyclone and encompasses a grid size of  $5 \times 5$  (approximately 762 km x 762 km). To avoid errors associated with the lateral boundaries of the domain, averages are computed only for cyclones more than two grid points away from the edges of the domain.

## **IV. RESULTS**

A set of 227 cyclone events was analyzed using the Eta model dataset described previously for the period January through May 1994. The results of this analysis are presented in terms of two detailed case studies and a statistical overview of the whole dataset. Data availability was not complete as occasional model runs were not received from NMC (Colucci 1994).

### **A. CASE STUDIES**

Two case studies, cyclones number 216 and 165, were selected for closer inspection on the basis of the total pressure change, completeness of the cyclogenetic life cycle, number of missing data runs, and geographic location. Oceanic cyclones were not considered because of uncertainty in the analysis over the oceans. The first cyclone, number 216, developed over northwestern Canada and tracked eastward to Newfoundland reaching a minimum pressure of 978 mb. The second cyclone, number 165, developed over the lower Mississippi valley and tracked northeastward along the eastern U.S. and Canada, also reaching a minimum pressure of 978 mb. Each cyclone was diagnosed to describe the synoptic environmental conditions and the upper-tropospheric forcing during their evolution. The model 00 h initialized analysis and forecast divergent fields were used for diagnosis in this section. The forecast fields showed greater consistency a point which is addressed further in the statistical analysis.

## 1. Surface Cyclone 216

The storm track for cyclone 216 (Fig. 4) extended from northwestern Canada east-southeast over the Hudson Bay and then northeast across Newfoundland. At the 1200 UTC 6 May analysis, the surface low was located over the Northwest Territories with an estimated central pressure of 1001 mb. The 12 h period of most rapid deepening began at 1200 UTC 7 May (Fig. 5), during which time the low ( $L_{12}$ ) moved toward the western Hudson Bay and deepened by 10 mb. The cyclone's minimum pressure, shown in Fig. 6, occurred at 1200 UTC 8 May, at which time the low ( $L_{18}$ ) was located over the western shores of the Hudson Bay. The support for the system weakened at this time, and the low ( $L_{19}$ ) began to gradually fill and move northeastward over Newfoundland through 0000 UTC 11 May (Fig. 7). The trace of Eta model analyzed and forecasted central pressures shown in Fig. 8 depicts the cyclone's life cycle. With increased forecast range, a trend toward larger central pressure errors was evident. However, the maximum departure of any forecast central pressure from the analysis was approximately 7 mb.

At the onset of greatest intensification (1200 UTC 7 May), the upper-level support for the system included a  $50 \text{ m s}^{-1}$  jet streak approaching the surface low ( $L_{12}$ ) at 300 mb and a shortwave trough that was passing through the longwave ridge at approximately  $120^\circ\text{W}$  (Fig. 9). The surface low at this time was under the left-front quadrant of the jet streak, a position favorable for development. Throughout the deepening period, the surface low maintained a position downstream of the shortwave trough, while the jet streak maximum increased to  $60 \text{ m s}^{-1}$  (figures not shown).

The surface cyclone reached its minimum central pressure on 1200 UTC 8 May as the shortwave trough began to come into phase with the longwave trough. At 300 mb (Fig. 10), the jet streak was greatest on the western side of the trough but extended through the base of the trough. The upper-level trough-ridge pattern showed a substantial increase in amplitude (over 10 degrees latitude) from the previous 12 h with the trough line just upstream of the surface low ( $L_{18}$ ). By 0000 UTC 11 May (Fig. 11), the 300 mb shortwave trough associated with this surface cyclone had come into phase with the trough over the eastern U.S. and rotated around it to a position on its eastern flank. A closed isobar formed nearly above the surface low ( $L_{19}$ ) making the system almost vertically stacked at this time.

The upper-level forcing for cyclones has traditionally been evaluated in terms of 500 mb vorticity advection over the surface low center. The averaged vorticity advection in the 5 x 5 grid point box centered on the surface low for the analysis and the 12 h, 24 h, 36 h, and 48 h forecasts (Fig.12) increased until 12 h prior to the time of minimum central pressure (1200 UTC 8 May). During the next 12 h an abrupt decrease occurred, followed by some variability, a slight decrease, and finally, a scant increase beginning at 1200 UTC 10 May. From the incipient stage of the surface cyclone to the mature stage, when it attained its minimum central pressure, a 500 mb shortwave trough propagated through the longwave ridge producing the steady increase in vorticity advection. Following the minimum central pressure, a reduction in vorticity advection occurred coinciding with the shortwave trough passing through the longwave trough. Except at 1200 UTC 7 May, the analyzed and predicted values of mean vorticity advection are reasonably consistent.

The details of the 500 mb vorticity advection associated with this surface cyclone are examined further in terms of horizontal fields valid at 1200 UTC 8 May, the time of minimum central pressure for the surface low. In Fig. 13, the analysis displays a maximum of vorticity advection downstream of the shortwave trough and a minimum upstream, as expected. The averaging box positioned over the surface low ( $L_{18}$ ) therefore, included both positive and negative values yielding a cyclone mean vorticity advection of only  $0.34 \times 10^{-9} \text{ s}^{-2}$ . The 500 mb vorticity advection in the 12 h forecast showed a similar pattern (Fig. 14) with a cyclone mean of  $2.0 \times 10^{-9} \text{ s}^{-2}$ . However, the position of the averaging box for the 24 h and 36 h forecasts, Figs. 15 and 16 respectively, included a smaller region of negative vorticity advection and so had cyclone averages of  $6.6 \times 10^{-9} \text{ s}^{-2}$  and  $4.0 \times 10^{-9} \text{ s}^{-2}$ , respectively. By comparison, the 48 h forecast portrayed little negative vorticity upstream of the trough and had the averaging box encompassing a vorticity advection maximum, resulting in a cyclone average of  $10.5 \times 10^{-9} \text{ s}^{-2}$ .

The 500 mb shortwave trough near  $95^\circ\text{W}$  is asymmetric with a larger wavelength ridge upstream and a shorter wavelength ridge downstream of the trough evident in the analysis and the forecasts. A shorter wavelength yields a tighter gradient and greater vorticity as seen in the 24 h (Fig. 15) and 48 h (Fig. 17) forecasts indicating nearly a closed isobar and much larger averaged vorticity advection than the analysis and the 12 h and 36 h forecasts.

Rather than vorticity advection, this thesis focuses more on 300 mb divergence as a measure of the upper-level forcing for the surface cyclone. Although, some variation in the

cyclone-average total divergence is apparent in Fig. 18, an increase prior to the time of minimum central pressure (1200 UTC 8 May) and a decrease following it is evident. At 1200 UTC 8 May, approximately half of the total divergence maximum northeast of the surface low was located within the averaging box (Fig. 19). This yielded the largest value of total divergence found throughout the life cycle of the cyclone, as indicated in Fig. 18. In the 12 h forecast (Fig. 20), the total divergence maximum was similar in magnitude to the analysis, however, it shifted slightly to the east producing reduced averaged total divergence. In Fig. 21, the 24 h forecast showed the magnitude of the maximum total divergence on the eastern edge of the averaging box decreased by almost half compared to the analysis and the 12 h forecast. Still, the averaged total divergence value decreases only slightly, since the area within the averaging box covered by the maximum total divergence is larger. The 36 h and 48 h forecasts, Figs. 22 and 23 respectively, show similar configurations as the 24 h forecast in that there is a decrease in the magnitude of the maximum total divergence, but an increase in the area within the averaging box covered by the maximum total divergence resulting in a slight reduction in the cyclone-averaged total divergence.

The sensitivity of the cyclone-average longitudinal divergence to variations in the 300 mb trough is reflected in Fig. 24. Despite the vacillation, there was a general increase before the time of minimum central pressure and a general decrease afterwards in the analysis and the forecasts. The details of the analysis and each of the forecasts valid at 1200 UTC 8 May supported the concept of supergeostrophic flow in the ridge and subgeostrophic flow in the trough associated with the longitudinal component of the divergent ageostrophic

wind (Figs. 25, 26, 27, 28, and 29). In Fig. 25, a sharp ridge downstream and a tight gradient near the low ( $L_{18}$ ) coincides with the maximum longitudinal divergence just east of the averaging box producing the largest value of longitudinal divergence at 1200 UTC 8 May. The 12 h forecast exhibits a resemblance to the analysis pattern with the maximum longitudinal divergence located just to the east of the averaging box (Fig. 26) and similar cyclone-averaged longitudinal divergence (Fig. 24). The 24 h forecast (Fig. 27) has a mean longitudinal divergence which is similar to the 12 h forecast, however, the maximum longitudinal divergence magnitude is less than the 12 h forecast and it is located almost completely within the averaging box. The 36 h and 48 h forecasts (Figs. 28 and 29, respectively) show the maximum longitudinal divergence is less than the analysis and other forecasts and is located west and southwest, respectively. The analysis and 12 h forecast show the strongest supergeostrophic flow in the downstream ridge which correspond well with large longitudinal divergence evident in Fig. 24.

The cyclone-averaged transverse divergence depicted in Fig. 30 showed more consistent values than the longitudinal divergence. A steady increase was present prior to 1200 UTC 8 May, and thereafter, a decline until 1200 UTC 9 May followed by a smaller increase. During the increase, the surface low remained in the left-front quadrant of the upstream jet streak and following 1200 UTC 8 May, the time of minimum central pressure, the position of the low was further downstream of the jet streak. Flow toward the cyclonic-shear side of the jet in the entrance and flow toward the anticyclonic-shear side of the jet in the exit region was evident in the analysis and each of the forecasts. The 1200 UTC 8 May

analysis (Fig. 31) shows a maximum transverse divergence located directly within the averaging box with a relatively high magnitude producing the largest value depicted on Fig. 30. In Fig. 32, the 12 h forecast maximum transverse divergence has shifted to the southeast and has a slightly reduced magnitude leading to a decreased averaged transverse divergence. The magnitude and position (centered over the low,  $L_{18}$ ) of the maximum transverse divergence in Fig. 33 support the large averaged transverse divergence present. The 36 h (Fig. 34) and 48 h (Fig. 35) forecasts indicate the maximum transverse divergence is shifted to the west which is reflected in the decreased values evident in Fig. 30.

In summary, throughout the life cycle of this cyclone, upper-level forcing as shown by either positive vorticity advection or divergence was reflected at the surface by the change in central pressure. As expected, where large values of positive vorticity advection and divergence were prevalent, there was a negative pressure tendency at the surface. The opposite case was true when small values of positive vorticity advection and divergence were evident, then there was a positive surface pressure tendency. Cyclone 216 was consistent with the Petterssen development equation in terms of vorticity advection and the pressure tendency equation for divergence to provide the upper-level forcing for surface cyclone development.

## **2. Surface Cyclone 165**

The storm track for cyclone 165 is shown in Fig. 36. In contrast to cyclone 216, this cyclone developed over northern Louisiana and moved northeast over the eastern U.S. and Canada, across the Gulf of St. Lawrence, and then south of Greenland where it began to



dissipate. The 0000 UTC 6 April chart showed the low ( $L_{18}$ ) to have a central pressure of 1004 mb over the border between Arkansas and Louisiana as seen in Fig. 37. During the next 36 h the central sea-level pressure of the cyclone remained approximately the same. However, by 1200 UTC 7 April (Fig. 38) the circulation had increased, the system ( $L_{20}$ ) was more organized, and the initial stage of deepening began even though the central pressure was essentially the same. Thereafter, the deepening rate maintained a steady fall to reach a minimum central pressure of 978 mb on 1200 UTC 9 April (Fig. 39) when the low ( $L_{21}$ ) was south of Greenland near  $50^{\circ}\text{W}$ . Following this period, a gradual rise in the central pressure was indicated in Fig. 40. This figure also illustrated the similarity in the central pressures for the analysis and the forecasts, however, analogous to cyclone 216, the mean central pressure error increased with increasing forecast range.

The 300 mb height/isotach analysis at 0000 UTC 6 April (Fig. 41) indicated the surface low ( $L_{18}$ ) was positioned in the right-front quadrant of a  $50 \text{ m s}^{-1}$  jet streak a quadrant where convergence aloft would be expected. The surface low positioning remained relatively the same with respect to the jet streak through the following 24 h, however, the jet streak increased in speed ( $> 60 \text{ m s}^{-1}$ ) chart not shown. As shown in Fig. 42 by 1200 UTC 7 April, the upper-level trough slightly increased in amplitude and moved to within 1110 km of the surface low position. The jet streak elongated, reduced in speed ( $> 50 \text{ m s}^{-1}$ ), and was directly over the surface low ( $L_{20}$ ). The cyclone deepened to its minimum central pressure over the next 48 h while the trough (Fig. 43) amplified and the jet streak increased to greater than  $60 \text{ m s}^{-1}$  upstream of the surface low ( $L_{21}$ ). It was in a favorable location for upper-level

support from the upstream longwave trough and its position under the left-front quadrant of the jet streak. Following this period, the surface low began to lose upper-level support as the trough weakened and overtook the surface cyclone.

An examination of the sequence of cyclone-averaged vorticity advection (Fig. 44) for the analysis and forecasts revealed greater variability from 0000 UTC 6 April to its initial deepening phase 1200 UTC 7 April. Thereafter, nearly constant values existed during the next 48 h at which time the minimum central pressure occurred. Specifically, the cyclone-average positive vorticity advection during the period of intensification remained high with values greater than approximately  $12 \times 10^{-9} \text{ s}^{-2}$ .

The details of the variability in cyclone-average vorticity advection at 1200 UTC 7 April are examined in terms of the horizontal distribution of vorticity advection at 500 mb. Fig. 45 shows the 500 mb vorticity advection maximum ahead of the trough axis near  $80^\circ\text{W}$  in the vicinity of the surface low as would be expected. However, a small negative maximum is present just downstream of the surface low ( $L_{20}$ ), that does not seem to be associated with any distinctive feature in the height field. The effects from both positive and negative vorticity advection were evident within the averaging box over the low resulting in a vorticity advection value of  $16.8 \times 10^{-9} \text{ s}^{-2}$  at this time. The magnitude of the maximum vorticity advection for the 12 h forecast in Fig. 46, was significantly less than the analysis, however, a significant amount was still within the averaging box. The 24 h forecast maximum vorticity advection was also less than the analysis and the position of the surface low ( $L_{17}$ ) was considerably further from the 500 mb trough axis (Fig. 47). In Fig. 48, the

maximum vorticity advection for the 36 h forecast is shifted south compared to the analysis, although the magnitude is similar. Of particular interest, Fig. 49 shows the 48 h forecast with a sizable section of the averaging box under a maximum negative vorticity advection resulting in the minimum vorticity advection value shown in Fig. 44.

The cyclone-averaged total divergence values found in Fig. 50 were also quite variable, particularly throughout the development stage of the cyclone. A decrease was apparent, however, following the time of minimum central pressure (1200 UTC 9 April) for the analysis and each of the forecasts. On 1200 UTC 7 April (Fig. 51) during the intensification of the cyclone, a divergence maximum was located directly over the low and produced a large cyclone-average total divergence for the analysis. Both the 12 h (Fig. 52) and 24 h (Fig. 53) forecasts valid at 1200 UTC 7 April depicted the maximum divergence northeast of the surface low with smaller values in the averaging box and reduced mean values. As depicted in Fig. 54, the 36 h forecast showed maximum divergence south of the averaging box, but produced a mean value comparable to the analysis. The 48 h forecast (Fig. 55) differed considerably from the others, with convergence in a sizable fraction of the averaging box countering the divergence also present and giving the lowest total divergence compared to the analysis and other forecasts.

The large variability present in the total divergence was also evident in the cyclone-average longitudinal divergence (Fig. 56), supporting the sensitivity of longitudinal divergence to the position of the upper-level trough axis relative to the surface low. In the analysis for 1200 UTC 7 April (Fig. 57), subgeostrophic flow was apparent in the trough

located near  $83^{\circ}\text{W}$ , and likewise, supergeostrophic flow was analyzed in the ridge near  $105^{\circ}\text{W}$ . All the forecasts supported similar subgeostrophic and supergeostrophic flow associated with the trough and ridge pattern. The analysis, 12 h forecast and 24 h forecast valid at 1200 UTC 7 April showed parallel averaged longitudinal divergence values and longitudinal vectors opposing the geostrophic flow. In the 12 h forecast, Fig. 58, the maximum longitudinal divergence is located west of the averaging box. Figure 59, the 24 h forecast, depicts the maximum longitudinal divergence southwest of the averaging box with a slightly lower magnitude than the 12 h forecast, yet the value of the vectors are slightly larger than the 12 h forecast. The longitudinal vectors in the 36 h forecast (Fig. 60) flow with the geostrophic wind, which is in the opposite direction from the analysis, 12 h forecast and 24 h forecast. The averaging box includes a significantly greater portion of the maximum longitudinal divergence than the 12 h and 24 h forecasts and is more similar to the analysis. A convergent maximum is located within the averaging box and the maximum longitudinal divergence is further to the southwest than in any other chart. The 48 h forecast (Fig. 61) displays converging longitudinal vectors and the distance of the maximum longitudinal divergence to the averaging box is significantly further than the analysis and any other forecasts.

The transverse divergence produced a much more consistent trace, overall larger cyclone-average divergence values, and a general decreasing trend throughout the cyclone's life cycle (Fig. 62). The analysis (Fig. 63) and 12 h forecast (Fig. 64) both show a maximum transverse divergence north and south-southeast of the averaging box with a similar

transverse vector pattern. The 24 h forecast also has maximum transverse divergence north and south-southeast of the averaging box, however, the transverse vectors are less and indicate opposite flow (Fig. 65). For Fig. 66, the distance of the two maximum transverse divergent areas to the averaging box is decreased and the vectors are relatively large supporting the largest cyclone-average by the 36 h forecast. The 48 h forecast (Fig. 67) indicates that the maximum transverse divergence falls within the averaging box and one area located much further south of the averaging box. Although, the classic jet streak concept and associated transverse component is not readily seen in these charts, the vector pattern does correspond to an alongstream wind speed gradient evident in the isotach analysis not shown.

As expected, the upper-level forcing identified in cyclone 165 was similar to the findings in cyclone 216. Cyclone intensification may be correlated to large values of 500 mb positive vorticity advection and 300 mb divergence and described as a negative pressure tendency at the surface.

## **B. STATISTICS**

A population of 227 cyclones comprised the statistical data base for this study. The Eta model performance was evaluated statistically using central pressure, central pressure error, predicted 12 h central pressure change, 500 mb vorticity advection, and 300 mb divergence. A comparison between the model initialized analysis (00 h) and the 12 h, 24 h, 36 h, and 48 h forecasts was conducted for each of the parameters mentioned above. The

correlation coefficient was used to quantify the degree of linear fit between the analysis and each of the forecasts. The Student's t-test was utilized to compare the two separate populations and to test whether the difference in their means was significant to a 95% confidence level.

Verification of the central pressure with each of the forecasts shows that good agreement exists between the forecasts and the initialized analysis (Fig. 68). The correlation coefficients were all quite high, ranging from 0.98 for the 12 h to 0.89 for the 48 h. The least-squares line in all four cases had a slope near one and an intercept near zero (i.e., the perfect linear fit is quantified by the dashed diagonal), implying little bias in the forecast values. The t-test showed no significant difference between the mean analyzed central pressure and each mean forecasted central pressure to a 95% confidence level. This also demonstrates that the forecast central pressures have essentially no bias. In order to further investigate the performance of the model in predicting central pressure, the central pressure error was examined. In Figs. 69 a and b, histograms of the 12 h and 48 h forecast central pressure errors, respectively, appear to have a near normal distribution with a mean near zero, but with a standard deviation (SD) that increases substantially from 2.66 at 12 h to 5.97 at 48 h. This increasing standard deviation can be seen in Fig. 68 as increasing scatter about the diagonal line that would result if all forecasts were perfect.

However, the predicted change in central pressure, a measure of the intensification rate for the surface cyclone, is of more interest in the present study than central pressure itself. The correlation coefficient between the analyzed and predicted 12 h central pressure

change ranged from 0.91 for the 12 h forecast to 0.75 for the 48 h forecast (Fig. 70), indicating a relatively good linear fit. The Student's t-test showed that the mean predicted central pressure change was not significantly different from the mean analyzed central pressure change at all forecast ranges at a 95% confidence level. However, the slope of the least squares line ranges from 0.83 for the 12 h forecast to 0.67 for the 48 h forecast, which suggests that the forecasts systematically underestimate the magnitude of the central pressure change.

Examining the 500 mb cyclone-average vorticity advection shown in Fig. 71, the correlation coefficient ranged between 0.77 and 0.59 for the 12 h and 48 h forecasts, respectively, demonstrating a weaker linear fit than in the previous parameters. Statistically, the model did not show any significant difference between the mean analyzed and forecasted vorticity advection. As with the previous parameters, the slope of the least square line decreased from 0.77 to 0.55 between the 12 h and the 48 h forecasts implying the forecasts systematically underestimate the vorticity advection. The decrease in linear fit with an increase in forecast range showed the expected decline in forecast accuracy with increased forecast range.

The 300 mb cyclone-average total divergence model verification (Fig. 72) showed a correlation coefficient range of 0.77 for the 12 h to 0.59 for the 48 h forecasts similar to the vorticity advection. The slope of the least square line decreased from 0.70 to 0.48 for the 12 h to the 48 h forecasts indicating an underestimation in the forecasts of the total divergence. As with the vorticity advection, the total divergence showed a decrease in linear fit related

to reduction in forecast accuracy with increased forecast time. Overall, the 300 mb divergence was very similar to the vorticity advection and may also be useful in predicting surface pressure changes.

The model verification for cyclone-average longitudinal divergence (Fig. 73) and transverse divergence (Fig. 74) showed the correlation coefficients were similar to the total divergence. Of particular interest was the difference in the range between the two components. The longitudinal divergence correlation coefficient at the 12 h forecast had a value of 0.71 and at the 48 h forecast a value of 0.49. Whereas, the transverse divergence correlation coefficient at the 12 h forecast had a value of 0.73 and at the 48 h forecast a value of 0.58. Quantitatively, the longitudinal divergence varied substantially more than the transverse divergence. These same results were also found in each of the two case studies. Specifically, cyclone 165 (Figs. 57, 58, 59, 60, and 61) showed small scale perturbations in the 300 mb height field over the surface low at 1200 UTC 7 April, which was reflected in the longitudinal divergence by large variability including a negative value in the trace at the 48 h forecast (Fig. 56).

In addition to verifying how well the Eta model performed in predicting these various quantities, the 227-cyclone database was also used to examine the relationship between the upper-level forcing and the development of the surface cyclone. Vorticity advection compared with the predicted 12 h central pressure change (Fig. 75) did not reflect a very high correlation. Although, the correlation coefficient value was not very high, it was relatively consistent ranging from 0.42 to 0.54. The slope of the least squares fit line indicated that



with positive vorticity advection there was a negative pressure tendency and with negative vorticity advection there was a positive pressure tendency as expected. The poor correlation may be explained in terms of the Petterssen development equation stating surface pressure change results from forcing by upper-level vorticity advection and additional factors such as thickness advection, stability, and surface fluxes which were not considered here.

The total divergence compared to the predicted 12 h central pressure change (Fig. 76) also did not correlate well with correlation coefficients ranging from 0.42 to 0.50. The linear fit did indicate that with divergence there was a negative pressure tendency and with convergence there was a positive pressure tendency. However, note that surface pressure change is really a function of the vertically integrated divergence through the whole column of air above the cyclone. Here the comparison was only a function of one level, the 300 mb level.

Figure 77 illustrates the comparison between total divergence and vorticity advection. The correlation coefficient ranges from 0.56 for the 12 h forecast to 0.72 for the 48 h forecast which is substantially improved over the comparison between these parameters and the 12 h predicted pressure change. As expected, however, a positive correlation existed between positive vorticity advection which corresponded to divergence and negative vorticity advection which corresponded to negative divergence or convergence. Interestingly, the correlation coefficient increased as the forecast range increased indicating greater consistency in the forecasted divergence compared to the analyzed divergence.

Using the 24 h forecast divergence, a comparison of the longitudinal and transverse components of divergence was evaluated. Figure 78 shows the ratio of the 24 h forecast transverse to total divergence plotted against the 24 h forecast total divergence. A domination of the total divergence by the transverse component is evidenced by a ratio greater than 0.50; a domination by the longitudinal component is evidenced by a ratio less than 0.50. The plots on Fig. 78 are approximately symmetric about a ratio of 0.50. Consequently, the contribution by those values less than 0.50 is predominantly the longitudinal component, and the contribution by those values greater than 0.50 is predominantly the transverse component. Values between the ratios of 0.00 and 1.00 indicate that the longitudinal and transverse components have the same sign. Values less than 0.00 indicate there is some cancellation and the longitudinal component is larger and of the opposite sign than the transverse component. Conversely, values greater than 1.00 indicate that the transverse component is larger and of the opposite sign than the longitudinal component. For total divergence values falling between -100 and 100 and for ratios of 0.00 and 1.00, any combination of longitudinal and transverse divergence is contributing to the total divergence. Since the majority of the plots fall between total divergence values of 100 and 200 and ratios of 0.25 and 0.75, both components are contributing to the total divergence. Those few plots between the large total divergence values of 200 and 300 and ratios of 0.50 and 0.75 imply the major contributor to the total divergence is the transverse component. In Fig. 79, the histogram of the ratio of the 24 h forecast transverse to the total divergence indicates a relative normal distribution with the greatest number of values

between 0.0 (left line) and 1.0 (right line). The mean of the transverse to total divergence ratio equals 0.48 (center line) and a near normal distribution exists, so the contribution by the longitudinal and transverse components are very similar. To obtain ratios greater than 1.00, a cancellation must occur and the longitudinal divergence is smaller and of opposite sign than the transverse divergence. Likewise, for ratios less than 0.00, a cancellation occurs and the transverse divergence is smaller and of opposite sign than the longitudinal divergence.

## V. CONCLUSIONS

This study quantitatively examined 300 mb divergence and its effect on surface cyclones. Simplistically, from the Petterssen development equation, surface pressure change is a response to forcing from mid-tropospheric vorticity advection along with several other factors. However, surface pressure change can be expressed in terms of the vertically integrated mass divergence in a column of air above the surface cyclone. Using the pressure tendency equation, net divergence in the column of air is reflected at the surface by a decrease in pressure. The small magnitude of divergence is such that accurate estimation of divergence is difficult using traditional methods; however, with today's models and data assimilation capabilities the accuracy of estimated divergent fields has significantly improved.

Divergence aloft is produced from ageostrophic winds generated by subgeostrophic and supergeostrophic flow within trough-ridge patterns and by acceleration and deceleration in the entrance and exit regions of jet streaks. The role of upper-level divergence in cyclone intensification has been investigated in studies completed by Uccellini and Kocin (1987), Sanders and Gyakum (1980) and others. The divergent ageostrophic wind components were computed from  $\phi$  ( $\Phi$ ), the velocity potential, calculated from the divergence of the ageostrophic wind. Decomposition into the longitudinal and transverse components of the ageostrophic wind was accomplished by projecting the divergent ageostrophic wind correspondingly in the along and normal directions to the geostrophic flow. Diagnosing the

contribution from both these sources of 300 mb divergence is evaluated in two limited case studies and the complete dataset of 227 cyclones using Eta model output from January through May 1994.

The Eta model verification showed no significant difference in the mean central pressure for the analysis and the forecasts to a 95% confidence level. The standard deviation of the mean central pressure error did indicate a decrease in forecast skill with increasing forecast range. Although, the correlation coefficients for 500 mb vorticity advection and 300 mb divergence were not high, model verification was very similar. The reduced linear fit of vorticity advection is an indication of other physical factors involved as stated in the Petterssen development equation. The less correlated divergence is related to the total divergence being a function of the vertical integration of the whole column of air above a surface cyclone and not just one level (300 mb).

The fundamental characteristic of longitudinal divergence generated by subgeostrophic flow in the trough and supergeostrophic flow in the ridge was evident in both case studies, cyclones 216 and 165. Large variability was evident in the longitudinal divergence showing sensitivity associated with small perturbations in the height field. The transverse divergence classic jet streak model pattern was modified somewhat by the fact that the ageostrophic wind does also point toward areas of falling heights as evidenced in both case studies.

The ratio of transverse to longitudinal divergence comprising the total divergence was approximately 50:50 for most values. However, when the magnitude of total divergence

was relatively large ( $> 200 \times 10^{-6} \text{ s}^{-1}$ ) the dominant contribution was found to be the transverse divergence component.



## APPENDIX

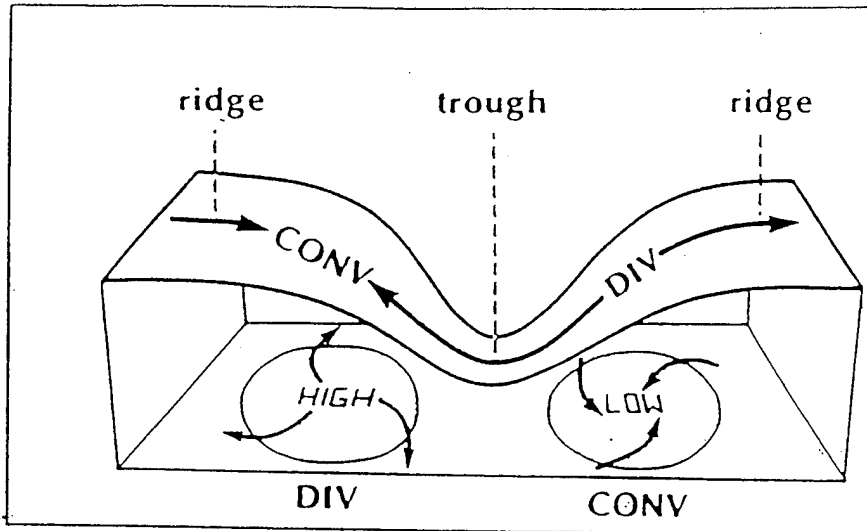


**Figure 1.** Schematic relating the along-stream ageostrophic wind at upper levels to patterns of divergence associated with an upper-level wave. (From Uccellini 1990)

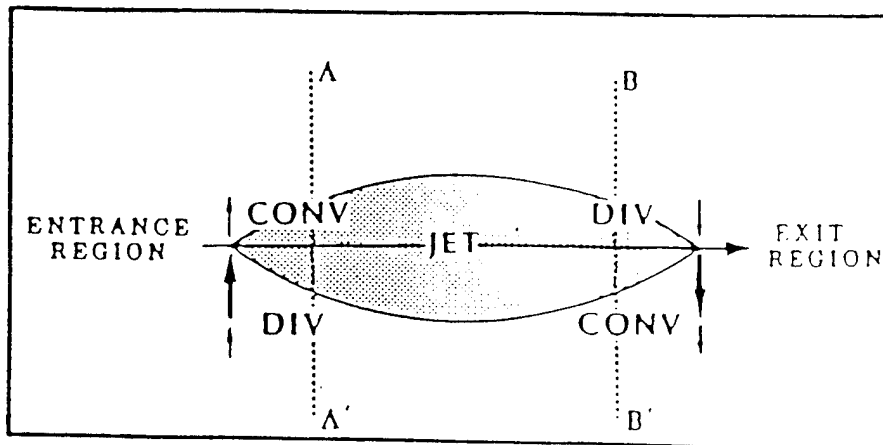
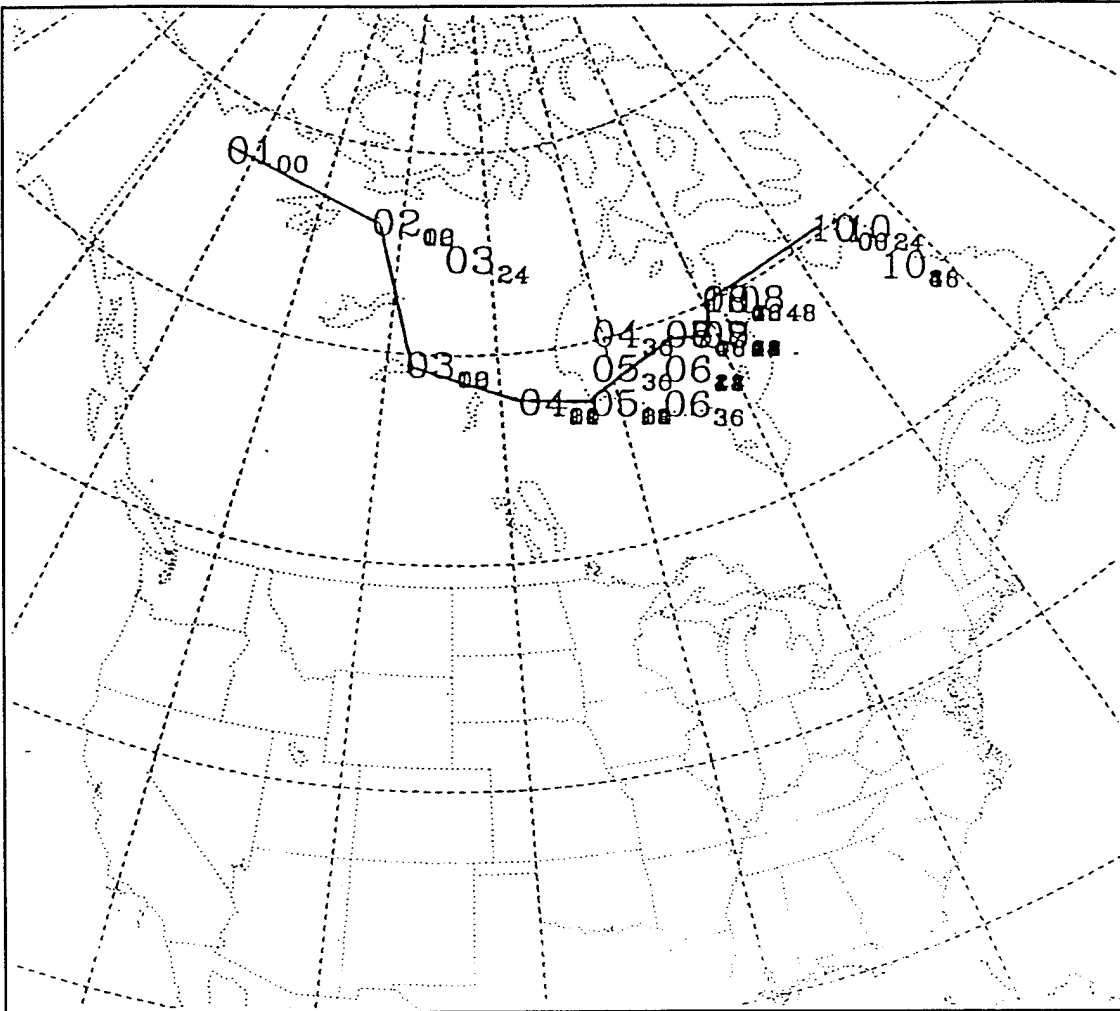


**Figure 2.** Schematic of transverse ageostrophic wind components and patterns of divergence associated with the entrance and exit regions of a straight jet streak. (From Uccellini and Kocin 1987)

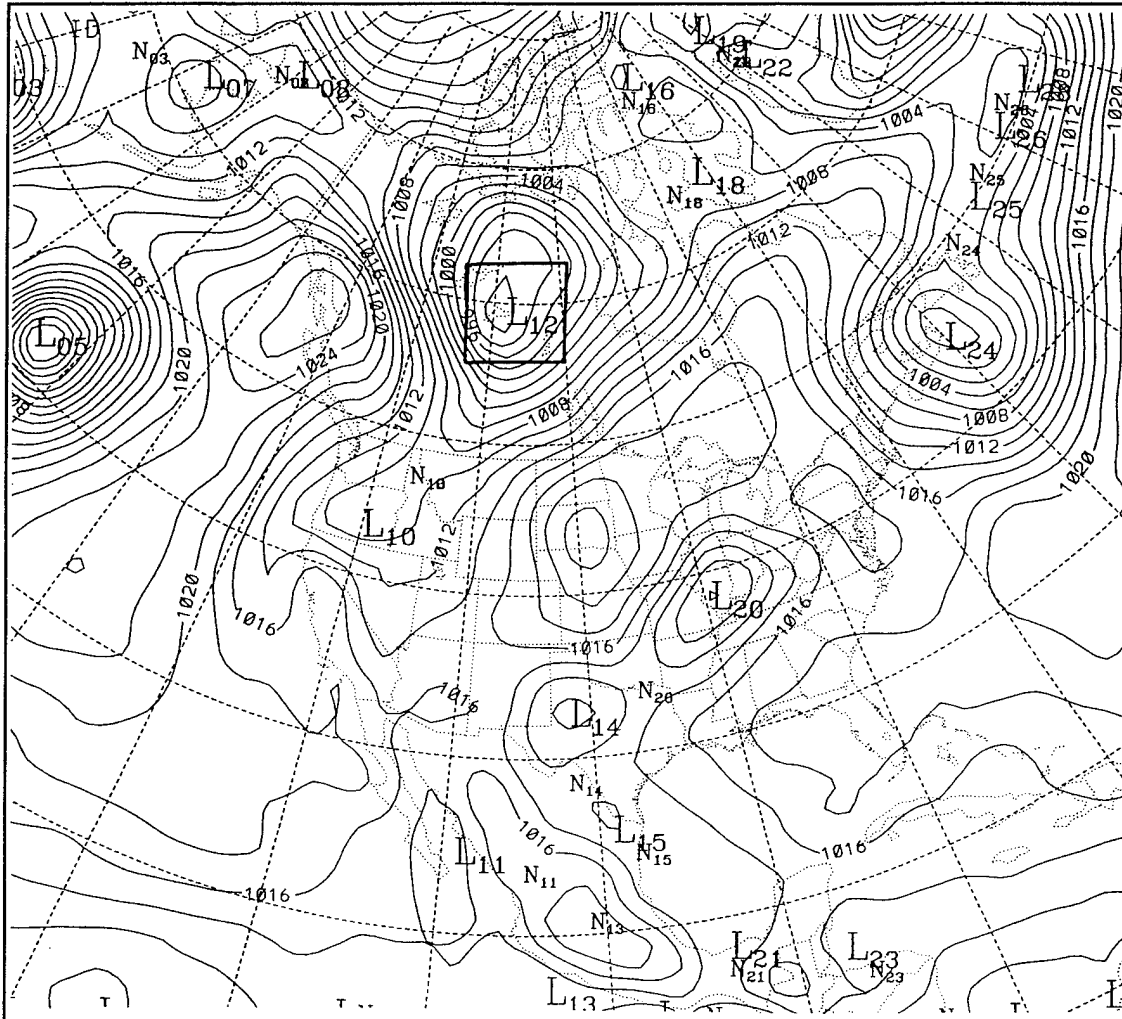


<b>p</b> $(i-1,j+1)$	<b>u</b> $(i-1,j+1)$	<b>p</b> $(i,j+1)$	<b>u</b> $(i,j+1)$	<b>p</b> $(i+1,j+1)$
<b>v</b> $(i-1,j)$	<b>z</b> $(i-1,j)$	<b>v</b> $(i,j)$	<b>z</b> $(i,j)$	<b>v</b> $(i+1,j)$
<b>p</b> $(i-1,j)$	<b>u</b> $(i-1,j)$	<b>p</b> $(i,j)$	<b>u</b> $(i,j)$	<b>p</b> $(i+1,j)$
<b>v</b> $(i-1,j-1)$	<b>z</b> $(i-1,j-1)$	<b>v</b> $(i,j-1)$	<b>z</b> $(i,j-1)$	<b>v</b> $(i+1,j-1)$
<b>p</b> $(i-1,j-1)$	<b>u</b> $(i-1,j-1)$	<b>p</b> $(i,j-1)$	<b>u</b> $(i,j-1)$	<b>p</b> $(i+1,j-1)$

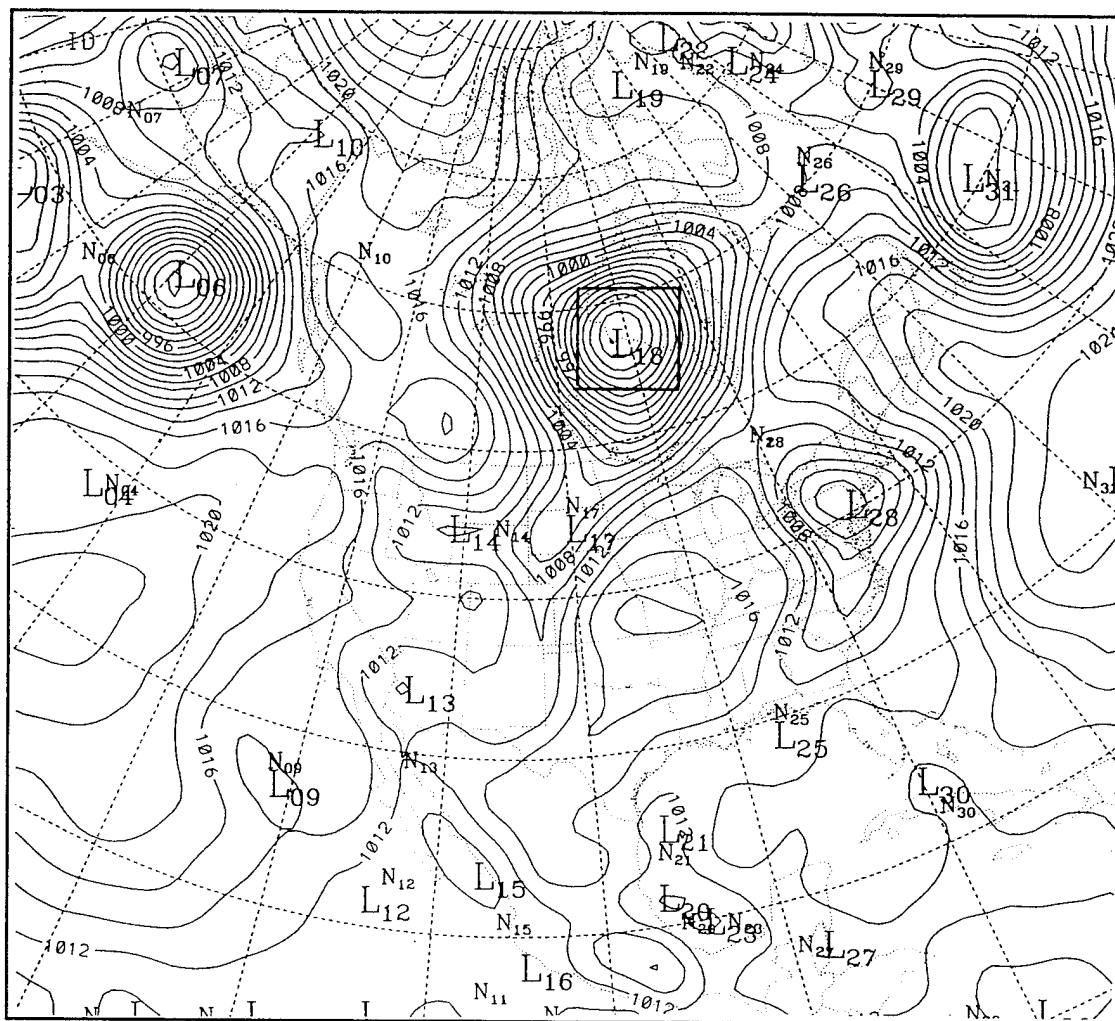
Figure 3. Staggered grid used for computations.



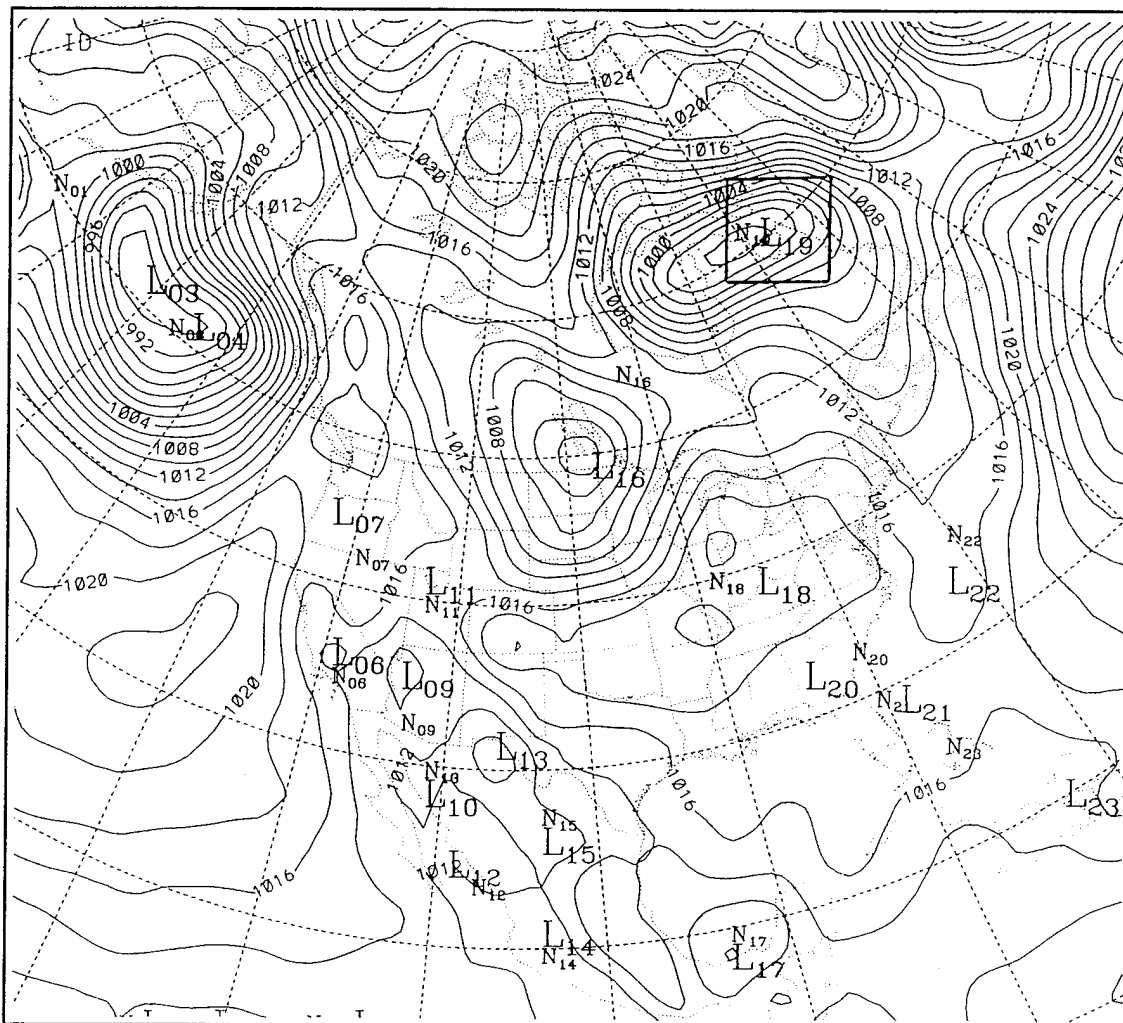
**Figure 4.** The 12-hourly surface cyclone center positions from the Eta model analysis (subscript 00) and forecasts at 12 h (subscript 12), 24 h (subscript 24), 36 h (subscript 36), and 48 h (subscript 48) between 1200 UTC 6 May (large 01) and 1200 UTC 11 May 1994 (large 10).



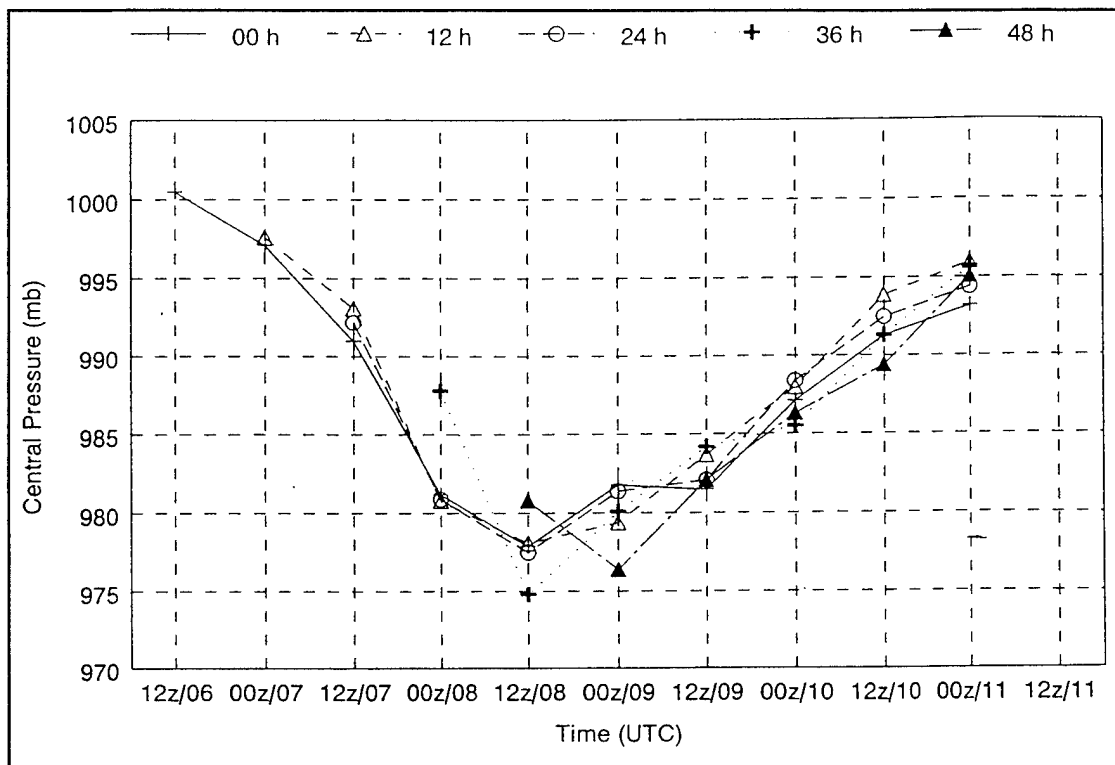
**Figure 5.** Eta model surface pressure (solid, 2 mb increment) analysis for 1200 UTC 7 May 1994. A 5 x 5 grid point averaging box is centered over the cyclone of interest labeled L<sub>12</sub>.



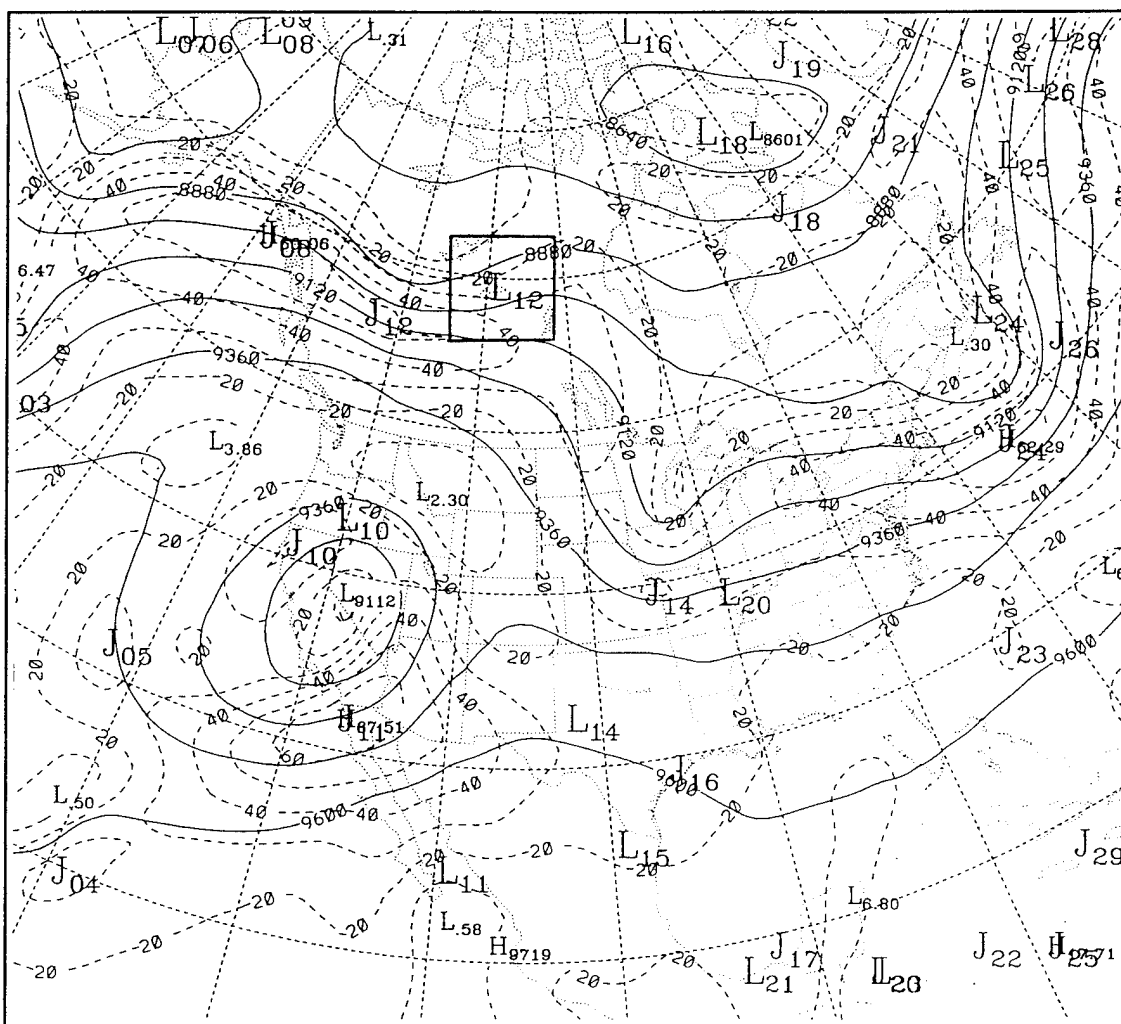
**Figure 6.** As in Figure 5, except for 1200 UTC 8 May 1994 and the cyclone of interest is labeled L<sub>18</sub>.



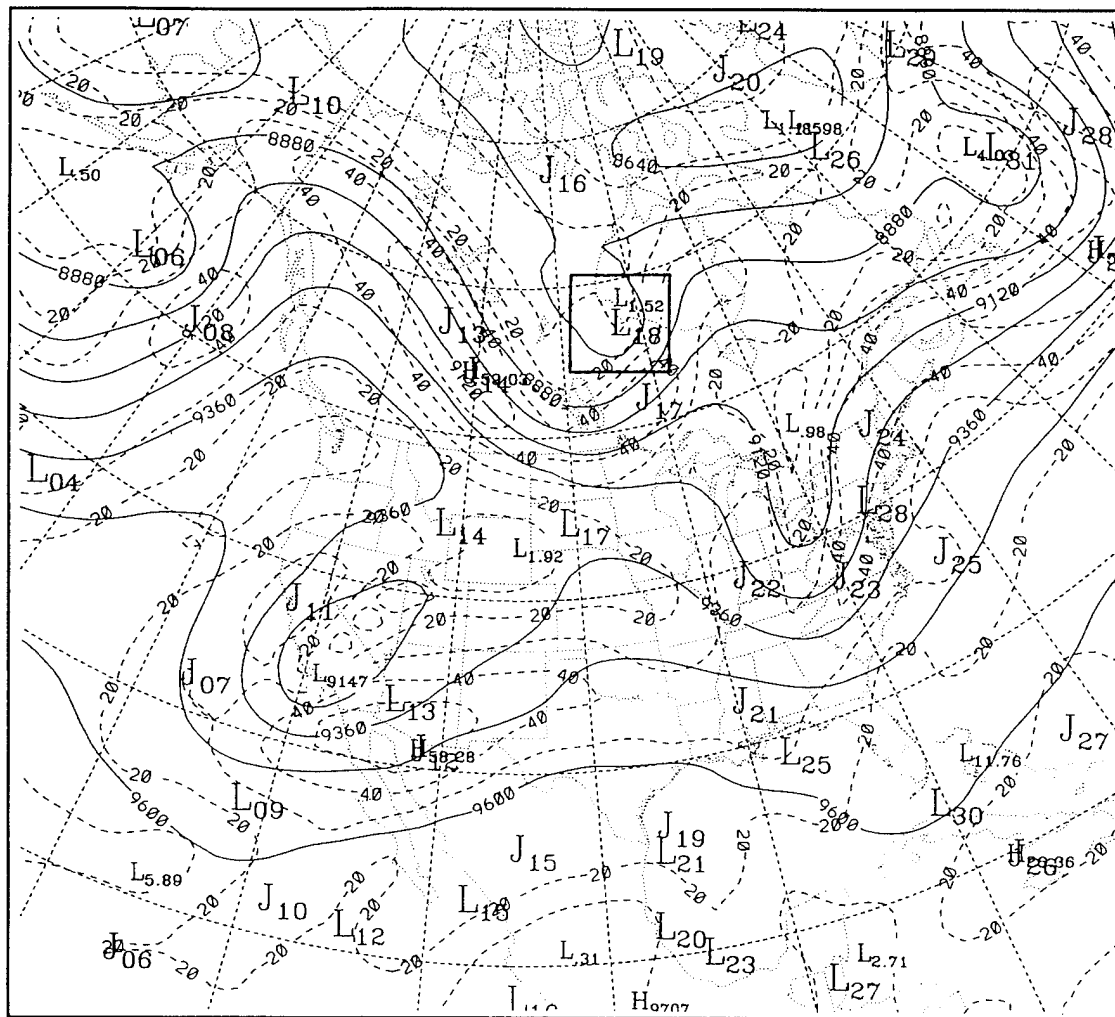
**Figure 7.** As in Figure 5, except for 1200 UTC 11 May 1994 and the cyclone of interest is labeled  $L_{19}$ .



**Figure 8.** Cyclone 216 central pressure trace from 1200 UTC 6 May (12Z/06) to 0000 UTC 11 May 1994 (00Z/11).



**Figure 9.** Eta model 300 mb height analysis (solid, 12 dm increment) and windspeed (dashed, 10 m/s increment) for 1200 UTC 7 May 1994. A 5 x 5 grid point averaging box is centered over the cyclone labeled L<sub>12</sub>.





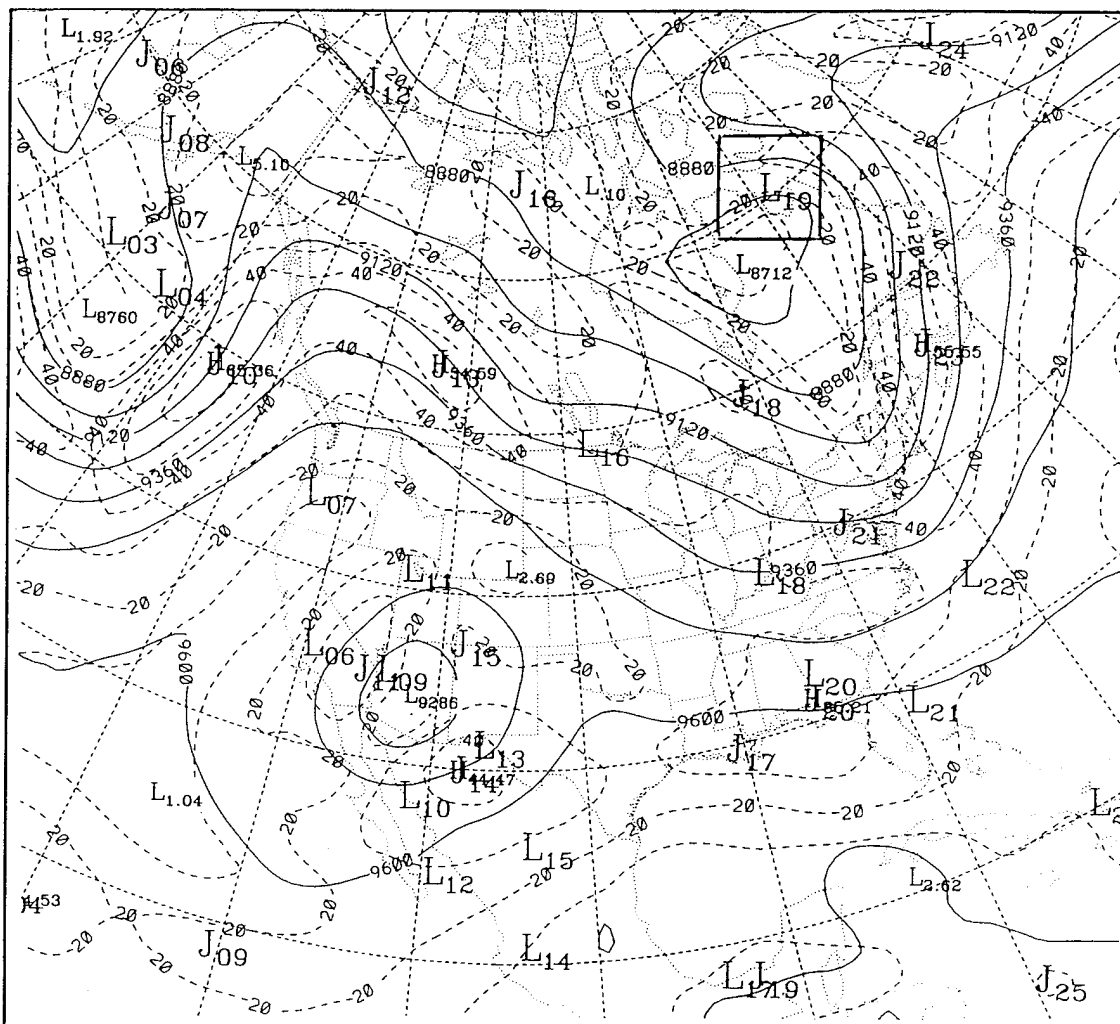


**Figure 11.** As in Figure 9, except for 1200 UTC 11 May 1994 and the cyclone of interest is labeled L<sub>19</sub>.

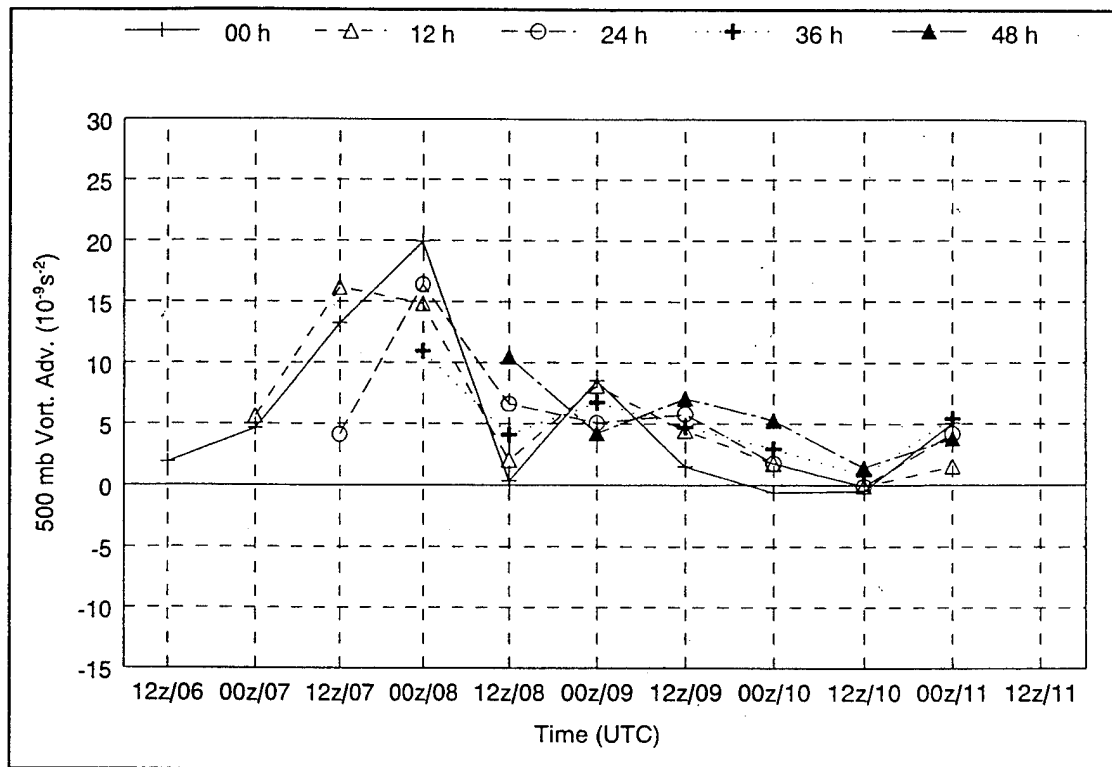


**Figure 12.** Cyclone 216 500 mb vorticity advection trace from 1200 UTC 6 May to 0000 UTC 11 May 1994.

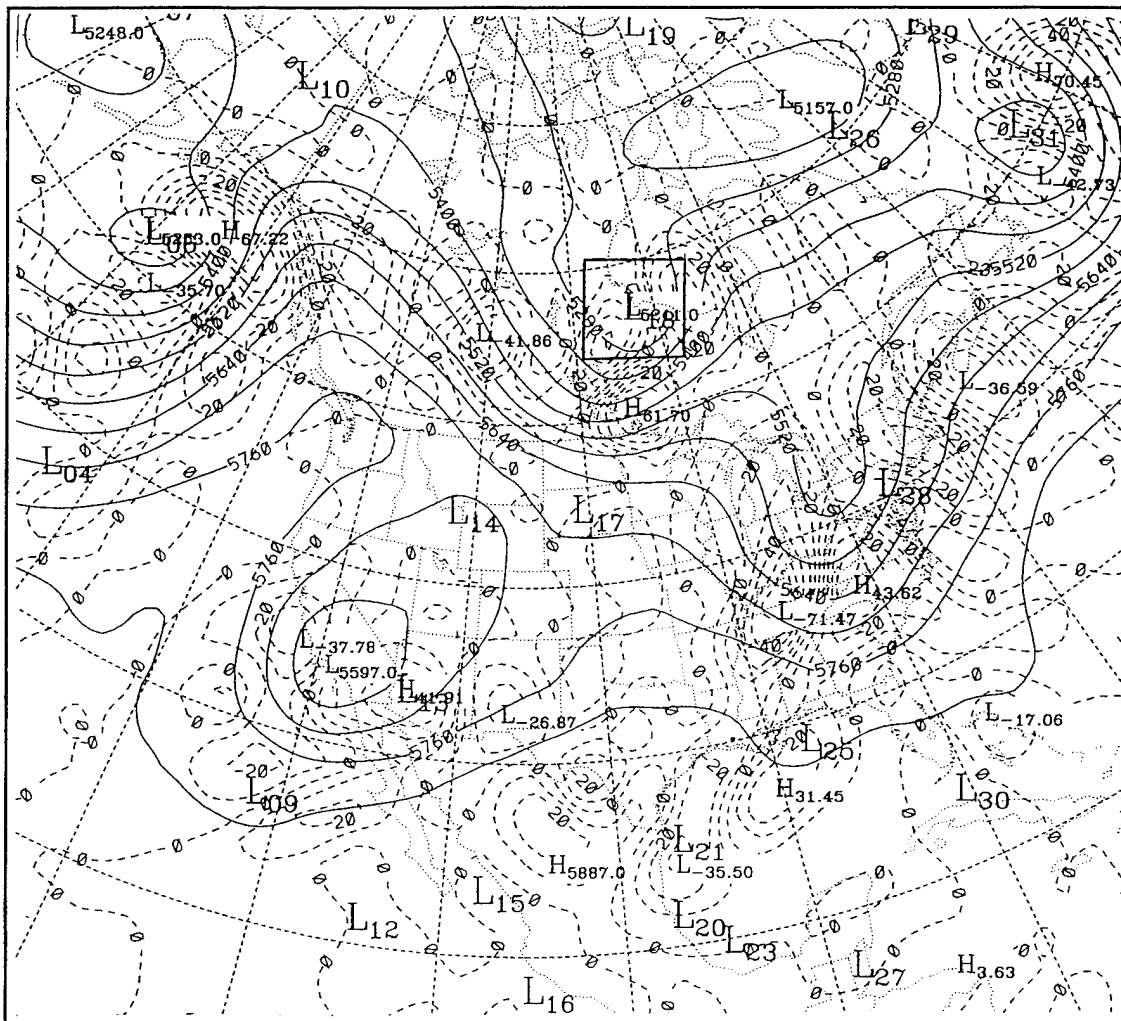


**Figure 13.** Eta model 500 mb height (solid, 120 m increment) and vorticity advection (dashed,  $10 \times 10^{-9} \text{ s}^{-2}$  increment) for 1200 UTC 8 May 1994. A 5 x 5 grid point averaging box is centered over the cyclone of interest.

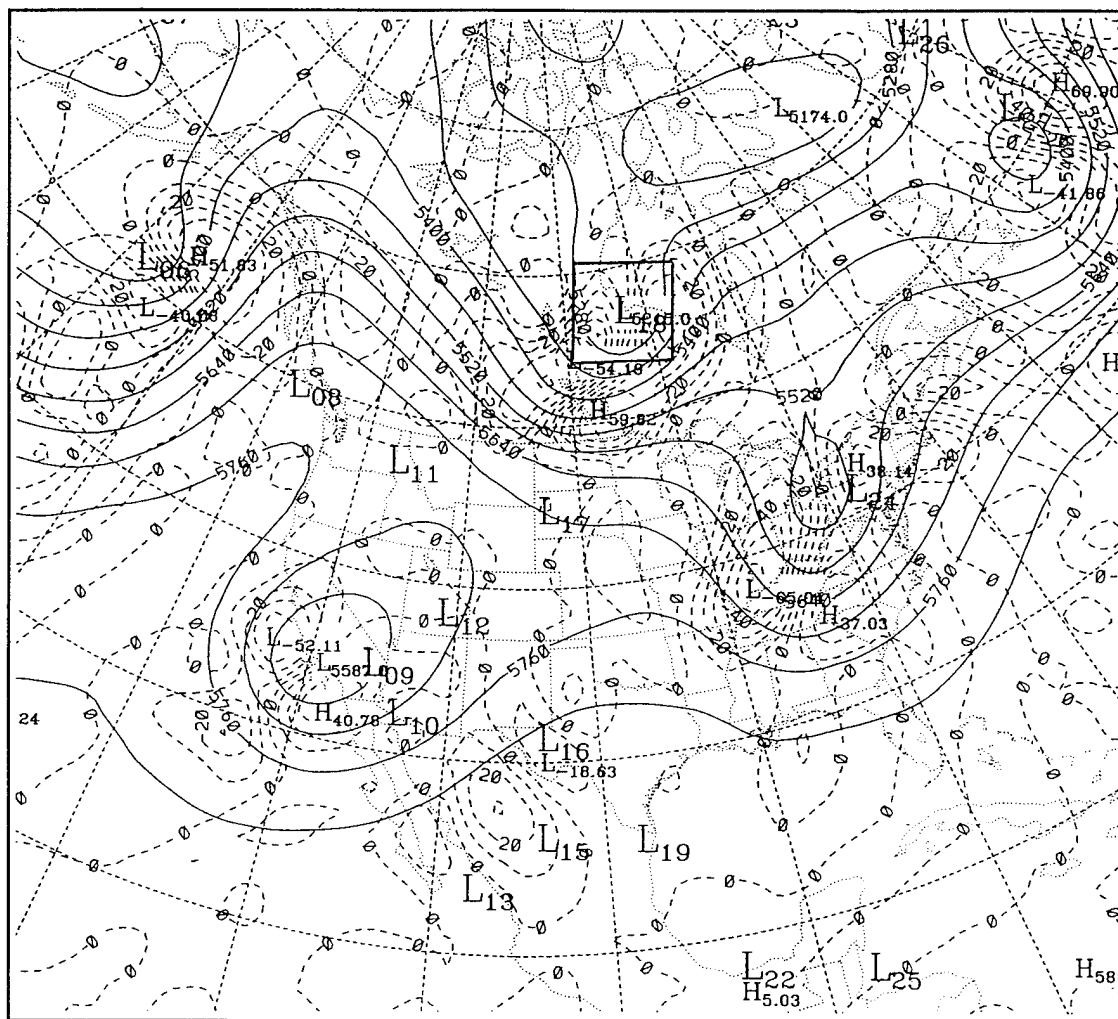


**Figure 14.** As in Figure 13, except for 12 h forecast valid at 1200 UTC 8 May 1994.

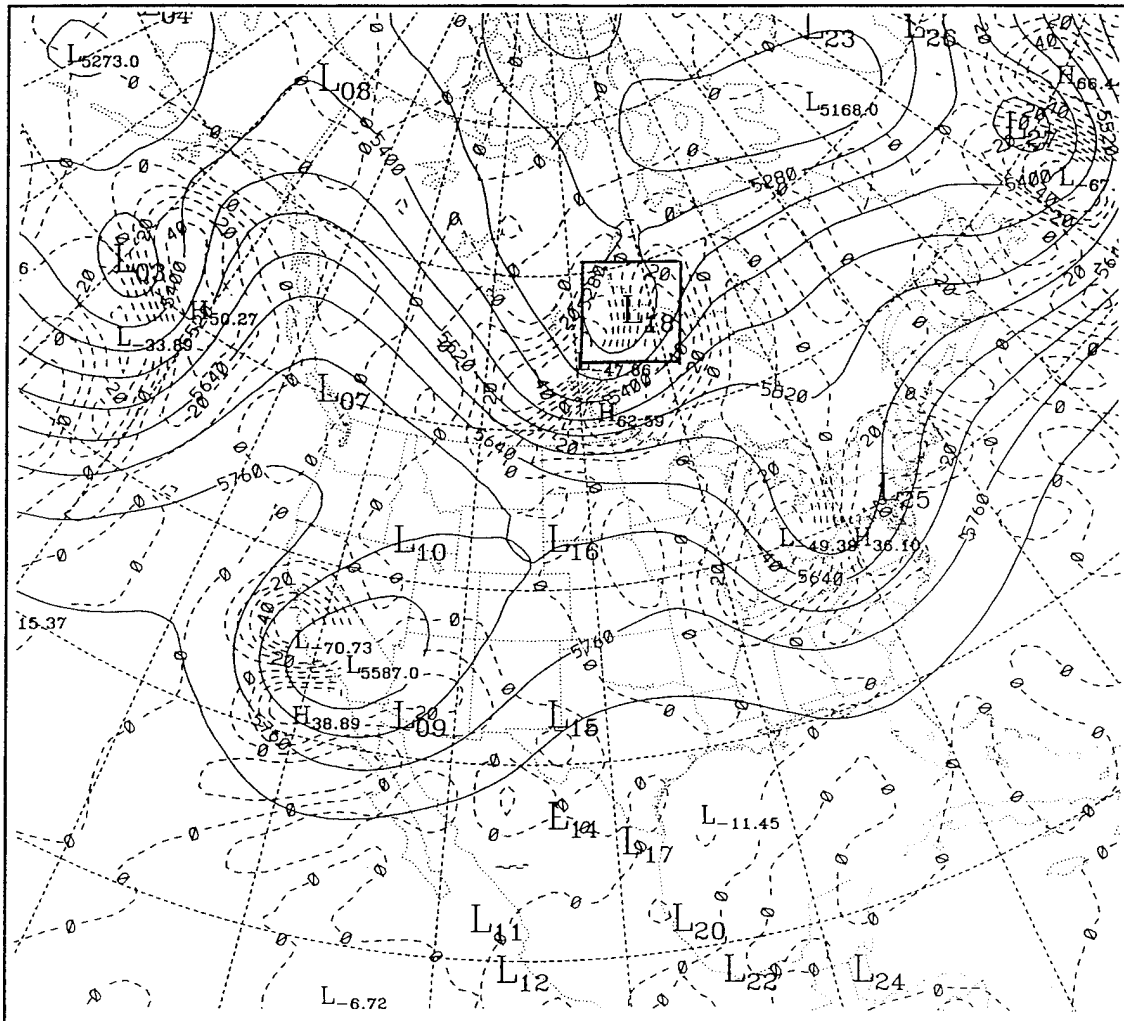


**Figure 15.** As in Figure 13, except for 24 h forecast valid at 1200 UTC 8 May 1994.

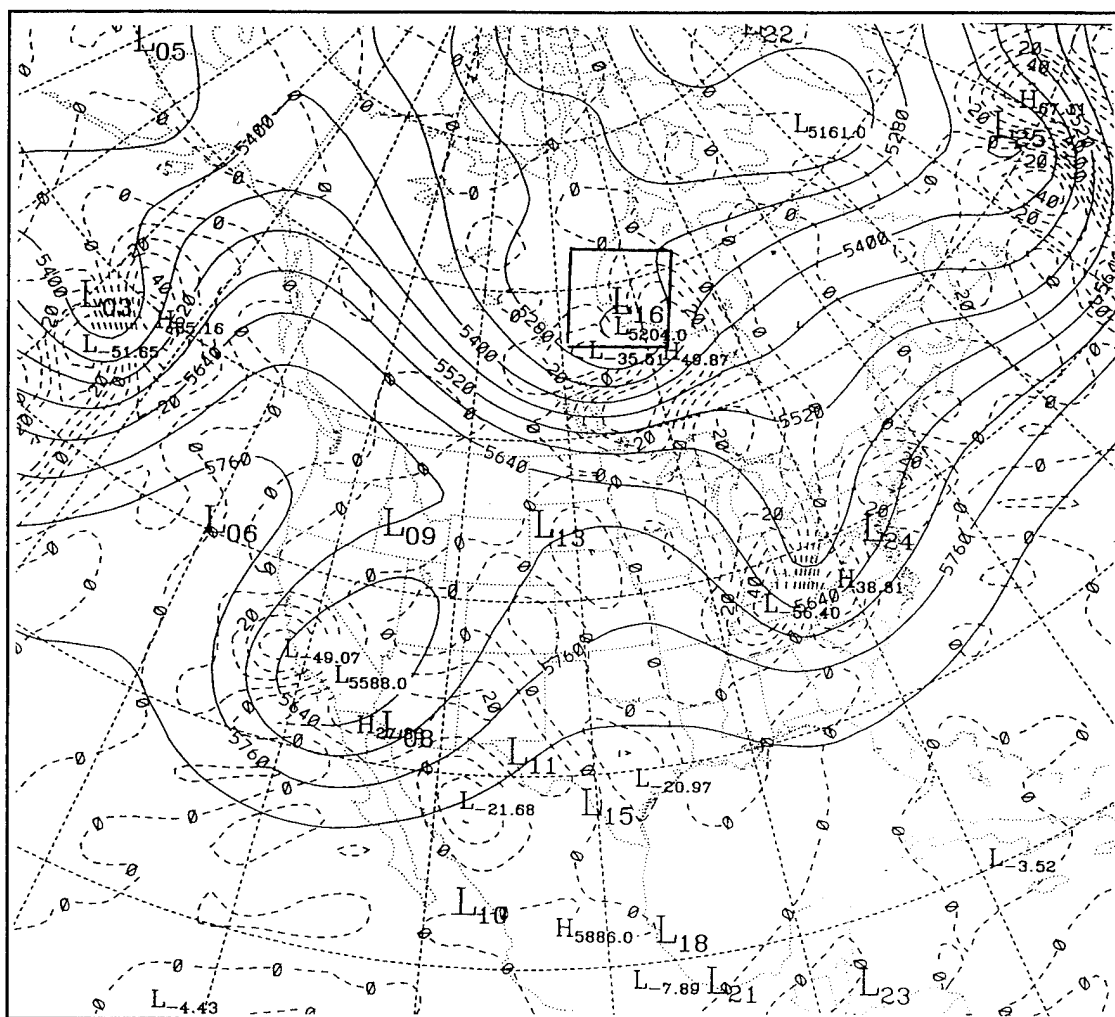


**Figure 16.** As in Figure 13, except for 36 h forecast valid at 1200 UTC 8 May 1994.

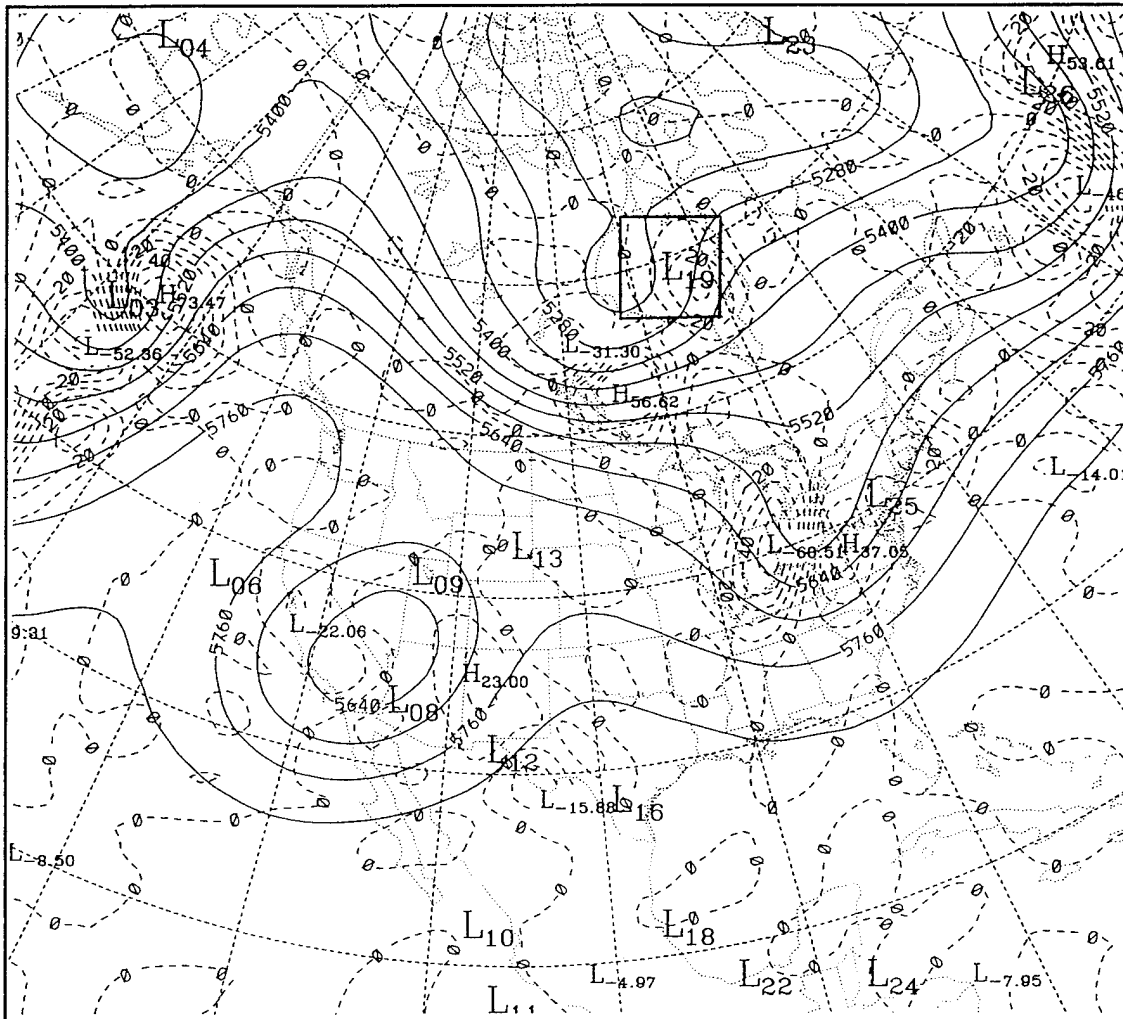


**Figure 17.** As in Figure 13, except for 48 h forecast valid at 1200 UTC 8 May 1994.

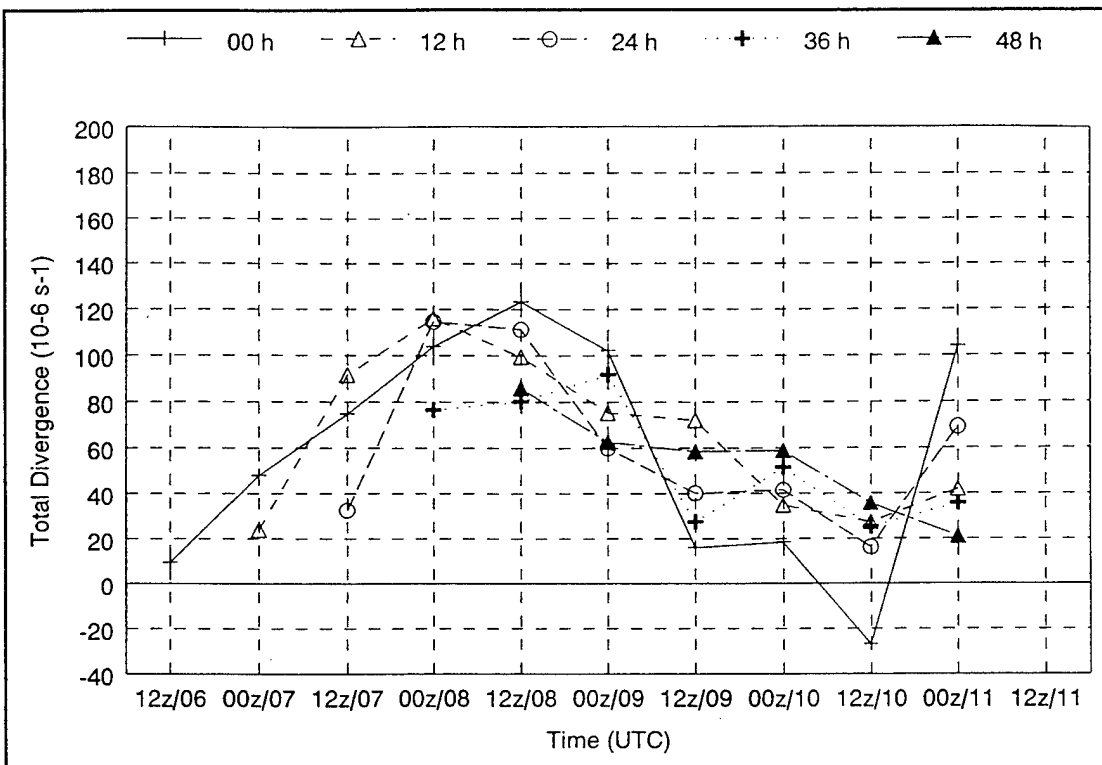


**Figure 18.** Cyclone 216 total divergence trace from 1200 UTC 6 May to 0000 UTC 11 May 1994.



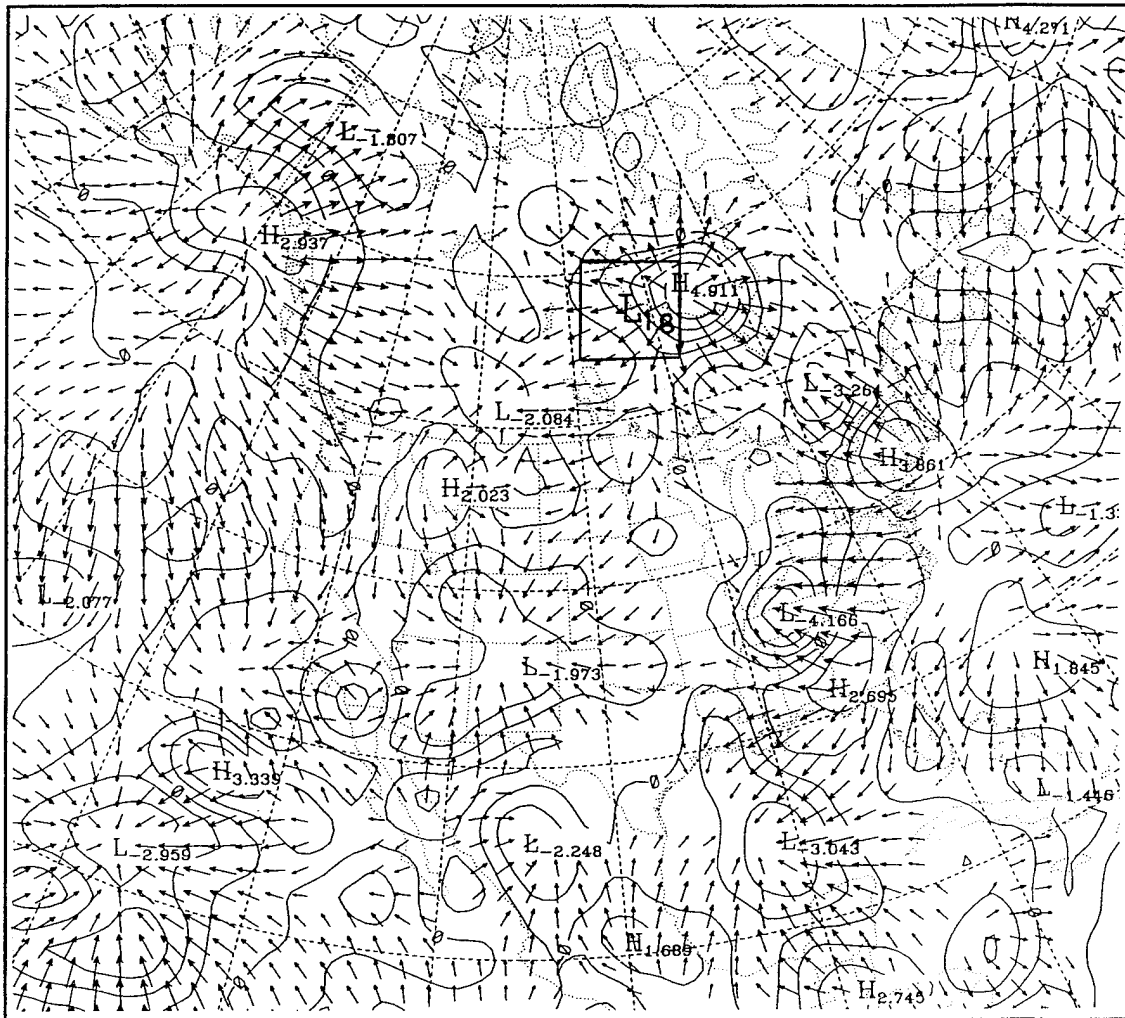


**Figure 19.** Eta model 300 mb total divergence (solid,  $10 \times 10^{-6} \text{ s}^{-1}$  increment) and vectors of divergent ageostrophic wind (1.0 to 8.5 m/s) for 1200 UTC 8 May 1994. The maximum (H) and minimum (L) divergence are labeled as  $10^{-6} \text{ s}^{-1}$ . A 5 x 5 grid point averaging box is centered over the cyclone of interest.

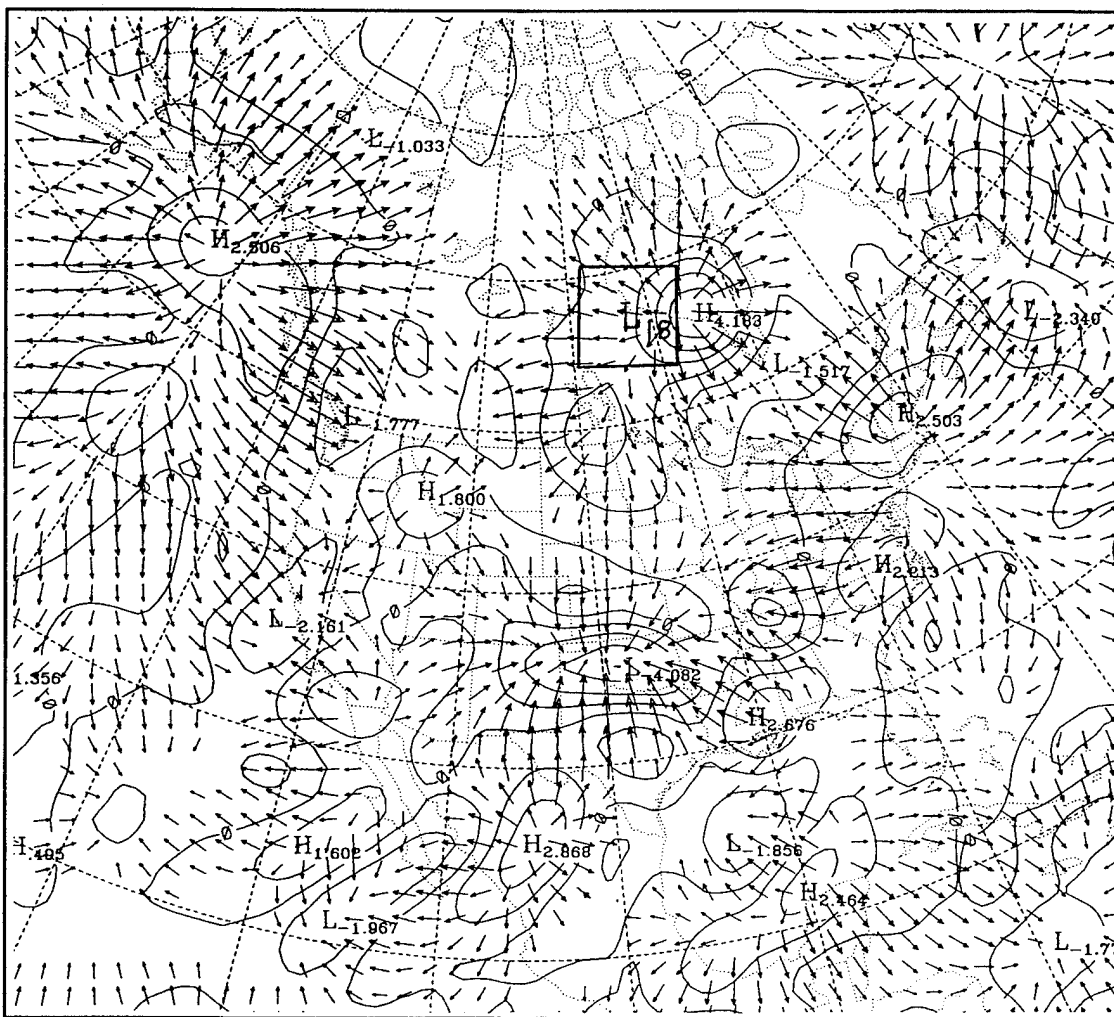


**Figure 20.** As in Figure 19, except for 12 h forecast valid at 1200 UTC 8 May 1994.

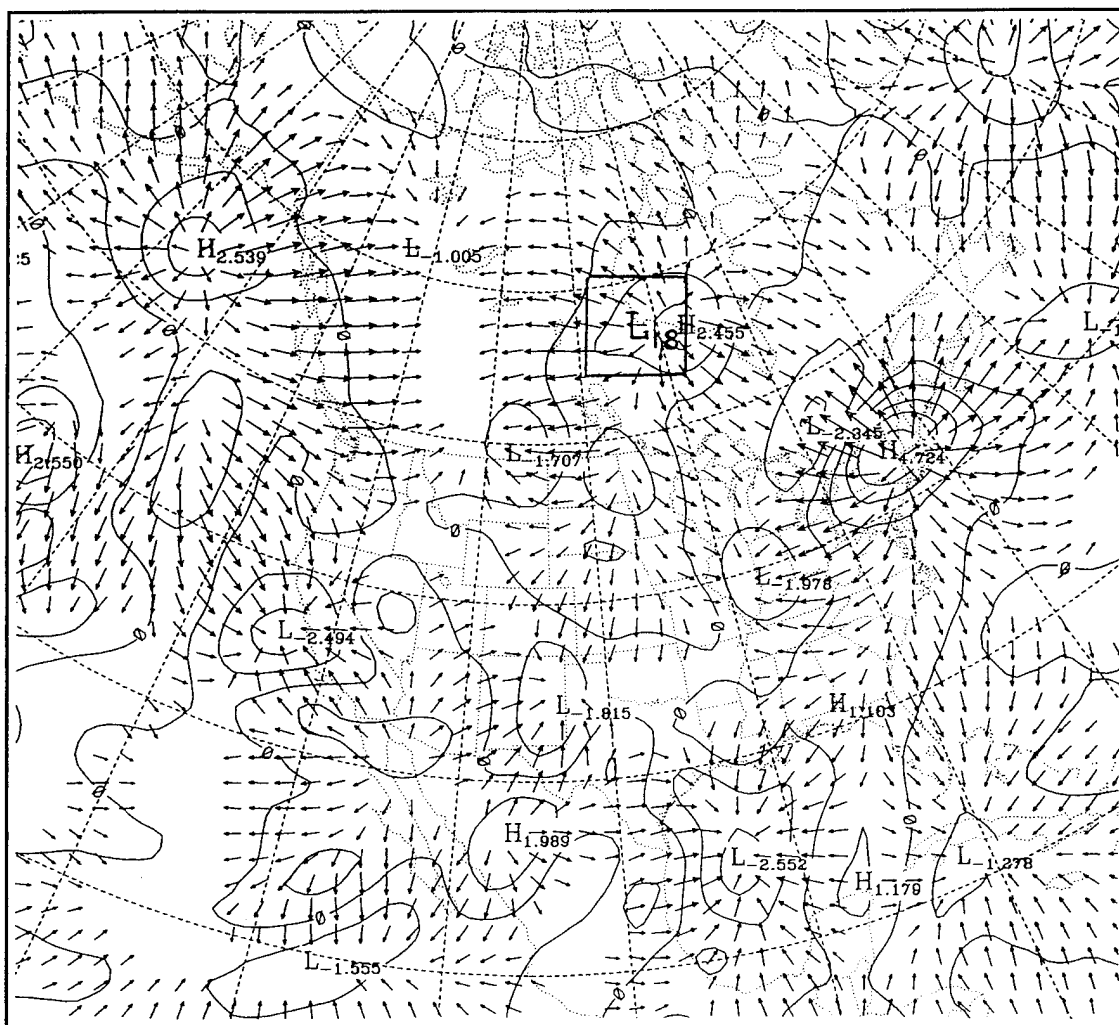


**Figure 21.** As in Figure 19, except for 24 h forecast valid at 1200 UTC 8 May 1994.

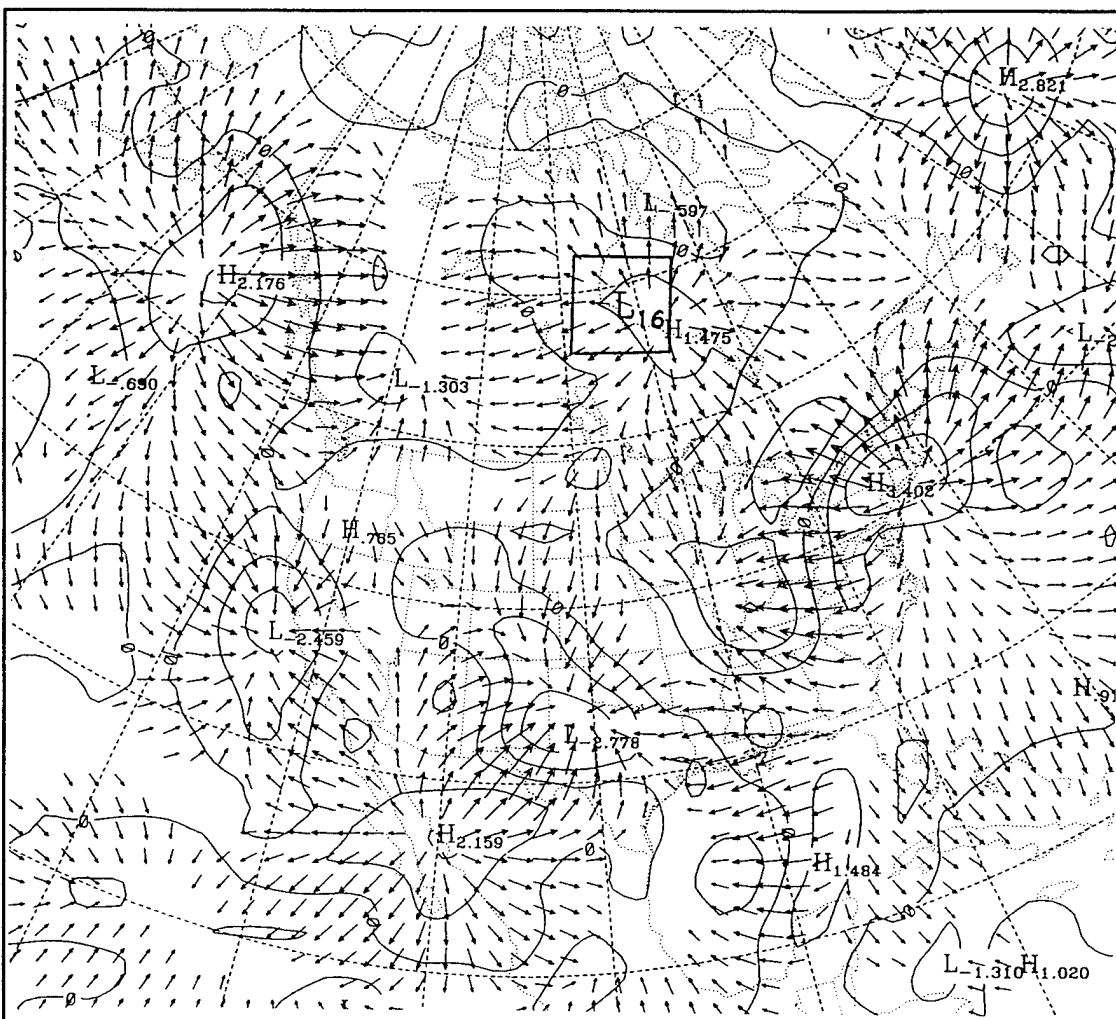


**Figure 22.** As in Figure 19, except for 36 h forecast valid at 1200 UTC 8 May 1994.

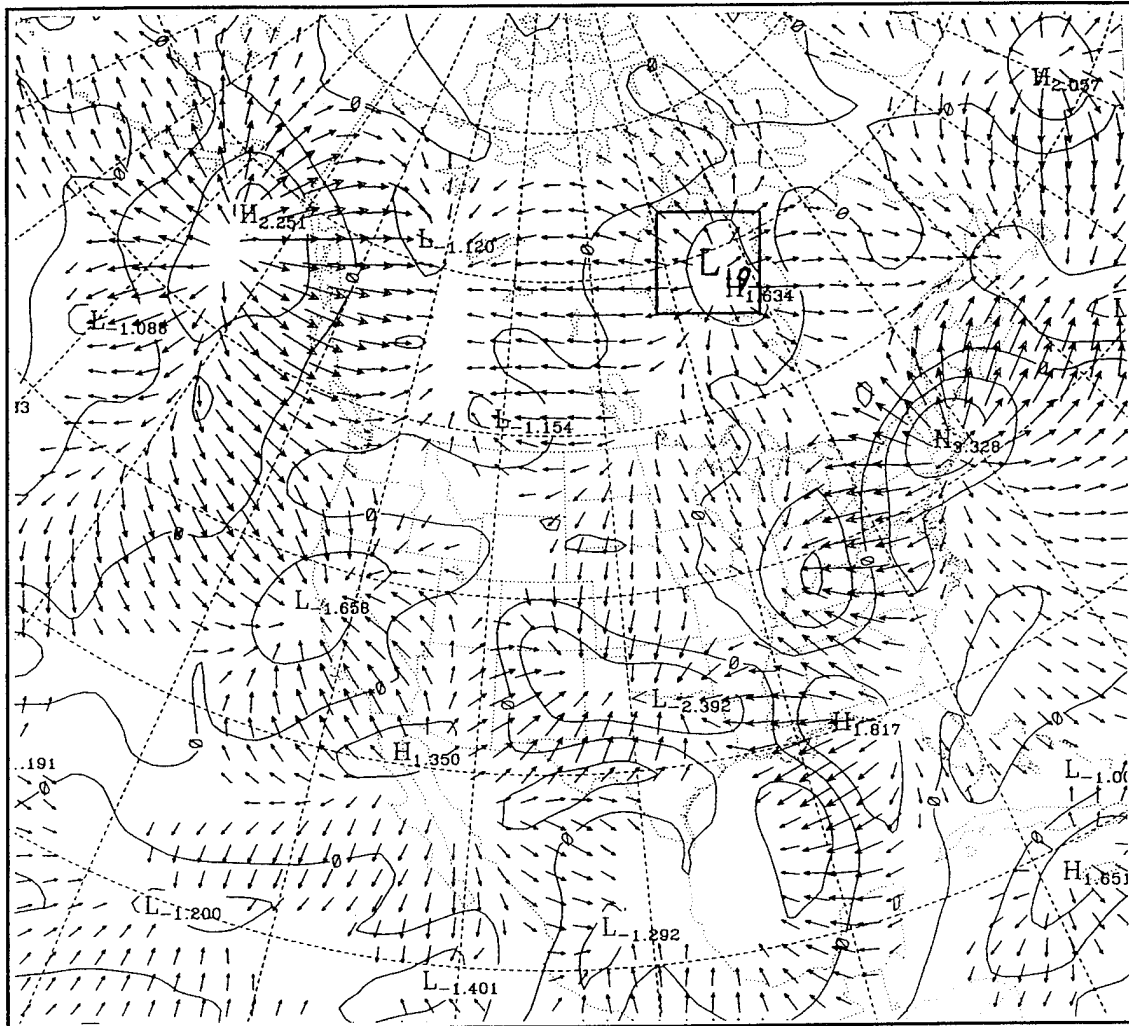


**Figure 23.** As in Figure 19, except for 48 h forecast valid at 1200 UTC 8 May 1994.

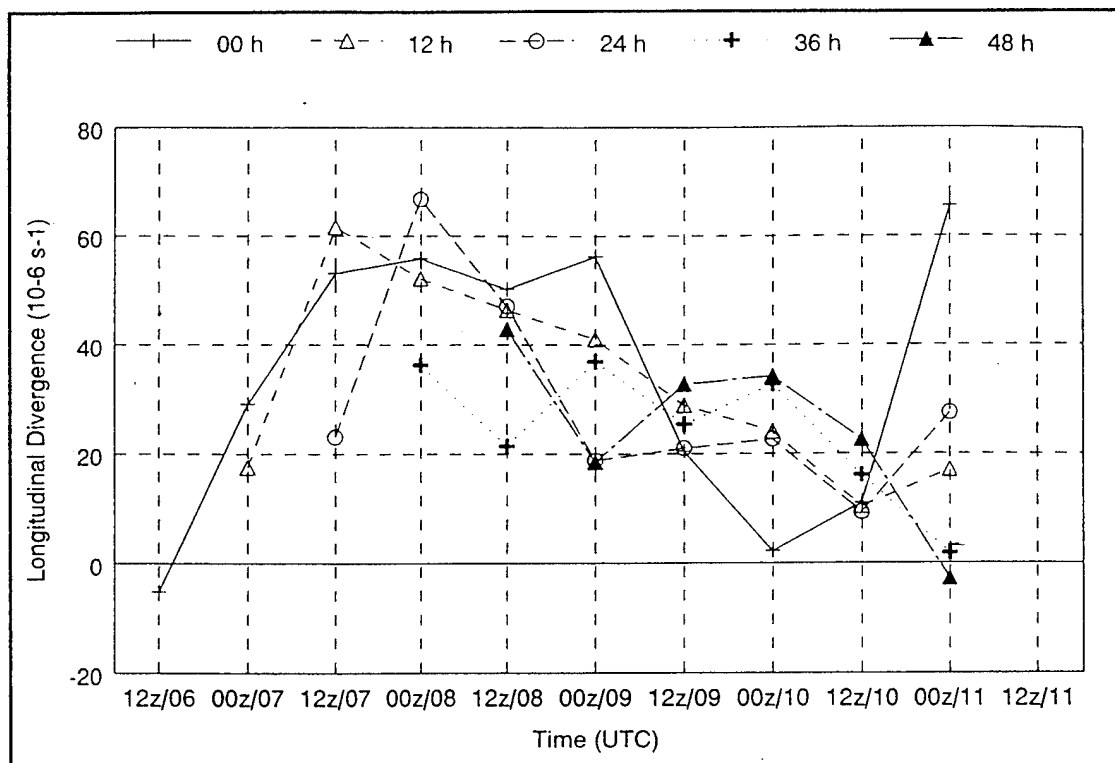


**Figure 24.** Cyclone 216 longitudinal divergence trace from 1200 UTC 6 May to 0000 UTC 11 May 1994.

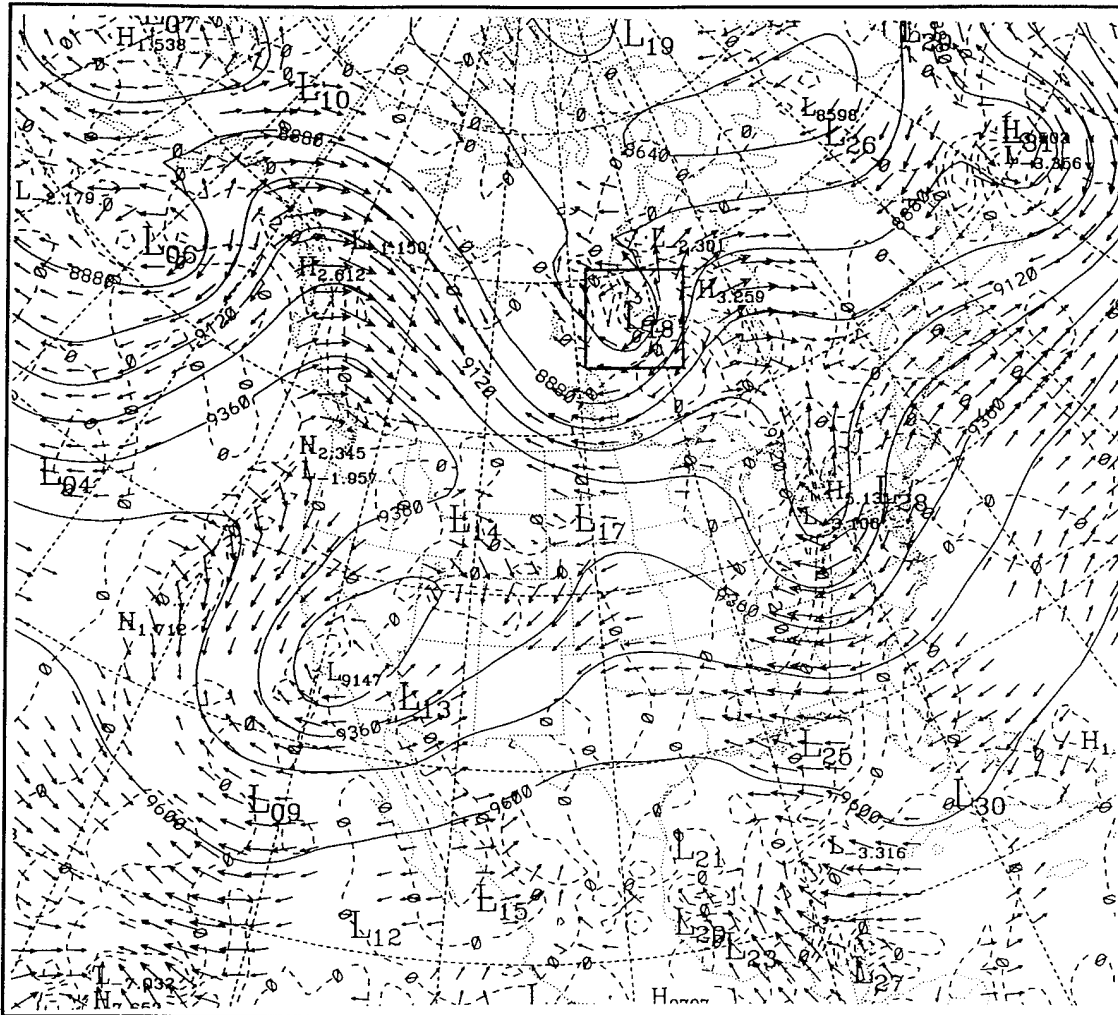


**Figure 25.** Eta model 300 mb height (solid, 12 m increment), longitudinal divergence (dashed,  $1 \times 10^{-6} \text{ s}^{-1}$  increment) and vectors of the longitudinal component of the divergent ageostrophic wind (1.0 to 6.0 m/s) for 1200 UTC 8 May 1994. A 5 x 5 grid point averaging box is centered over the cyclone of interest.





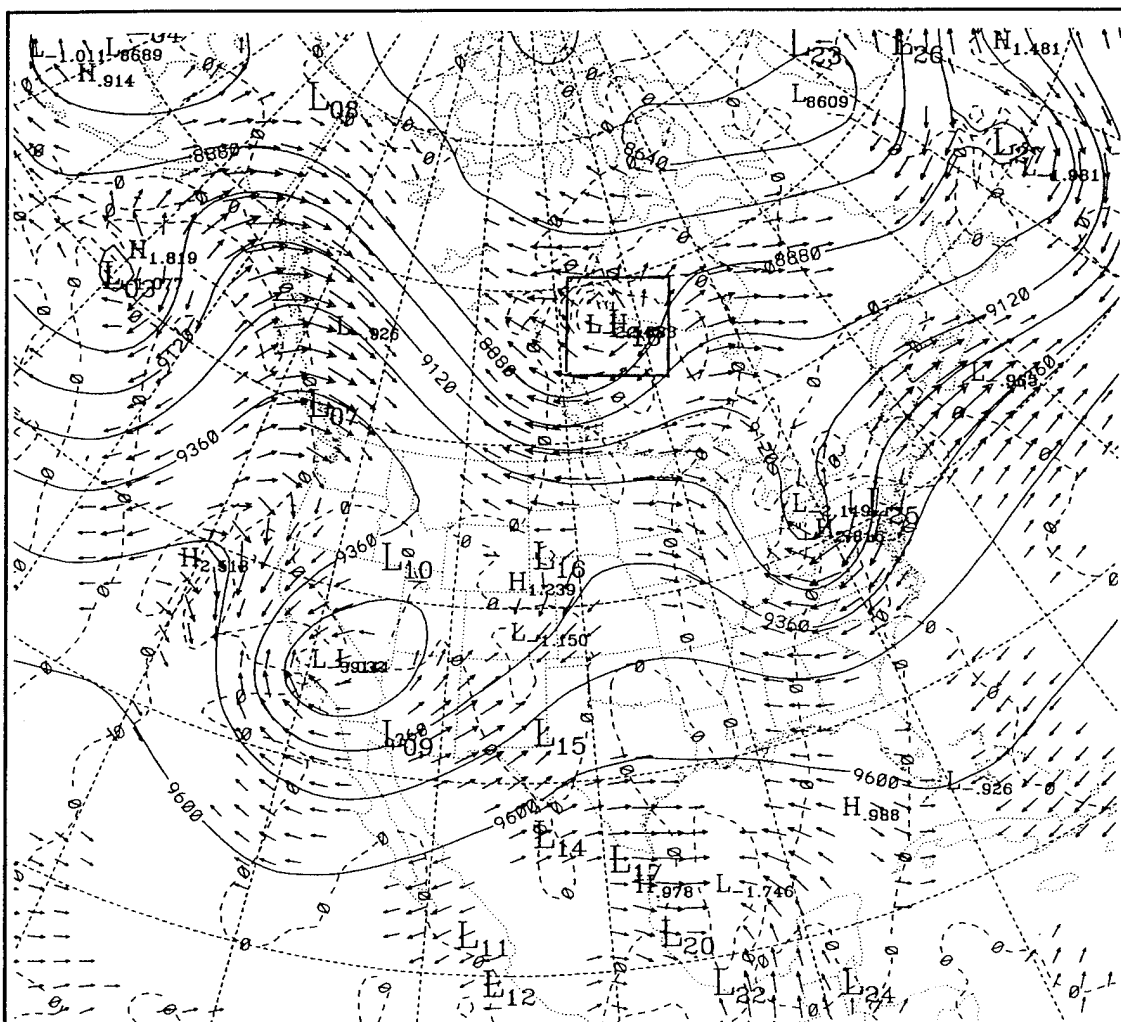


**Figure 27.** As in Figure 25, except for 24 h forecast valid at 1200 UTC 8 May 1994.

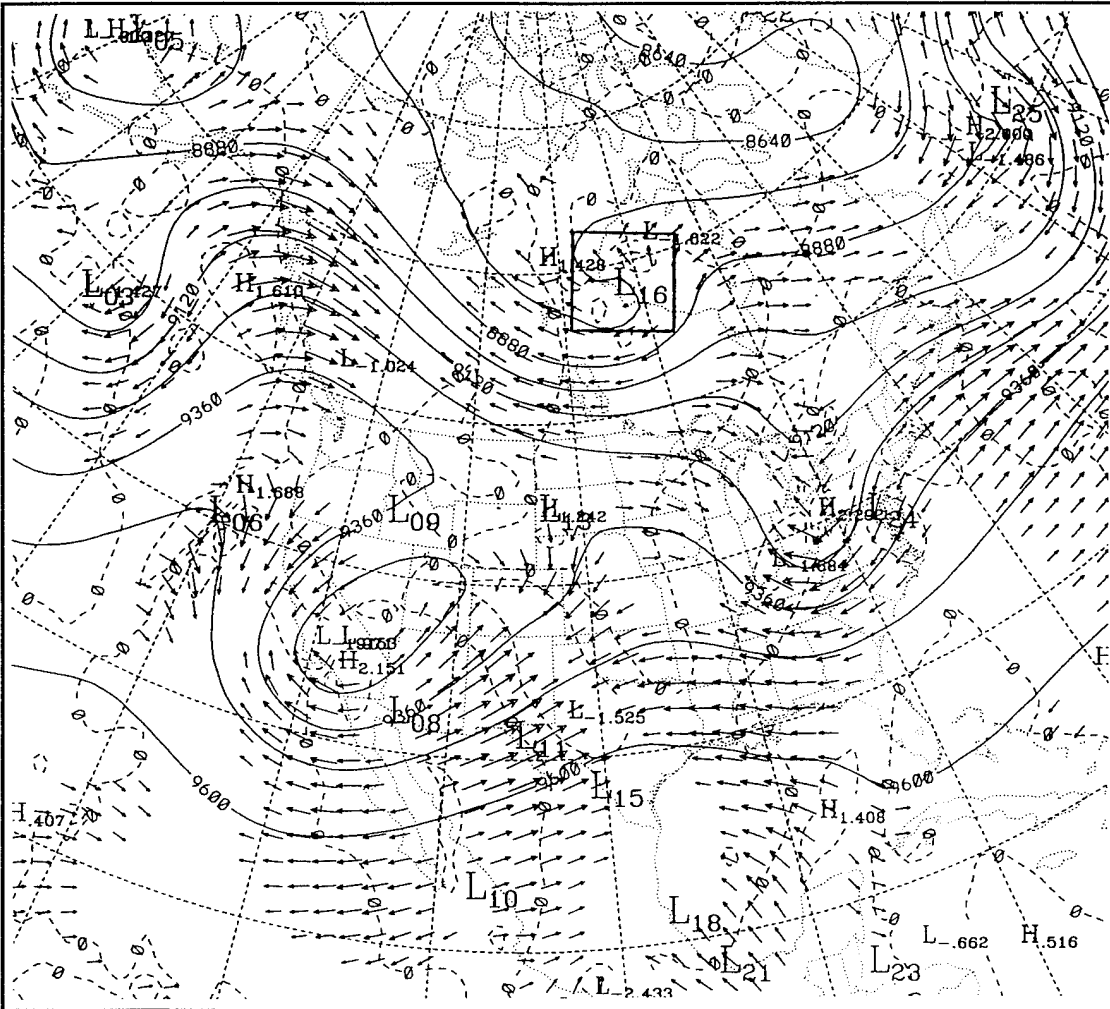


**Figure 28.** As in Figure 25, except for 36 h forecast valid at 1200 UTC 8 May 1994.

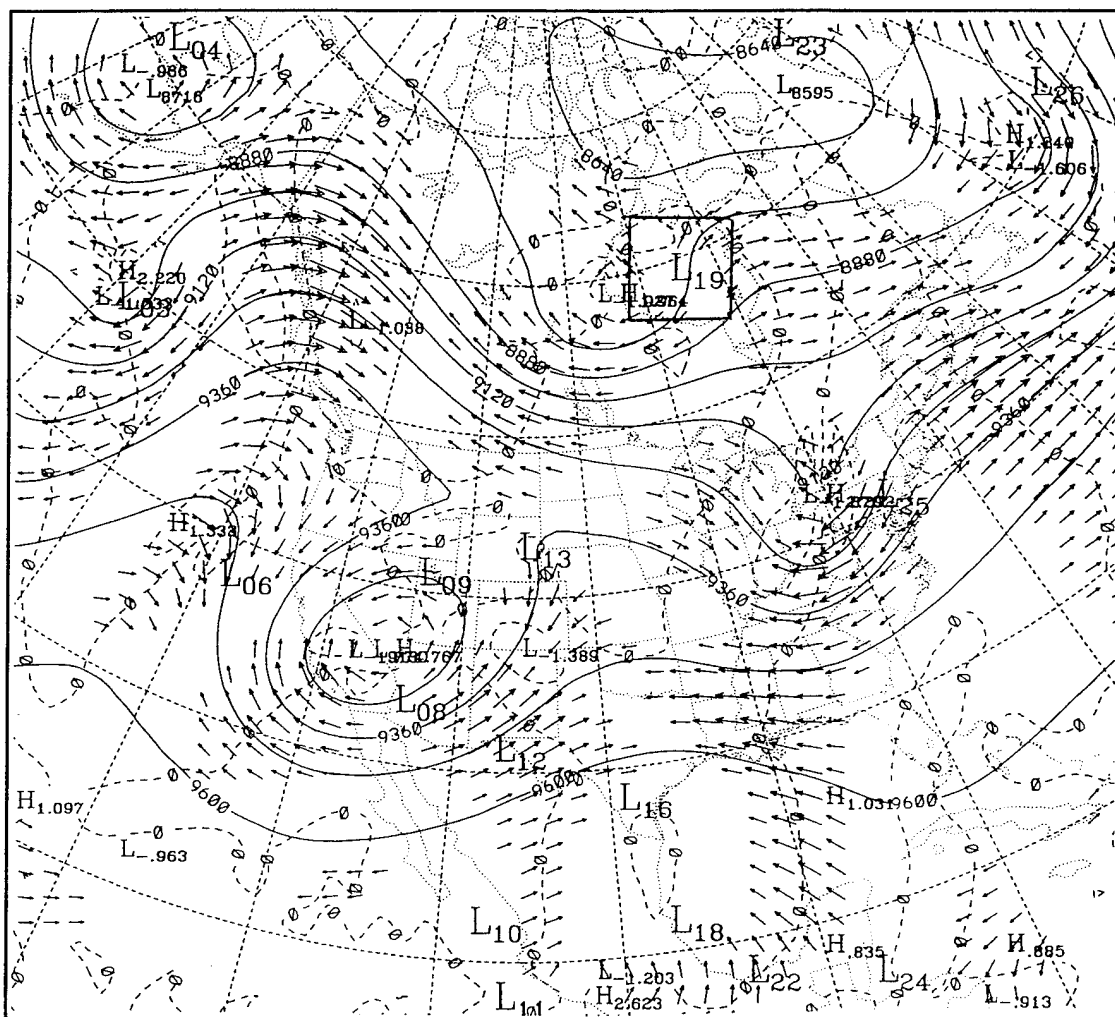
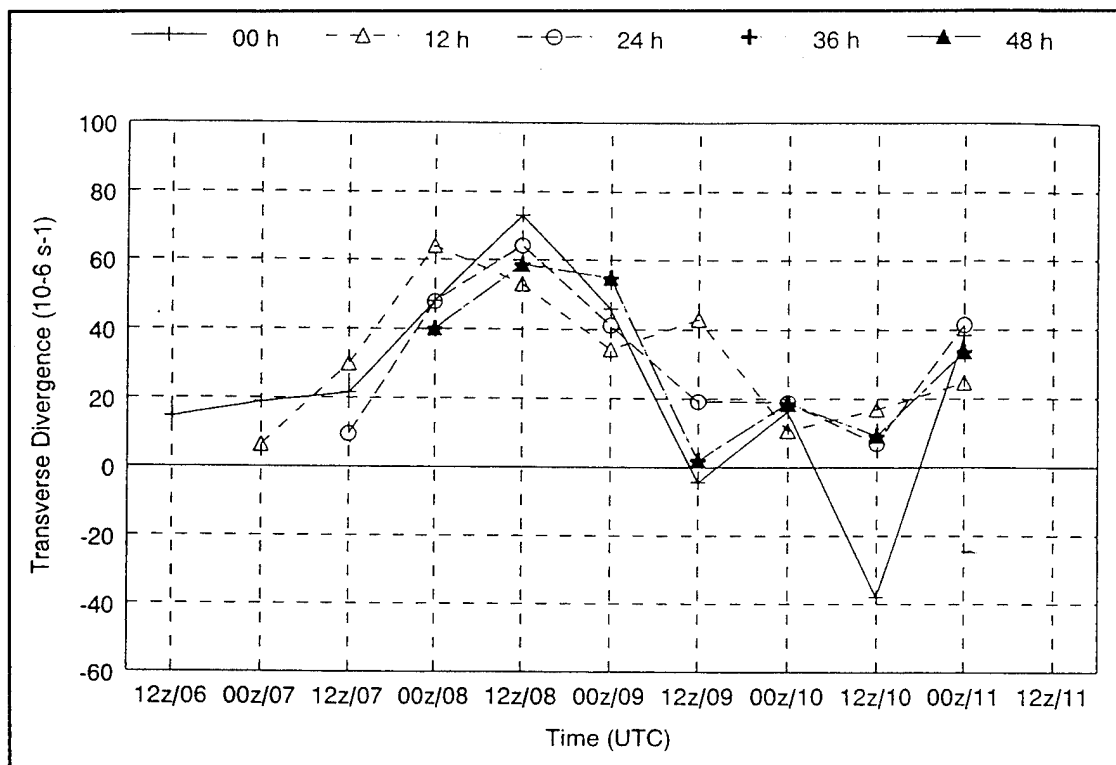
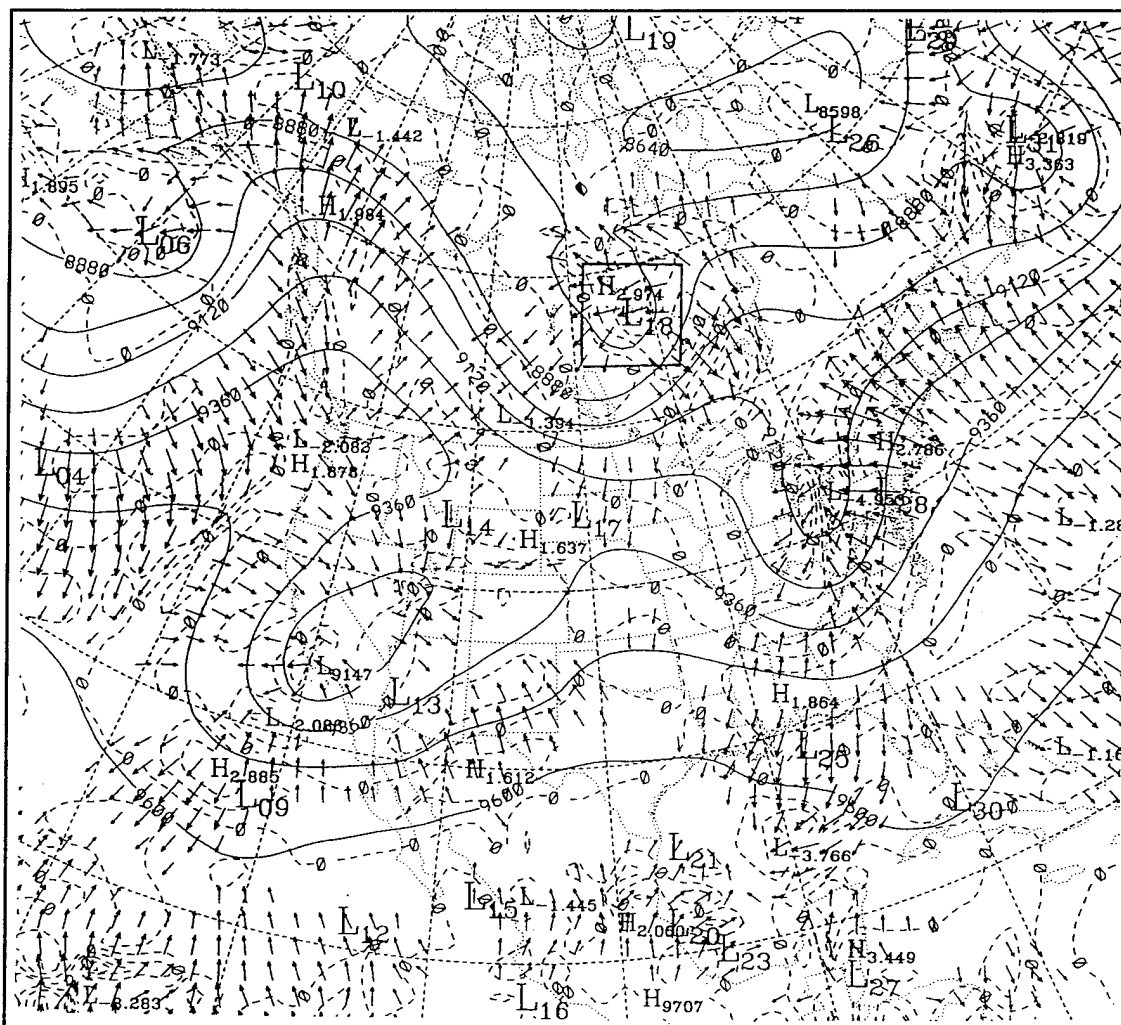
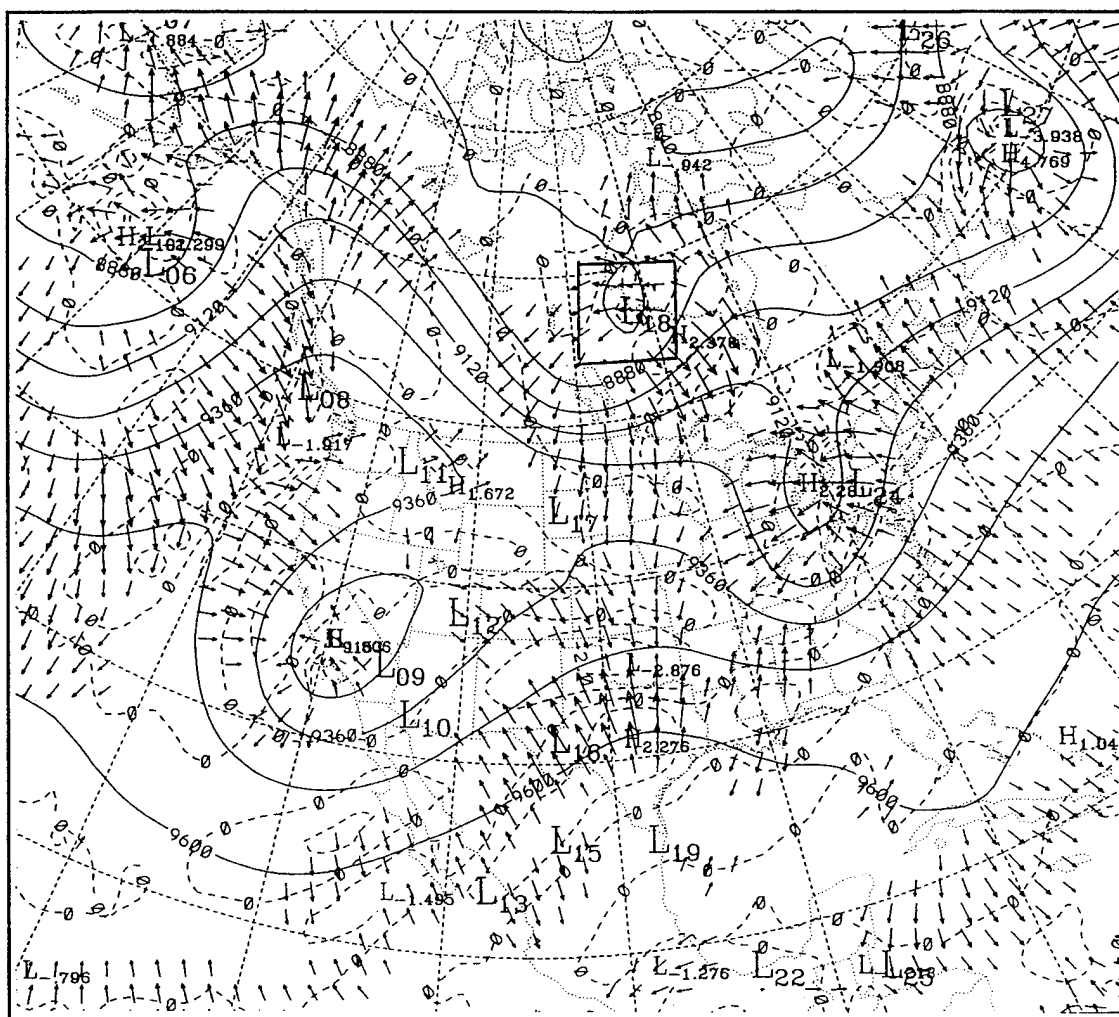


Figure 29. As in Figure 25, except for 48 h forecast valid at 1200 UTC 8 May 1994.



**Figure 30.** Cyclone 216 transverse divergence trace from 1200 UTC 6 May to 0000 UTC 11 May 1994.





**Figure 32.** As in Figure 31, except for 12 h forecast valid at 1200 UTC 8 May 1994.

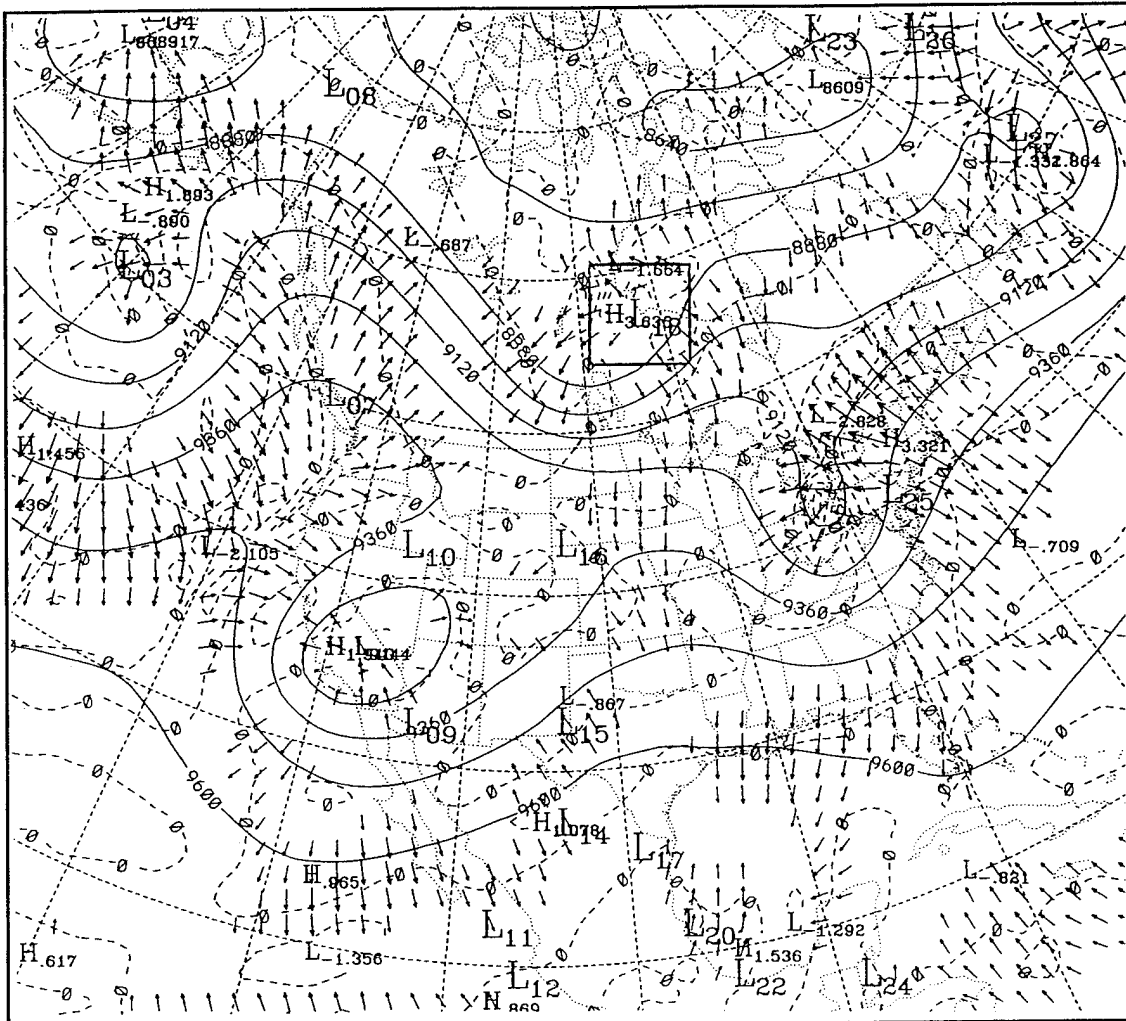


**Figure 33.** As in Figure 31, except for 24 h forecast valid at 1200 UTC 8 May 1994.

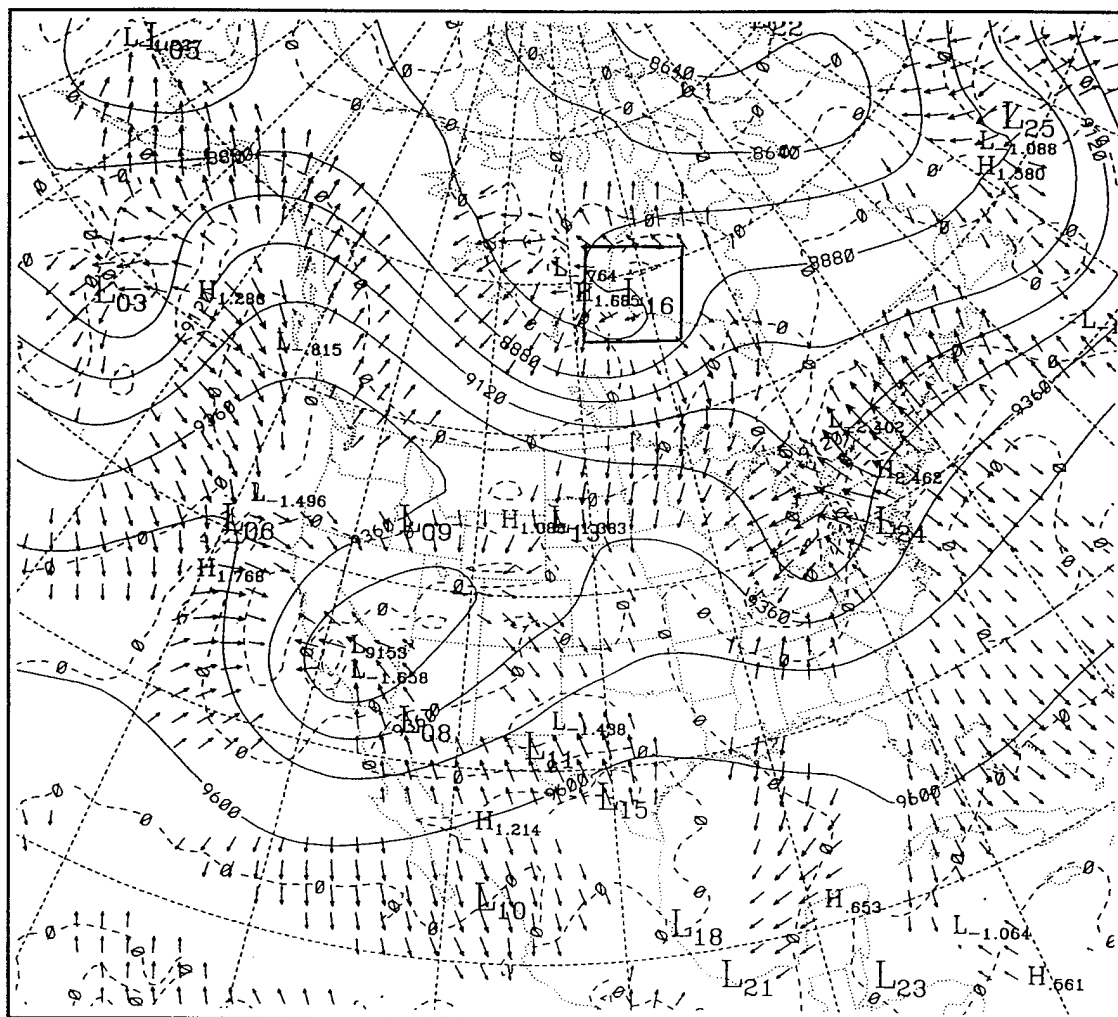


**Figure 34.** As in Figure 31, except for 36 h forecast valid at 1200 UTC 8 May 1994.



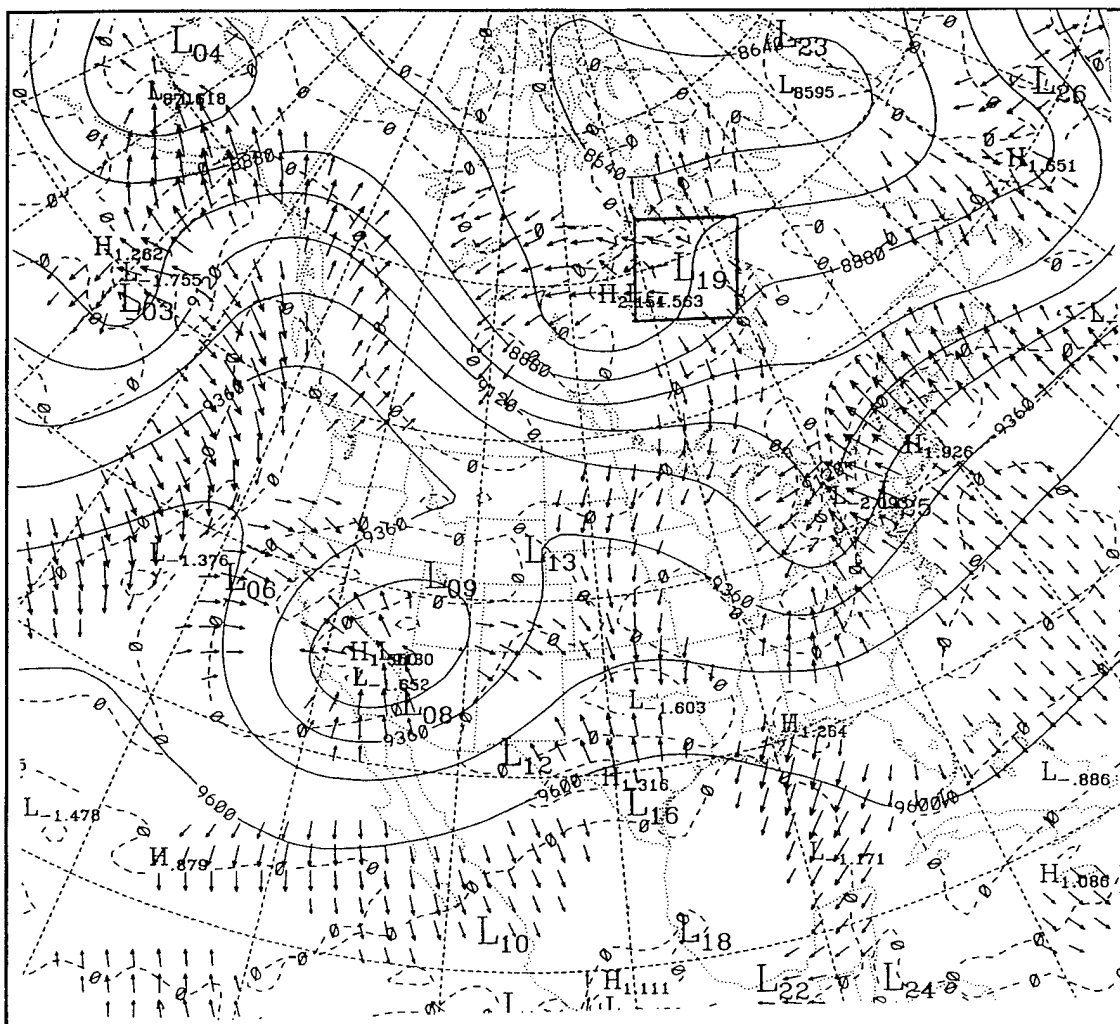


**Figure 35.** As in Figure 31, except for 48 h forecast valid at 1200 UTC 8 May 1994.

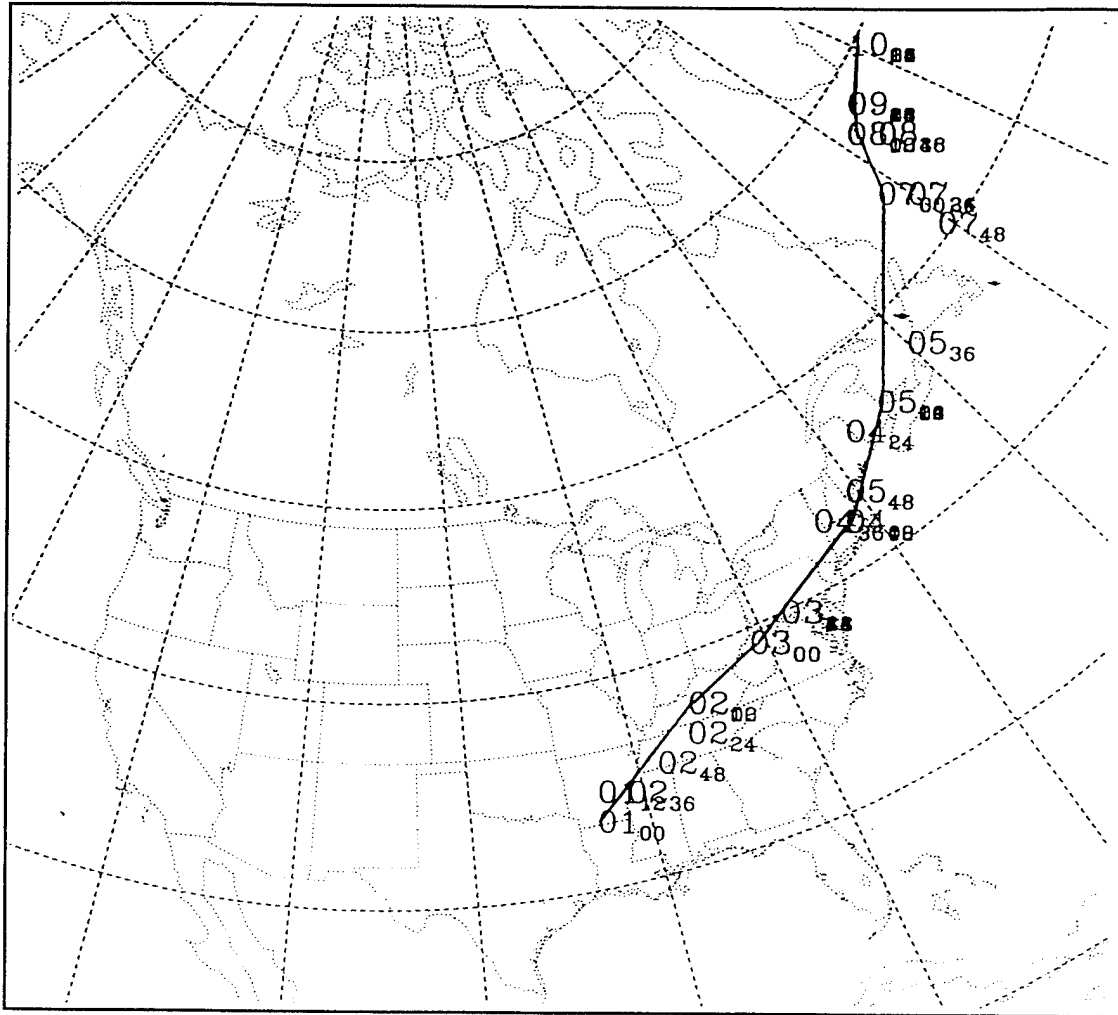


**Figure 36.** The 12-hourly surface cyclone center positions from the Eta model analysis (subscript 00) and forecasts at 12 h (subscript 12), 24 h (subscript 24), 36 h (subscript 36), and 48 h (subscript 48) between 0000 UTC 6 April (large 01) and 1200 UTC 10 April 1994 (large 10).

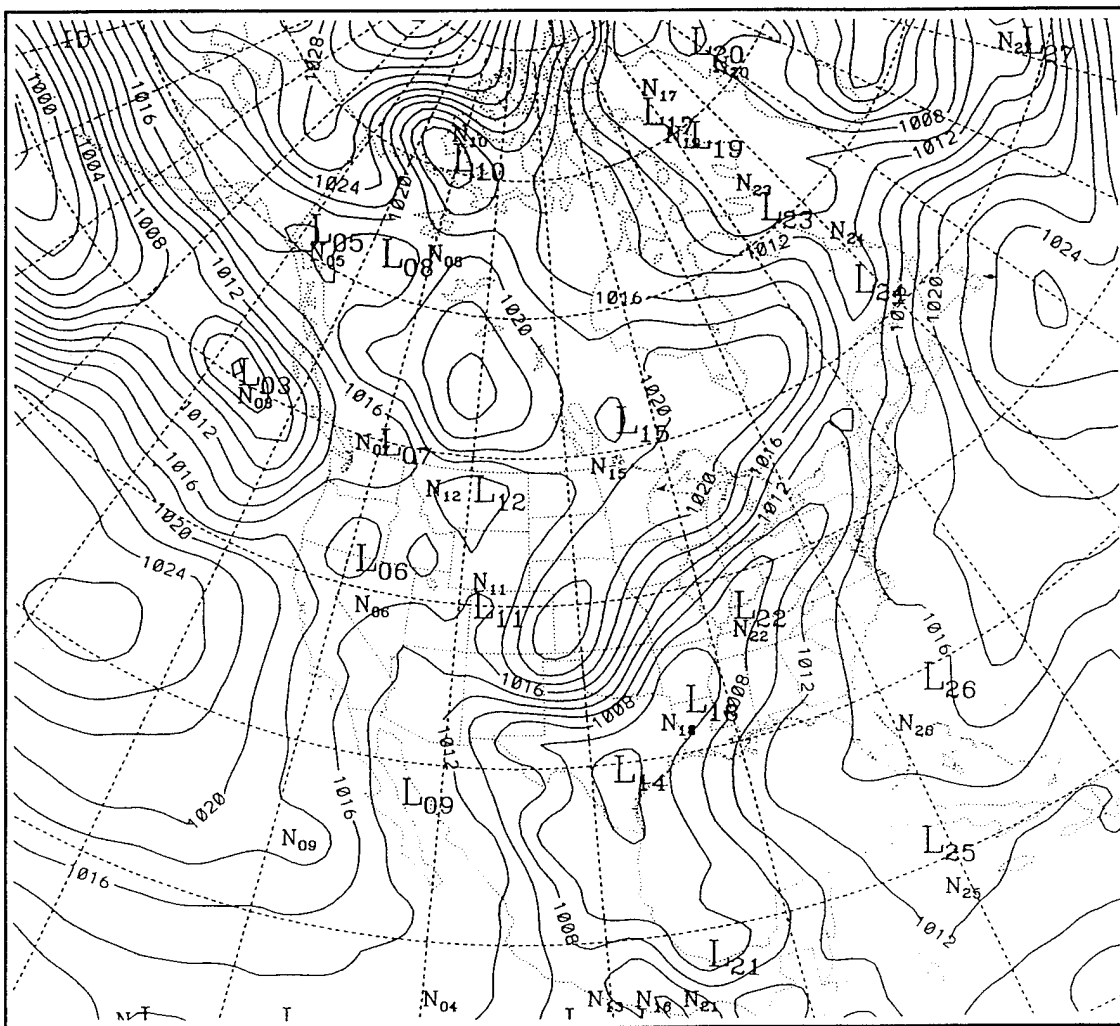


**Figure 37.** Eta model surface pressure (solid, 2 mb increment) analysis for 0000 UTC 6 April 1994. A 5 x 5 grid point averaging box is centered over the cyclone of interest labeled L<sub>18</sub>.

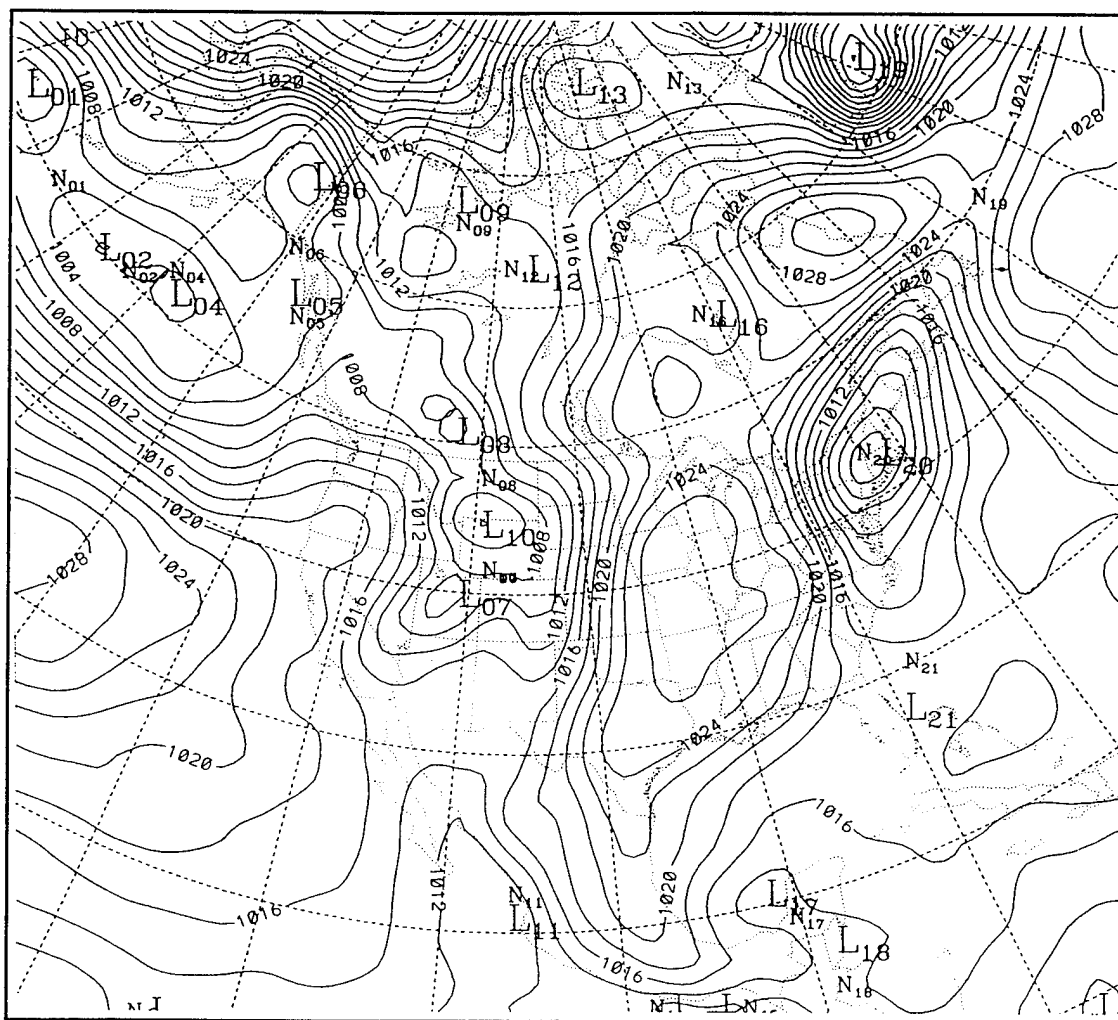


**Figure 38.** As in Figure 37, except for 1200 UTC 7 April 1994 and the cyclone of interest is labeled L<sub>20</sub>.

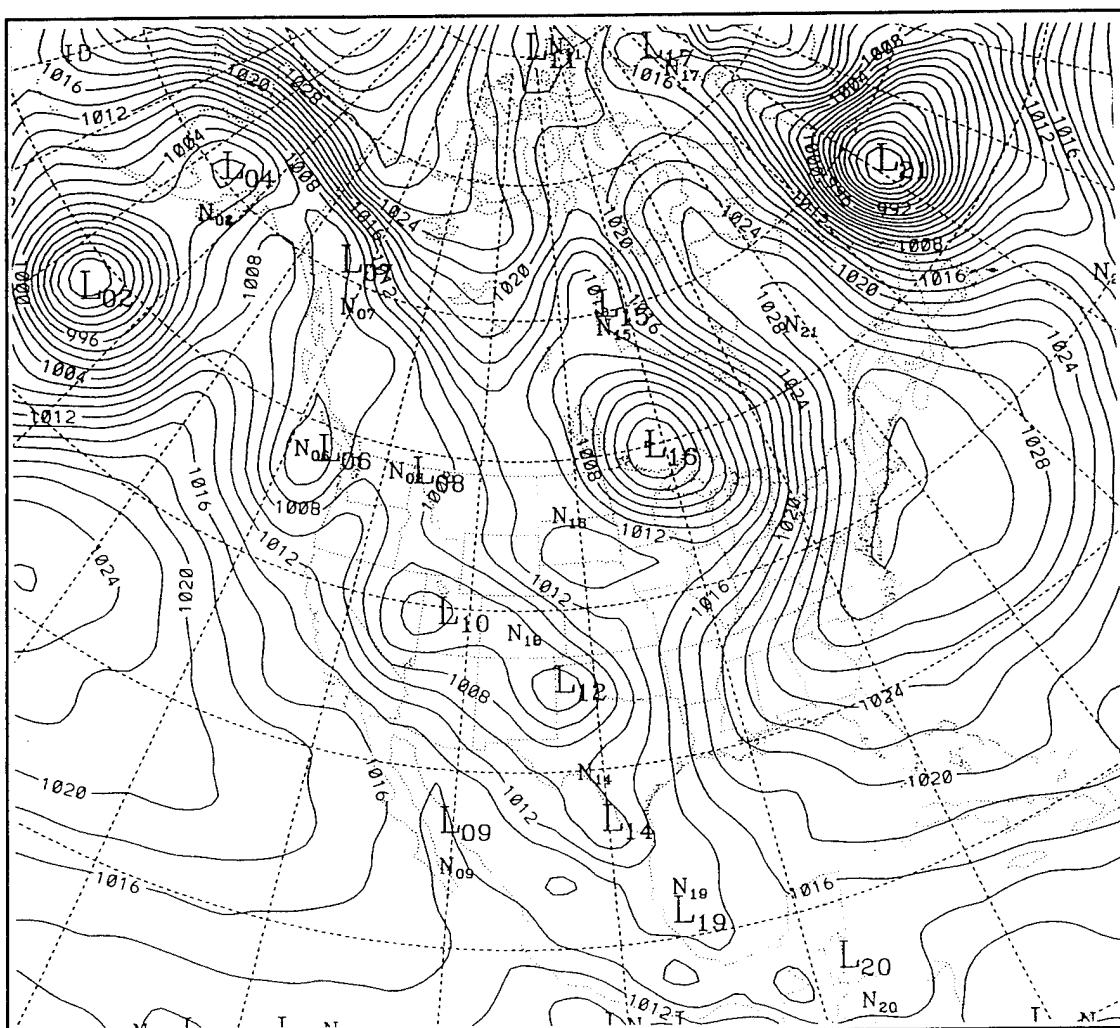


**Figure 39.** As in Figure 37, except for 1200 UTC 9 April 1994 and the cyclone of interest is labeled L<sub>21</sub>.

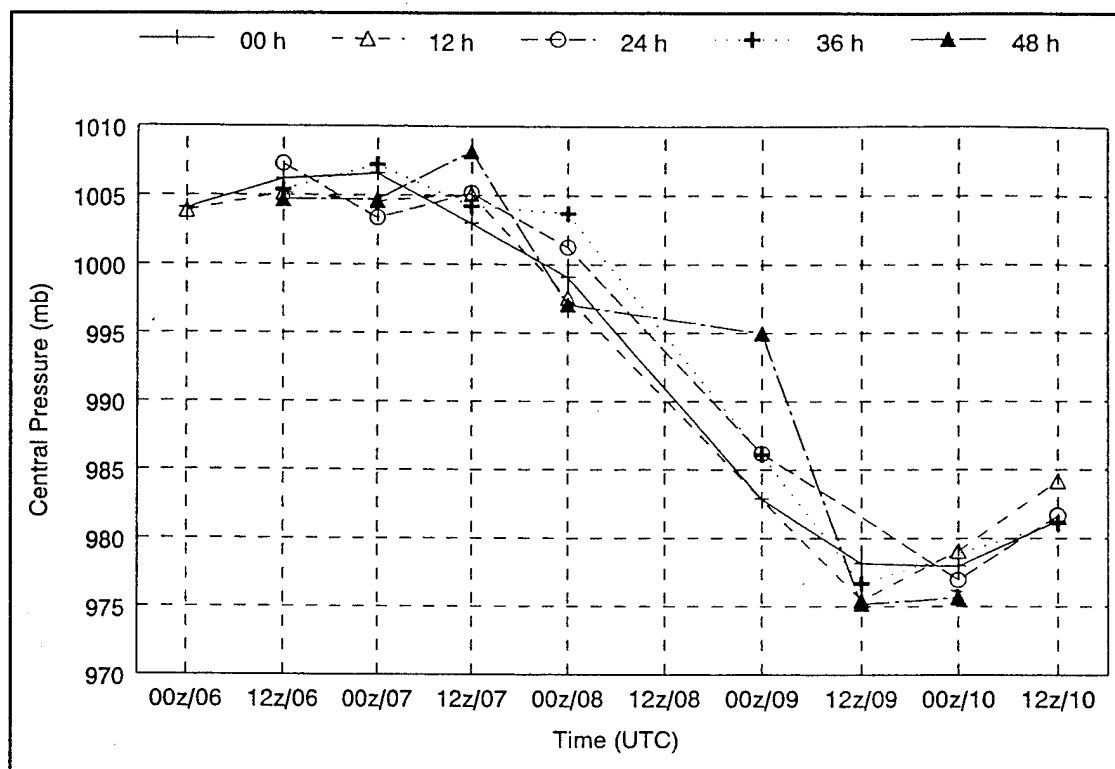


**Figure 40.** Cyclone 165 central pressure trace from 0000 UTC 6 April (00Z/06) to 1200 UTC 10 April 1994 (12Z/10).

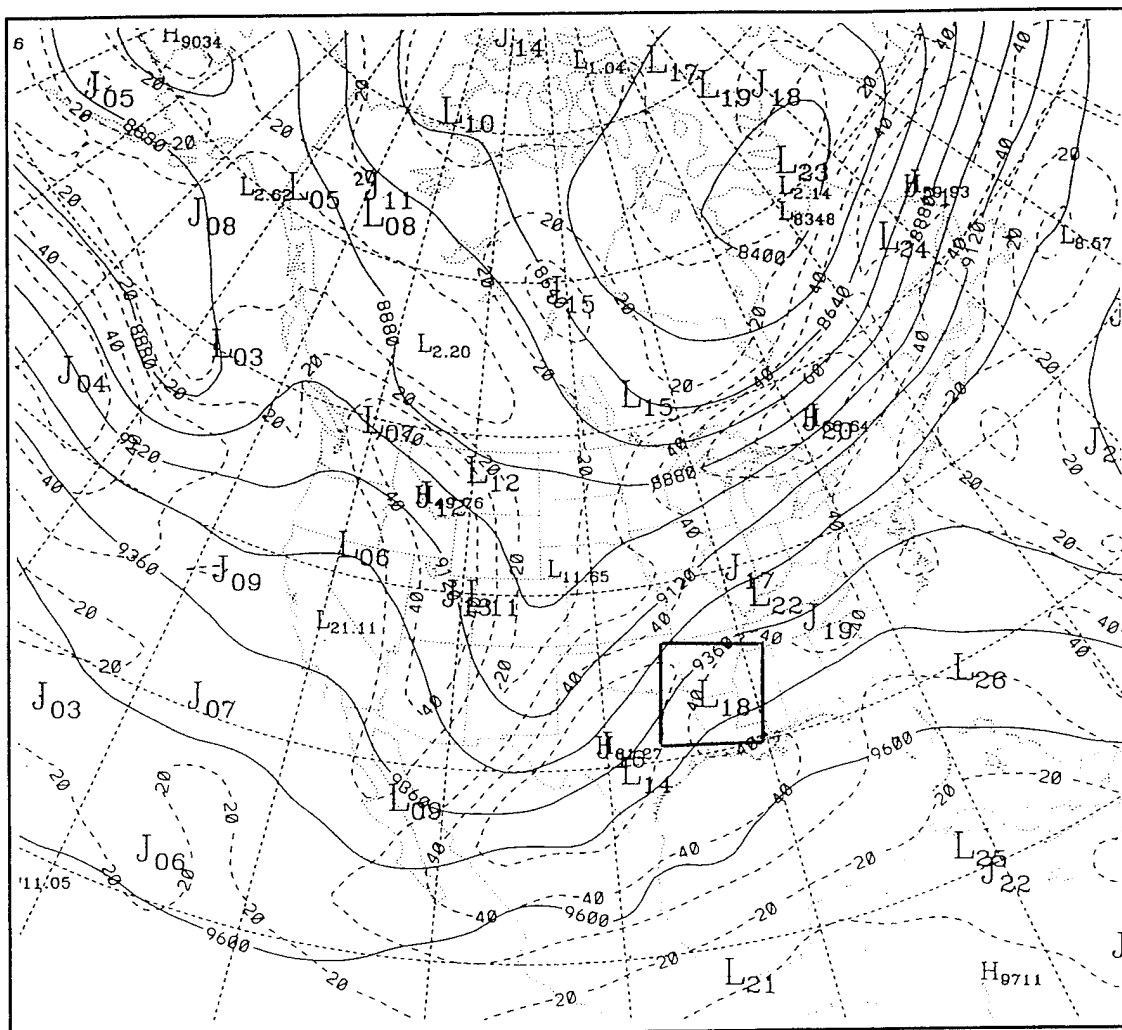


**Figure 41.** Eta model 300 mb height analysis (solid, 12 dm increment) and windspeed (dashed, 10 m/s increment) for 0000 UTC 6 April 1994. A 5 x 5 grid point averaging box is centered over the cyclone of interest labeled L<sub>18</sub>.

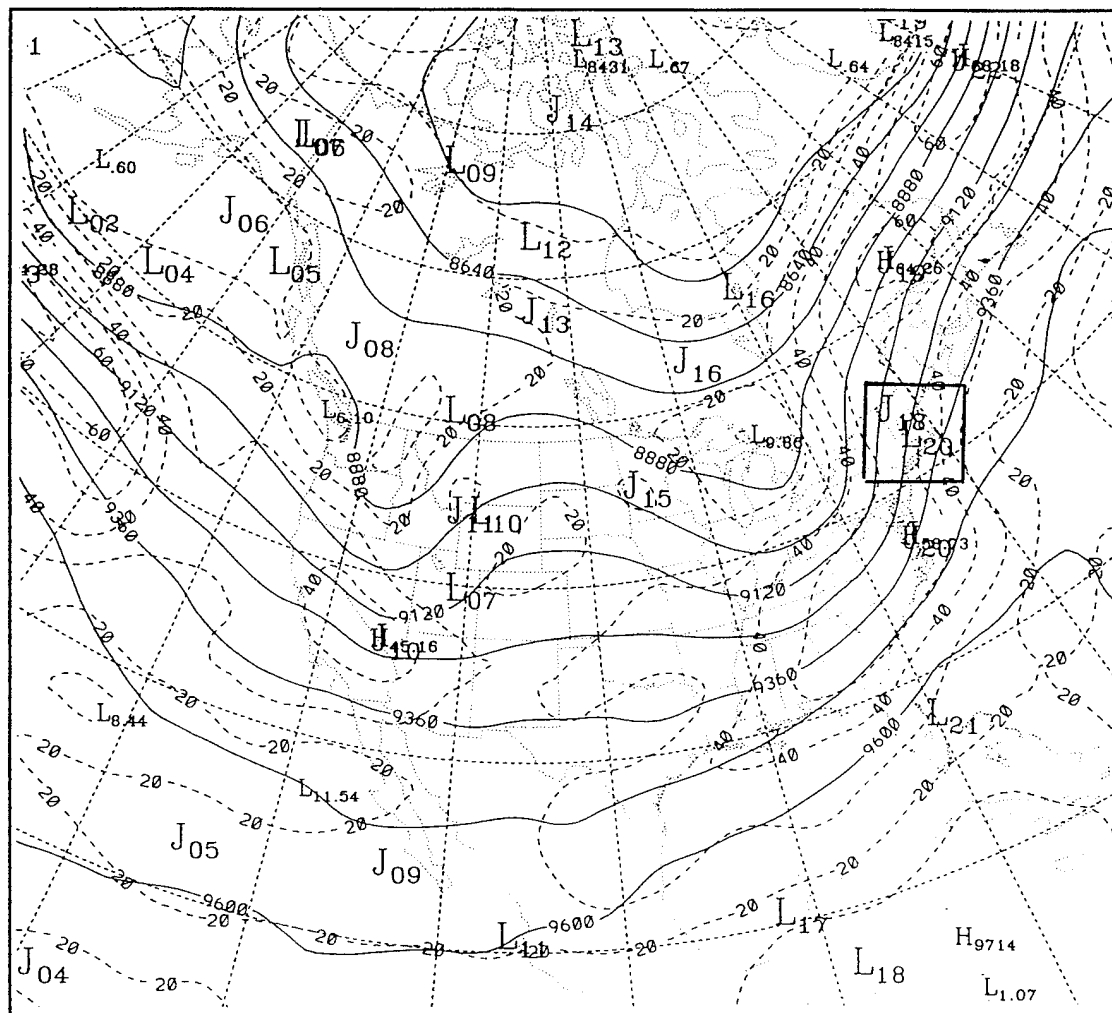


**Figure 42.** As in Figure 41, except for 1200 UTC 7 April 1994 and the cyclone of interest is labeled L<sub>20</sub>.



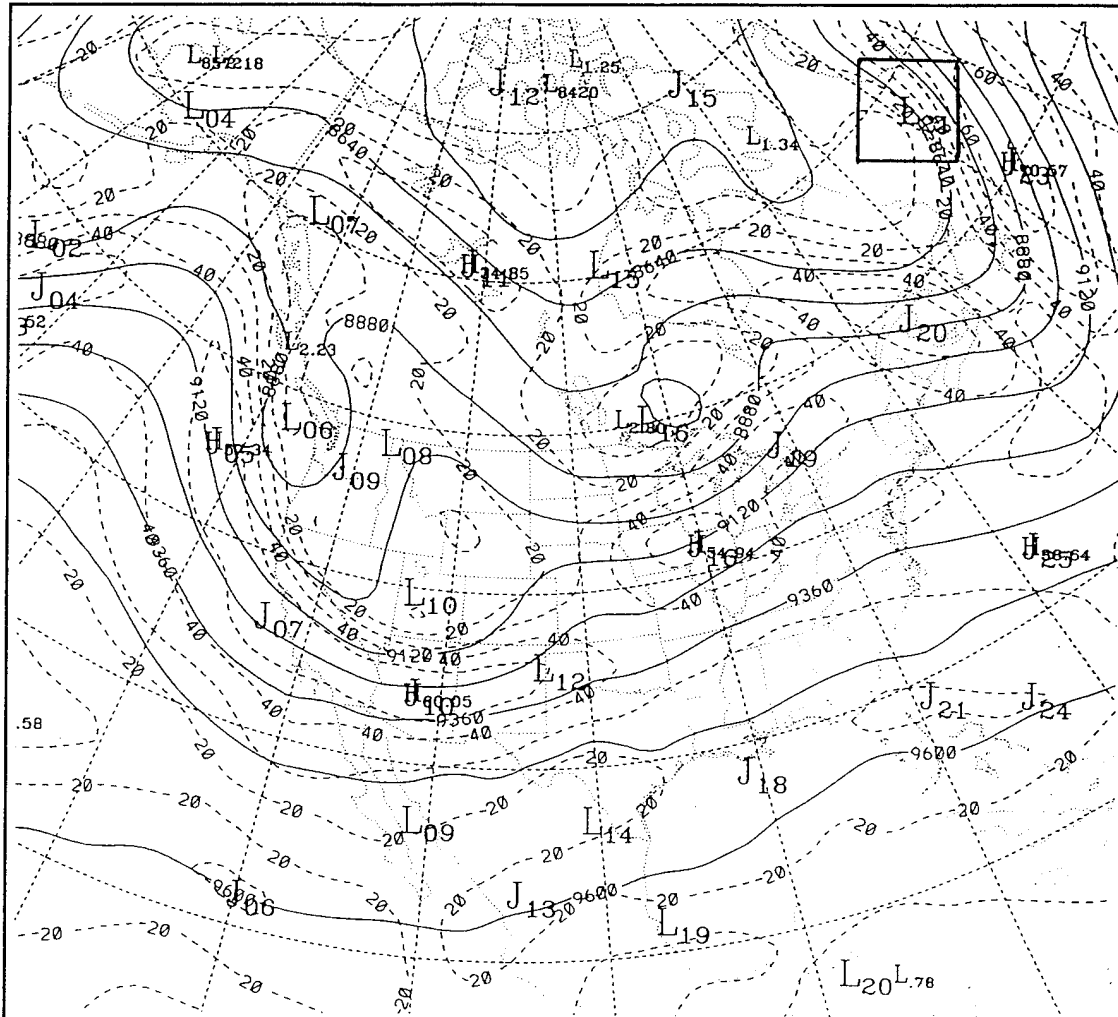


**Figure 43.** As in Figure 41, except for 1200 UTC 9 April 1994 and the cyclone of interest is labeled L<sub>21</sub>.

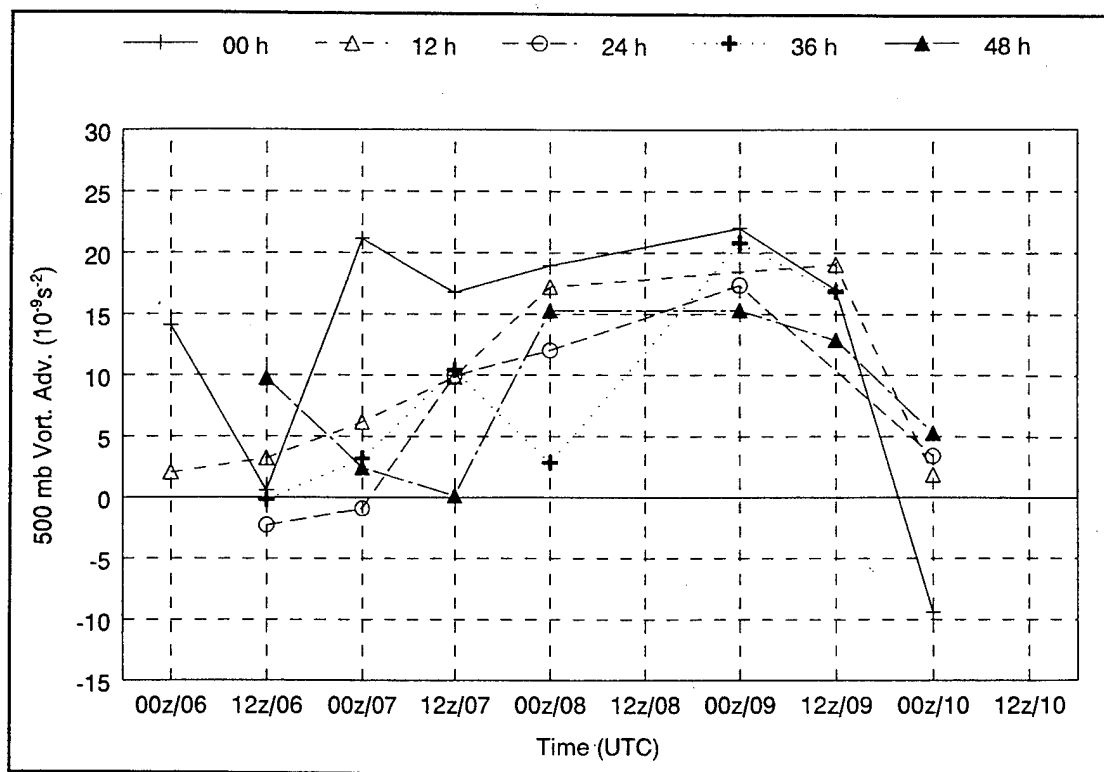


**Figure 44.** Cyclone 165 500 mb vorticity advection trace from 0000 UTC 6 April to 0000 UTC 10 April 1994.

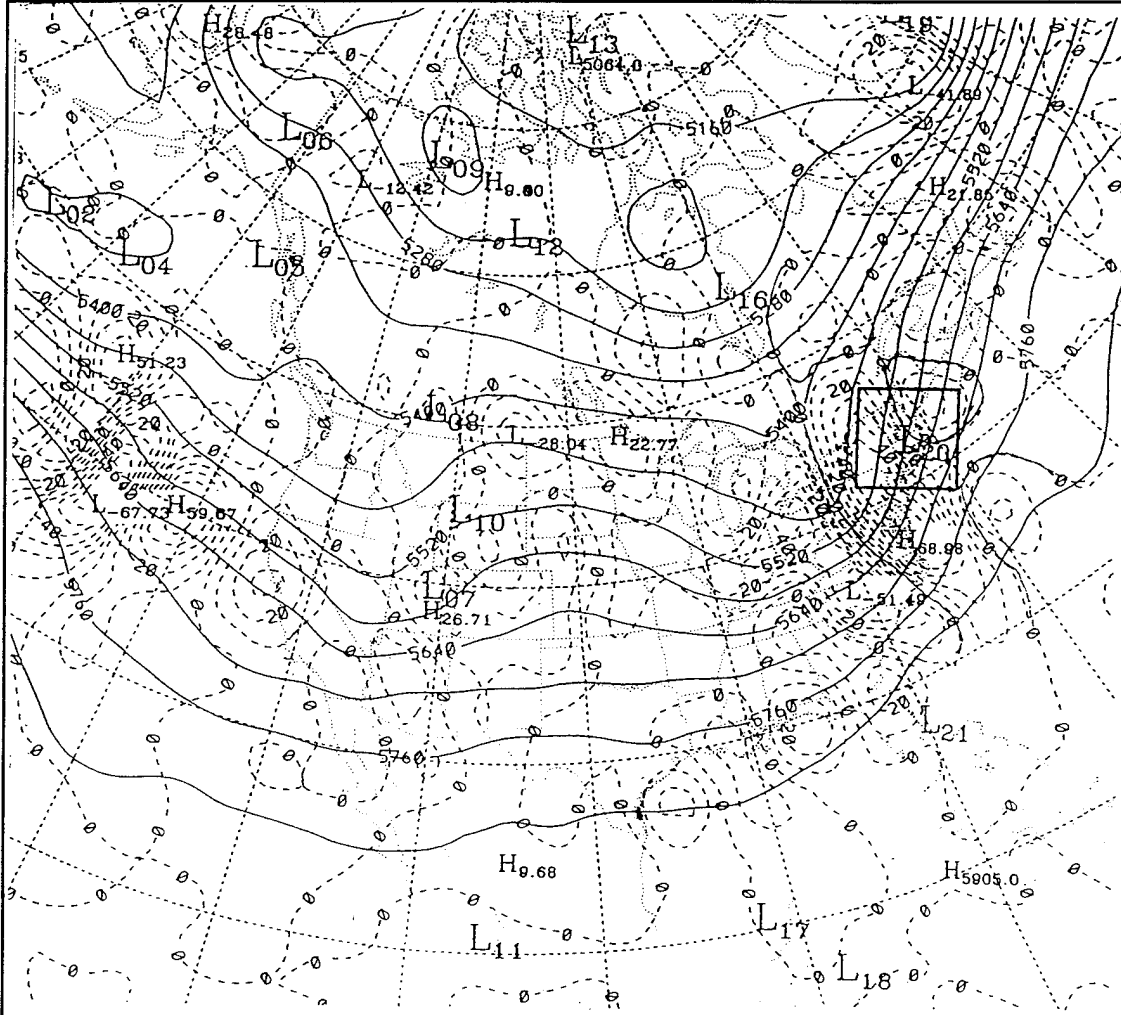


**Figure 45.** Eta model 500 mb height (solid, 120 m increment) and vorticity advection (dashed,  $10 \times 10^{-9} \text{ s}^{-2}$  increment) for 1200 UTC 7 April 1994. A 5 x 5 grid point averaging box is centered over the cyclone of interest.

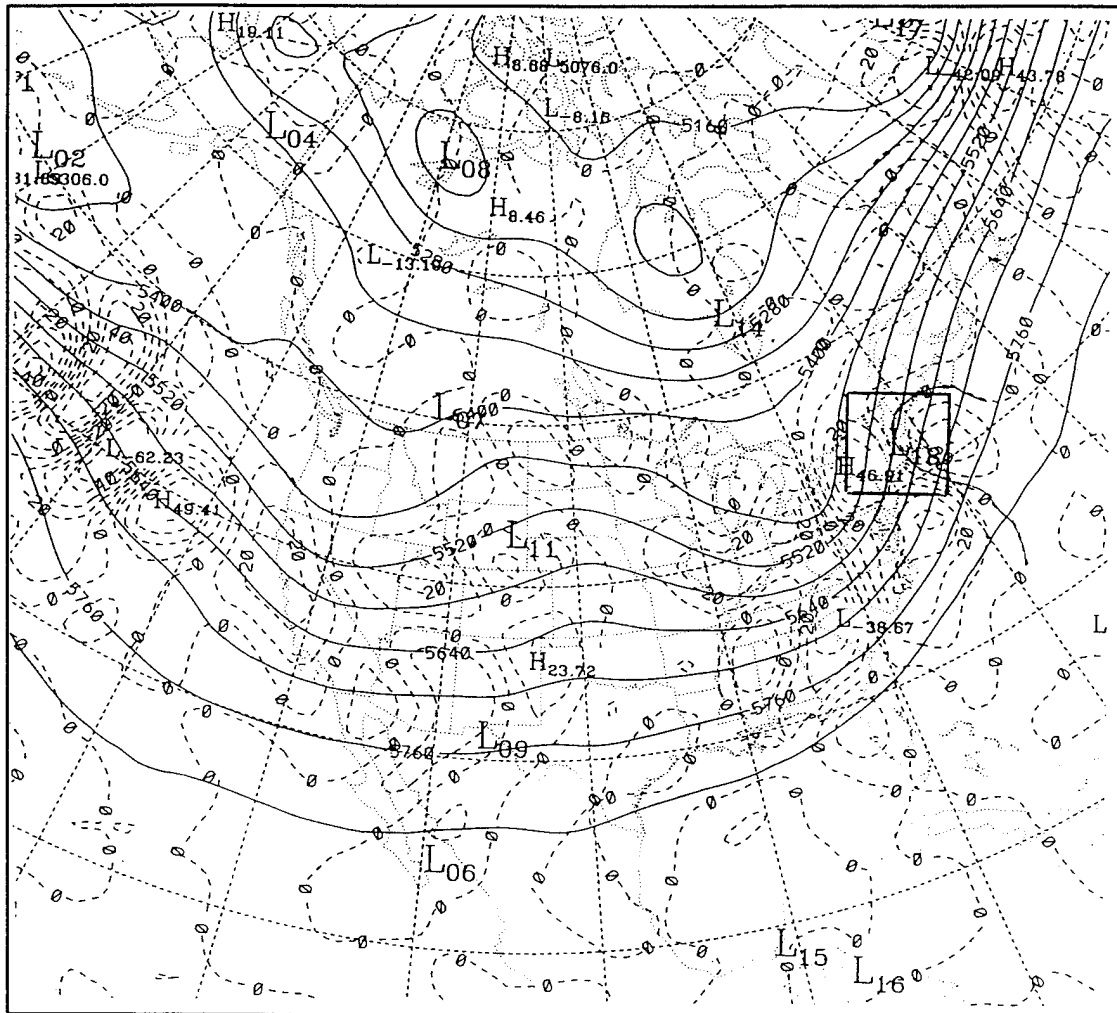


**Figure 46.** As in Figure 45, except for 12 h forecast valid at 1200 UTC 7 April 1994.

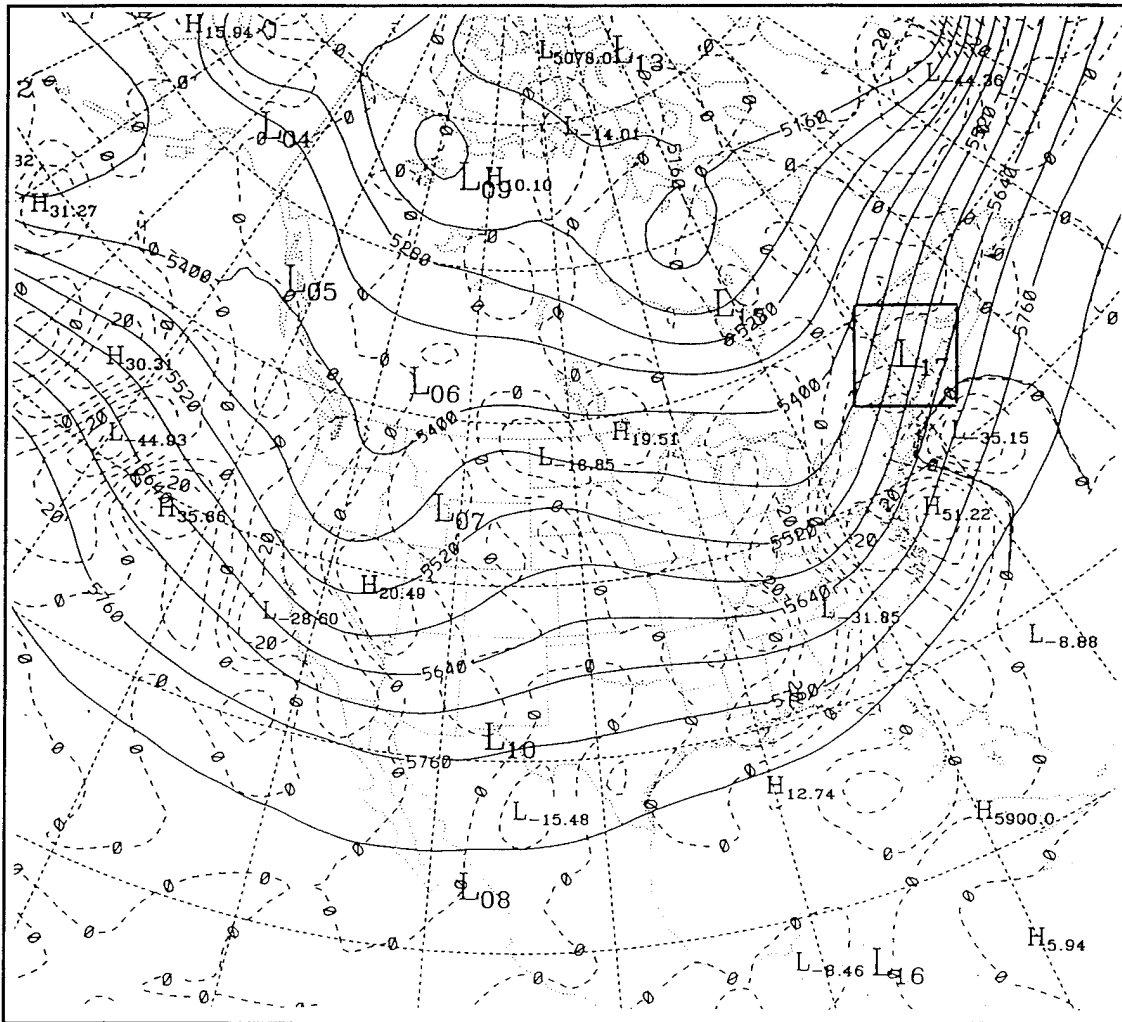


**Figure 47.** As in Figure 45, except for 24 h forecast valid at 1200 UTC 7 April 1994.

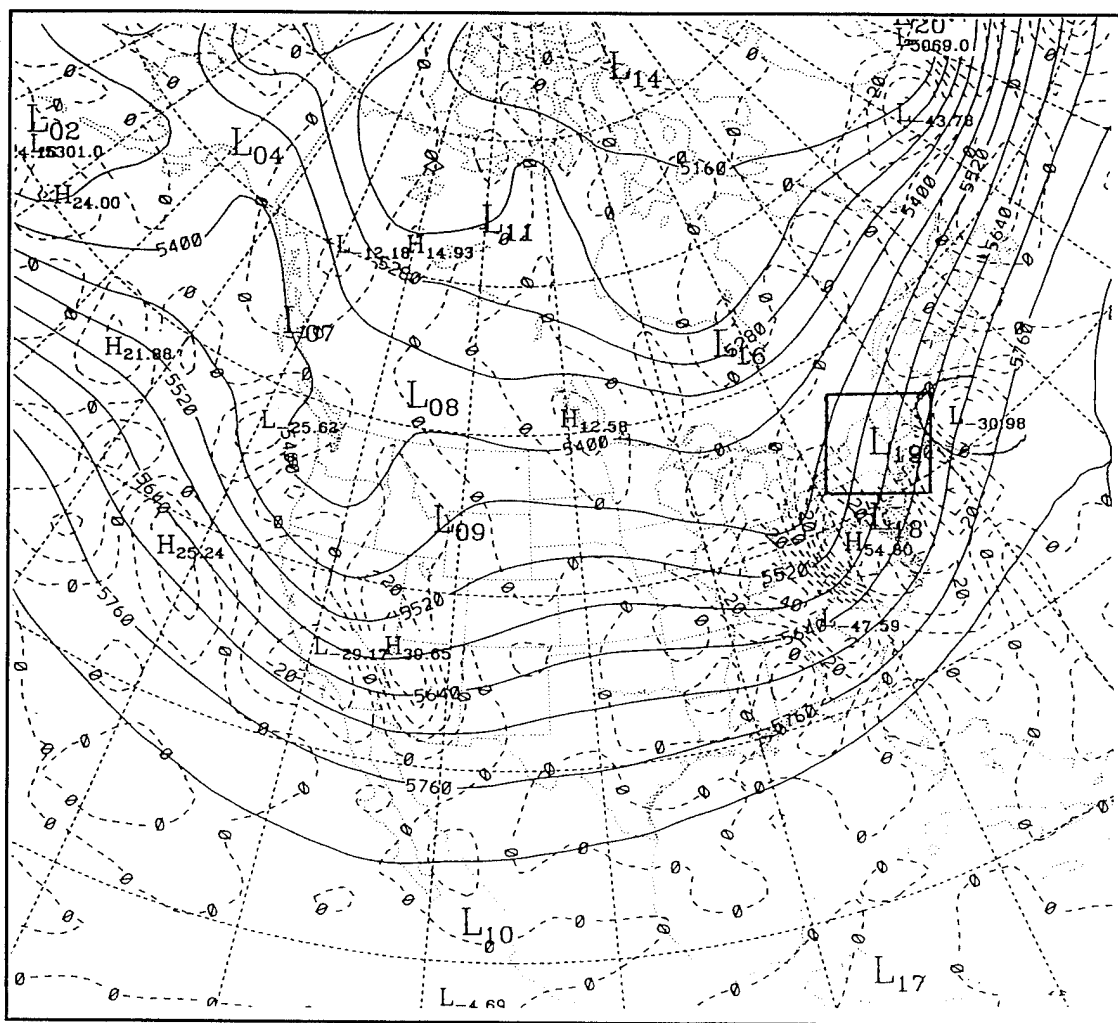


**Figure 48.** As in Figure 45, except for 36 h forecast valid at 1200 UTC 7 April 1994.

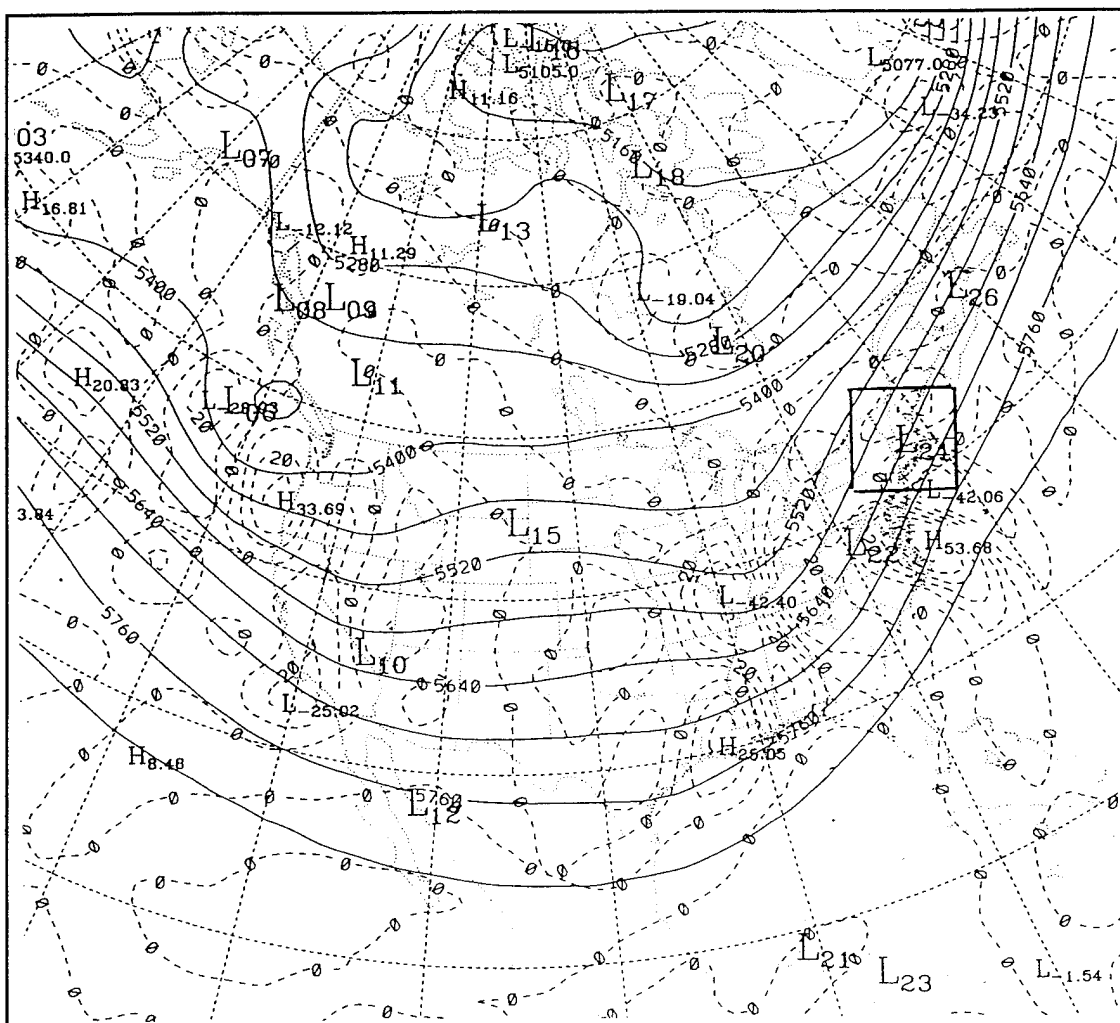
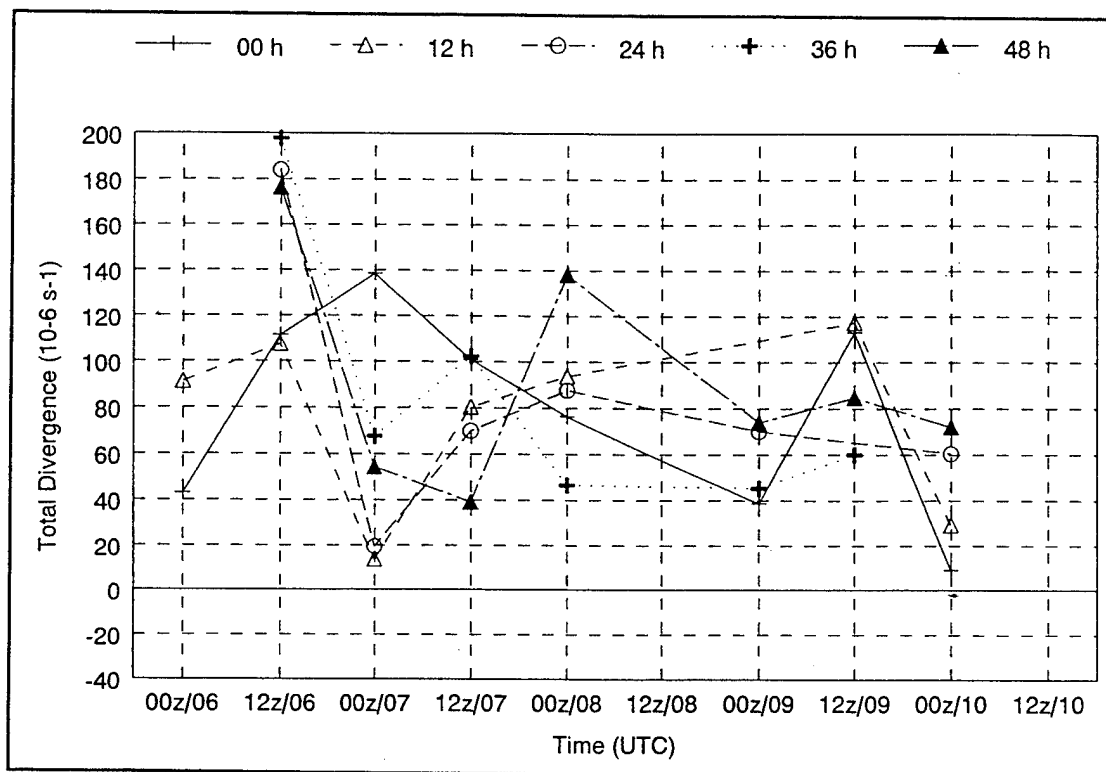
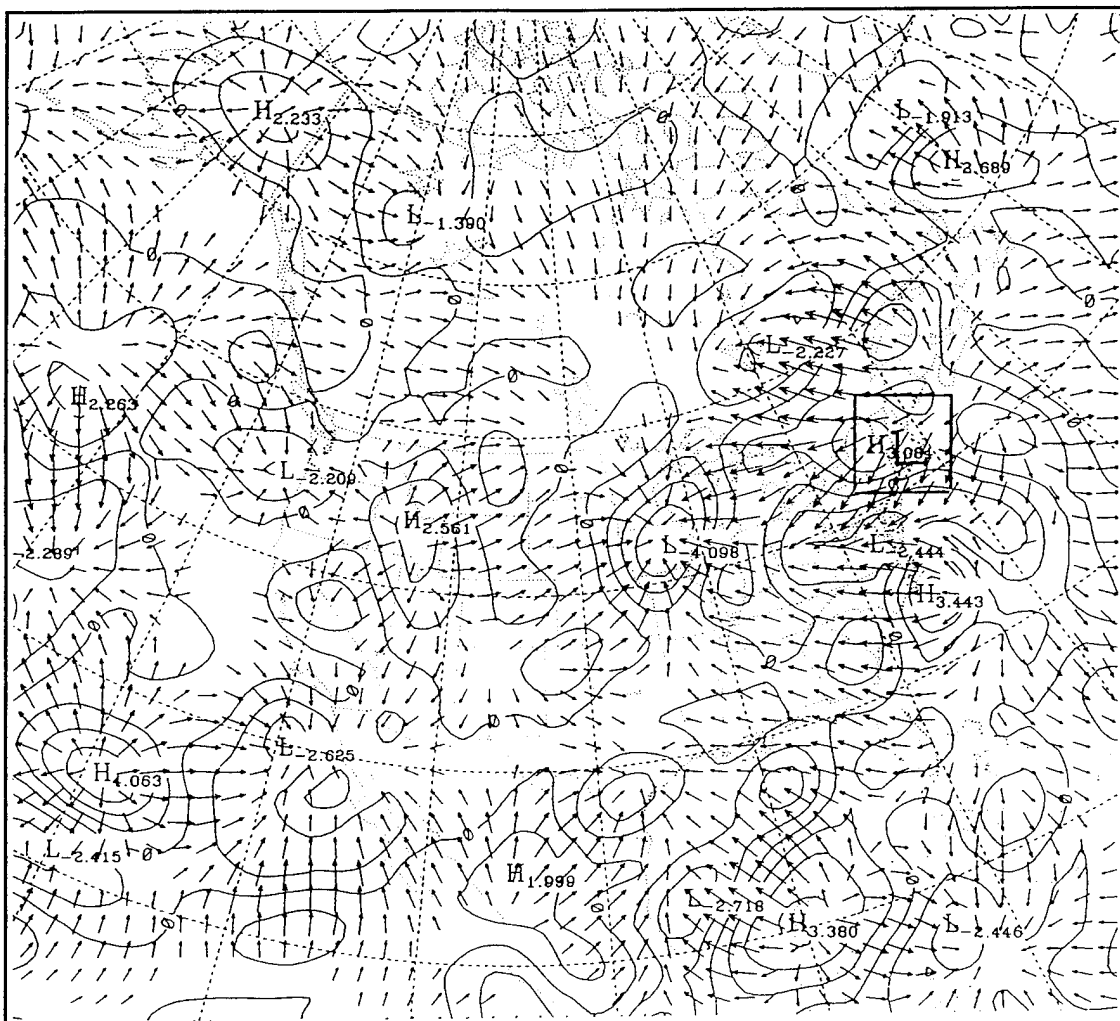


Figure 49. As in Figure 45, except for 48 h forecast valid at 1200 UTC 7 April 1994.

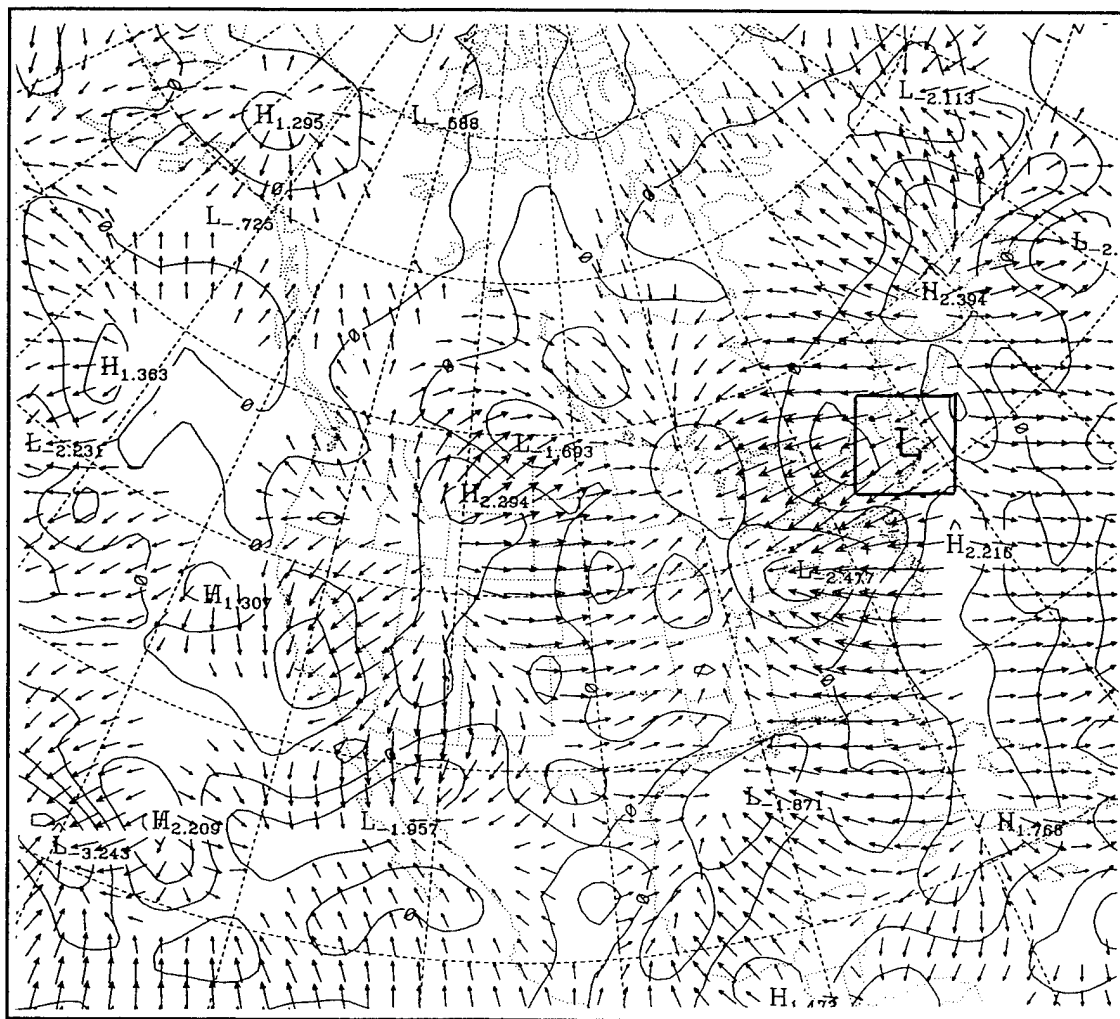


**Figure 50.** Cyclone 165 total divergence trace from 0000 UTC 6 April to 0000 UTC 10 April 1994.

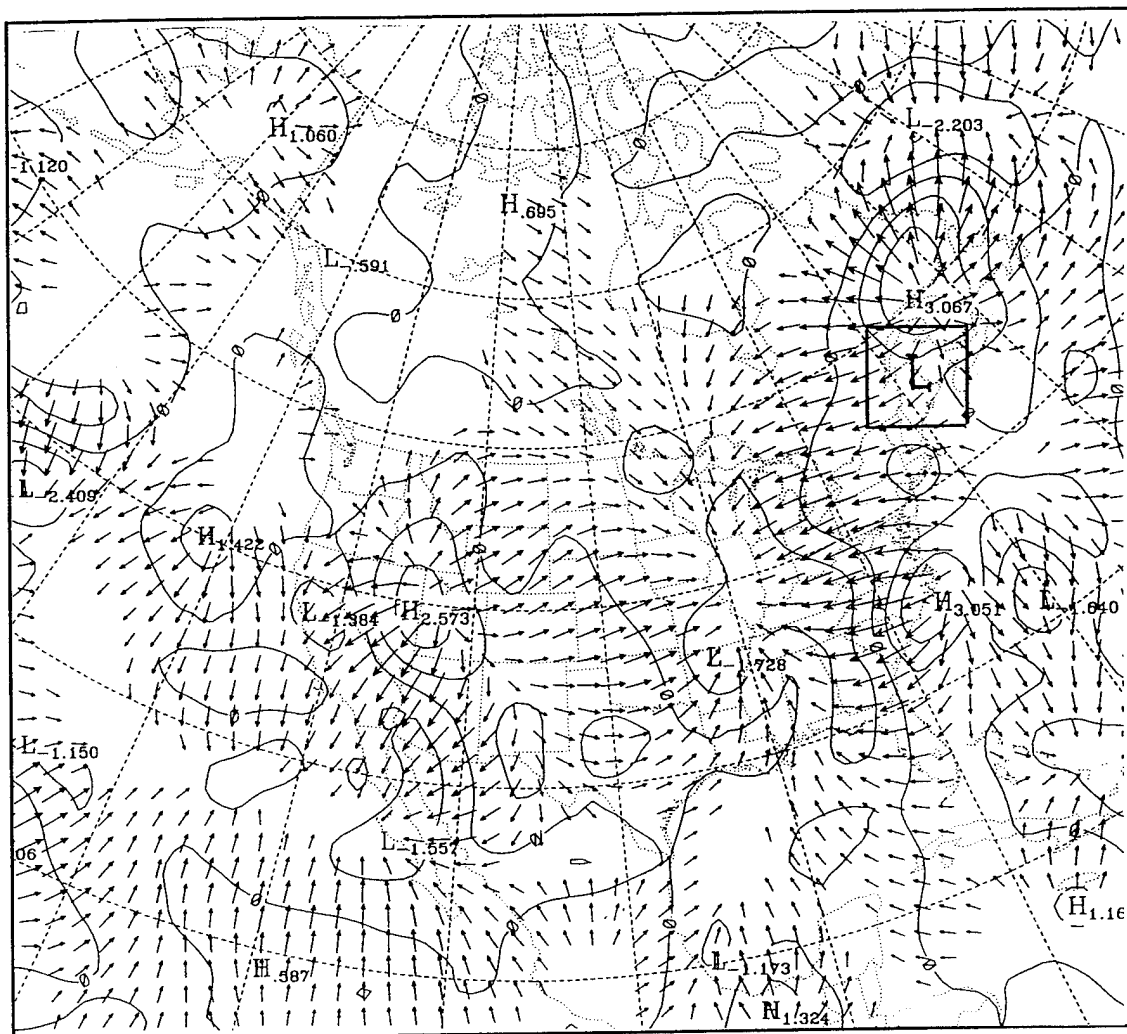




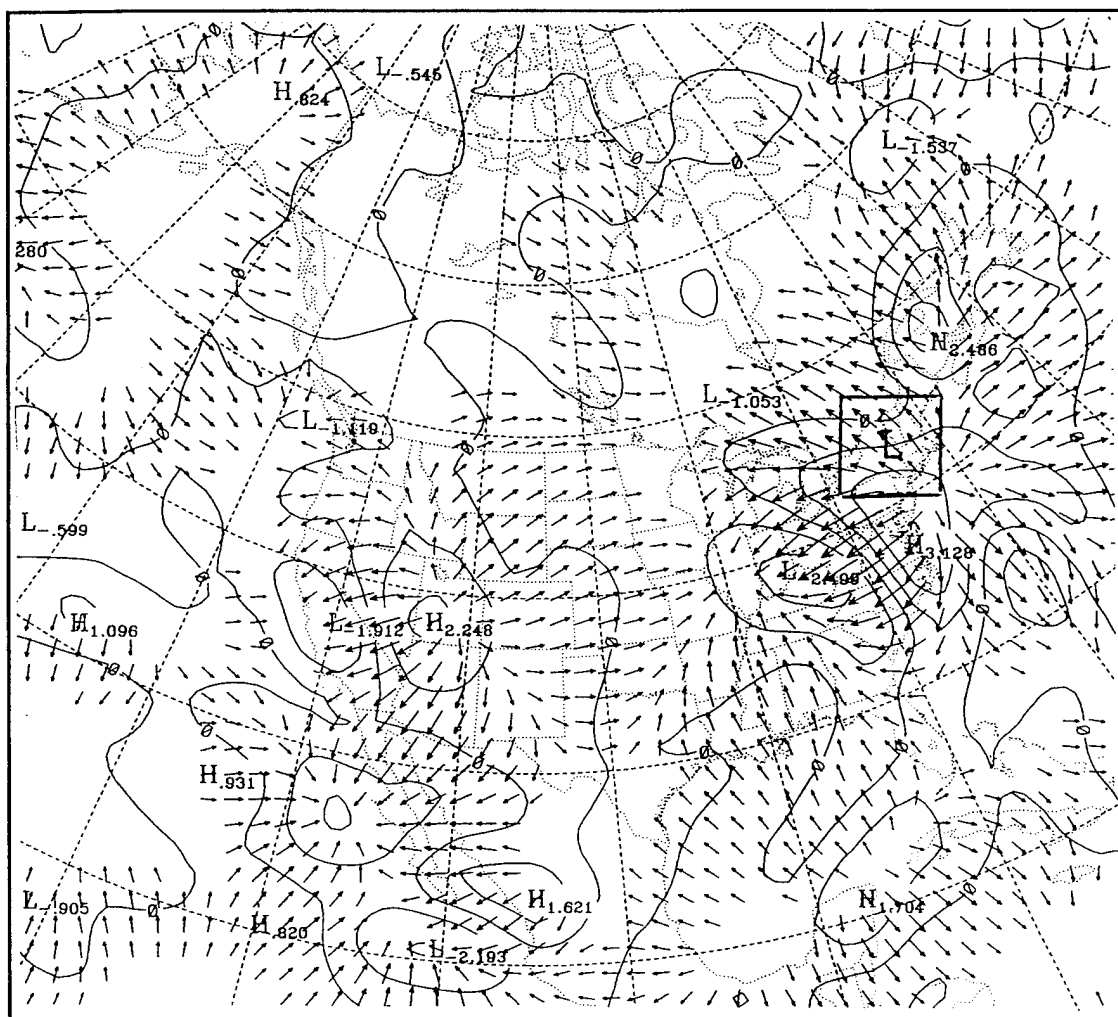
**Figure 51.** Eta model 300 mb total divergence (solid, 10 x 10<sup>-6</sup> s<sup>-1</sup> increment) and vectors of divergent ageostrophic wind (1.0 to 8.5 m/s) for 1200 UTC 7 April 1994. The maximum (H) and minimum (L) are labeled as 10<sup>-6</sup> s<sup>-1</sup>. A 5 x 5 grid point averaging box is centered over the cyclone of interest.



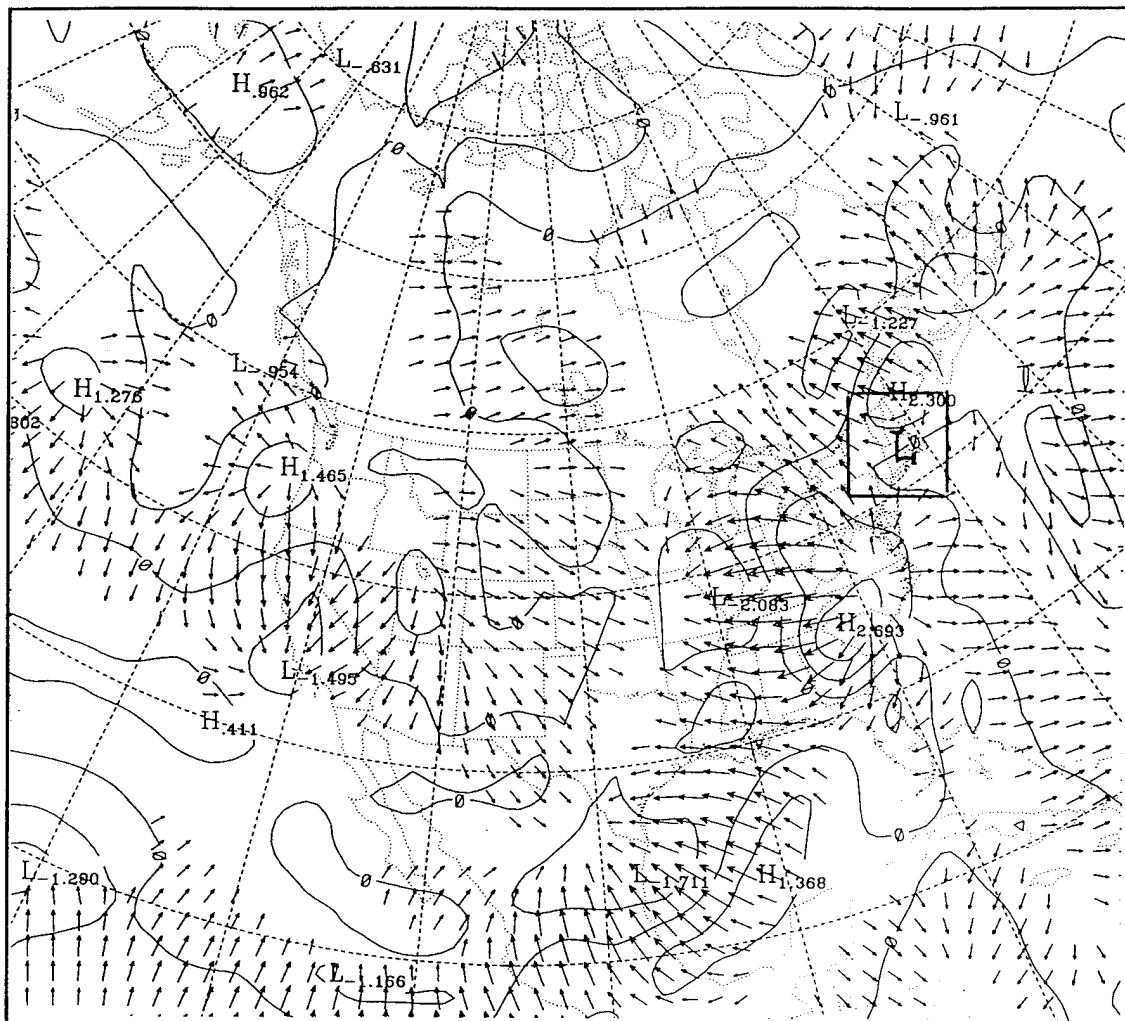
**Figure 52.** As in Figure 51, except for 12 h forecast valid at 1200 UTC 7 April 1994.



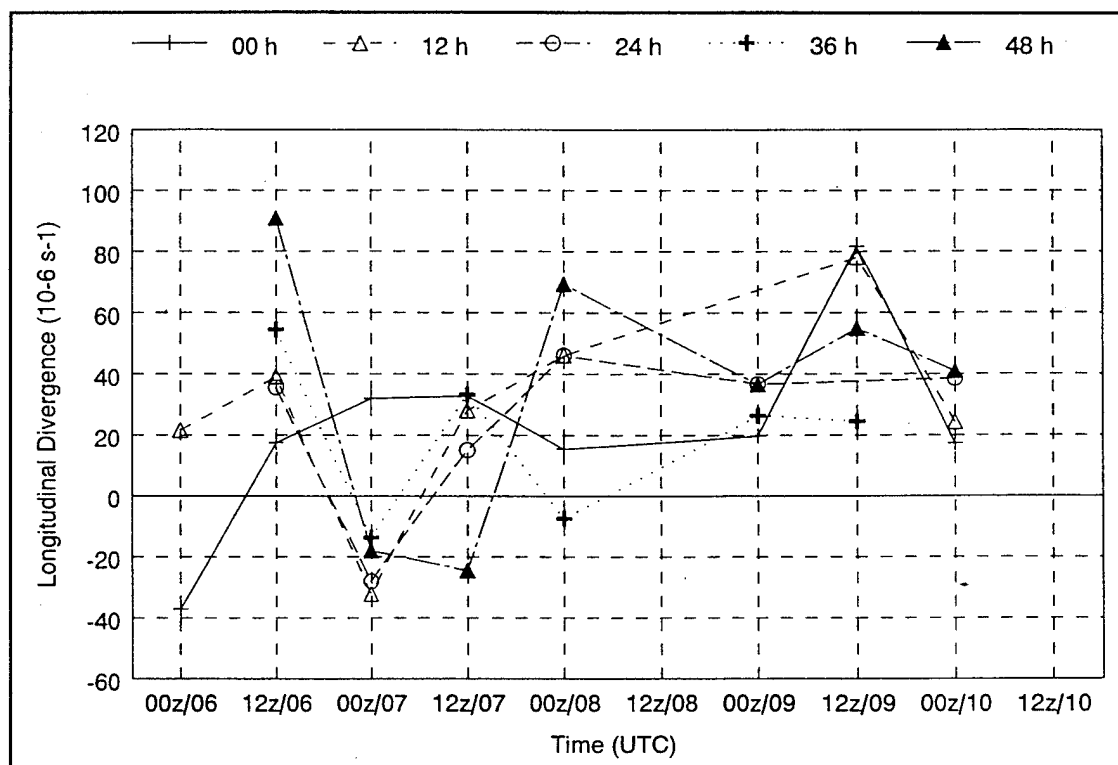
**Figure 53.** As in Figure 51, except for 24 h forecast valid at 1200 UTC 7 April 1994.



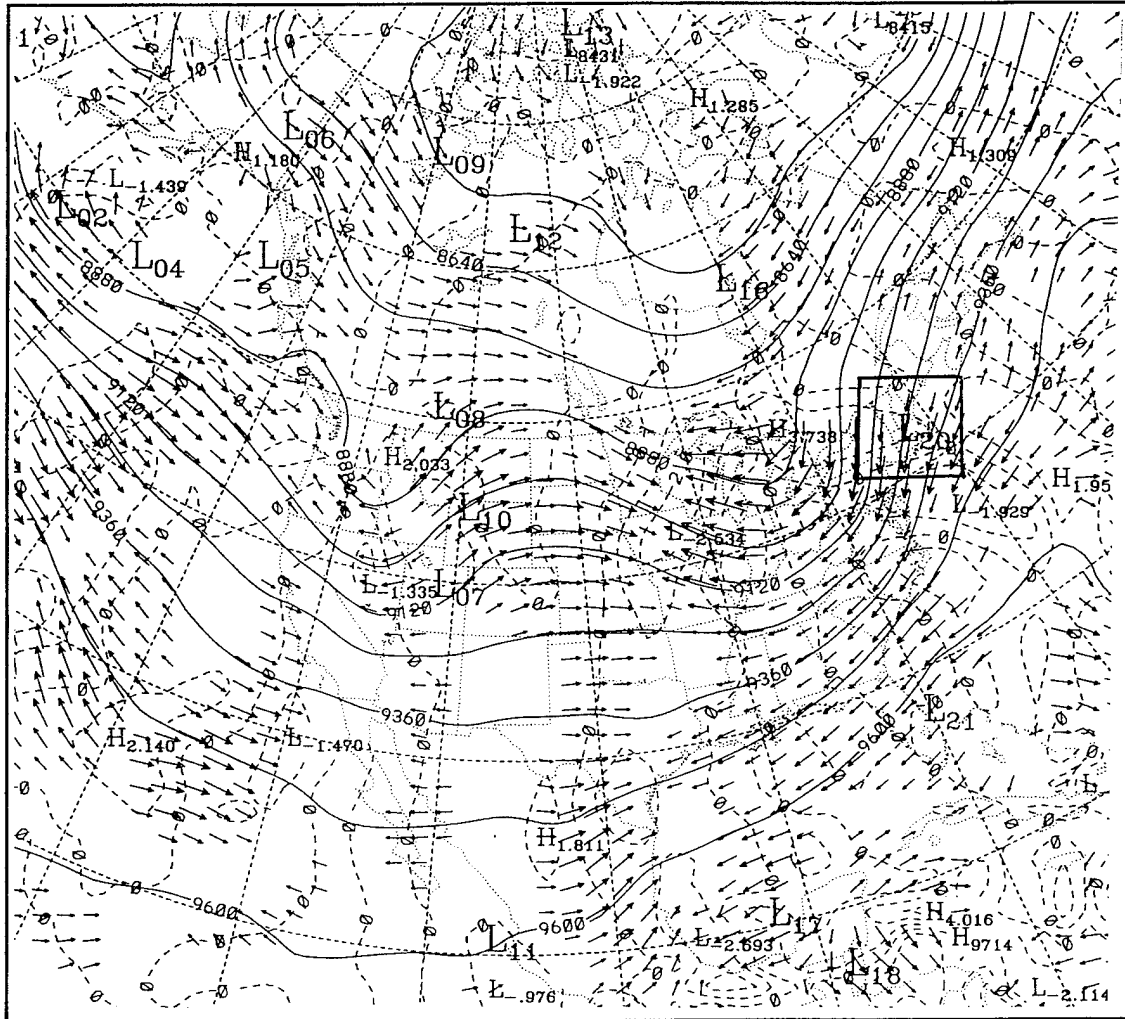
**Figure 54.** As in Figure 51, except for 36 h forecast valid at 1200 UTC 7 April 1994.

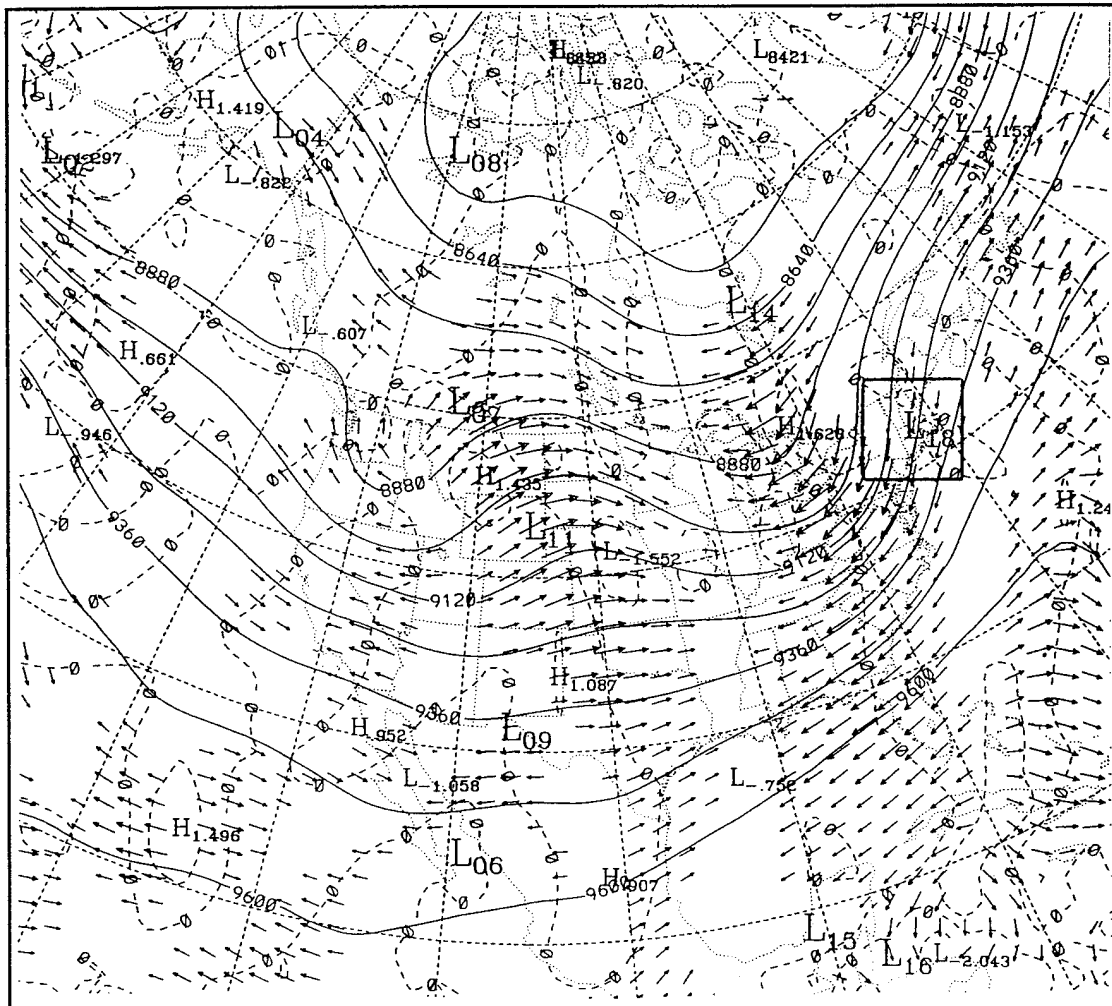


**Figure 55.** As in Figure 51, except for 48 h forecast valid at 1200 UTC 7 April 1994.



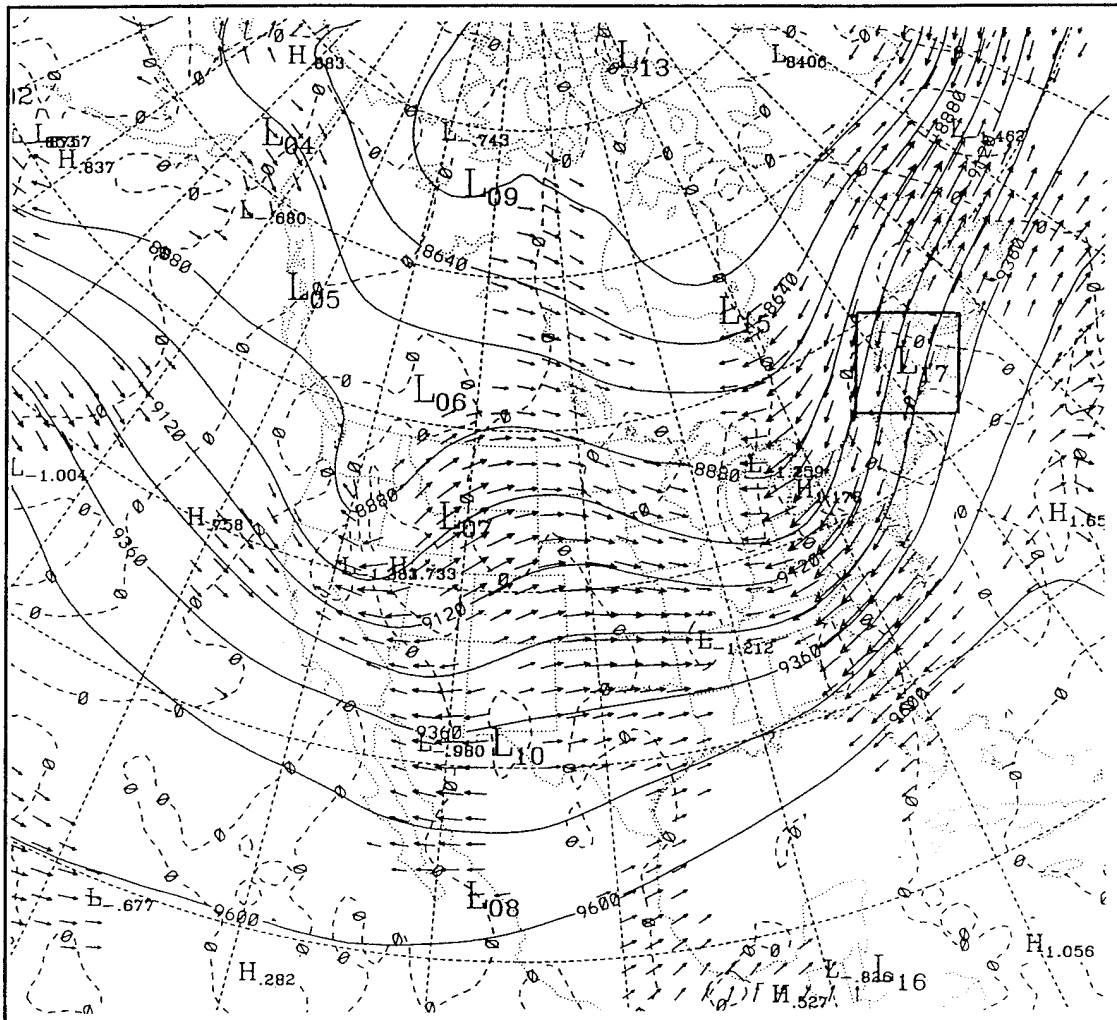
**Figure 56.** Cyclone 165 longitudinal divergence trace from 0000 UTC 6 April to 0000 UTC 10 April 1994.



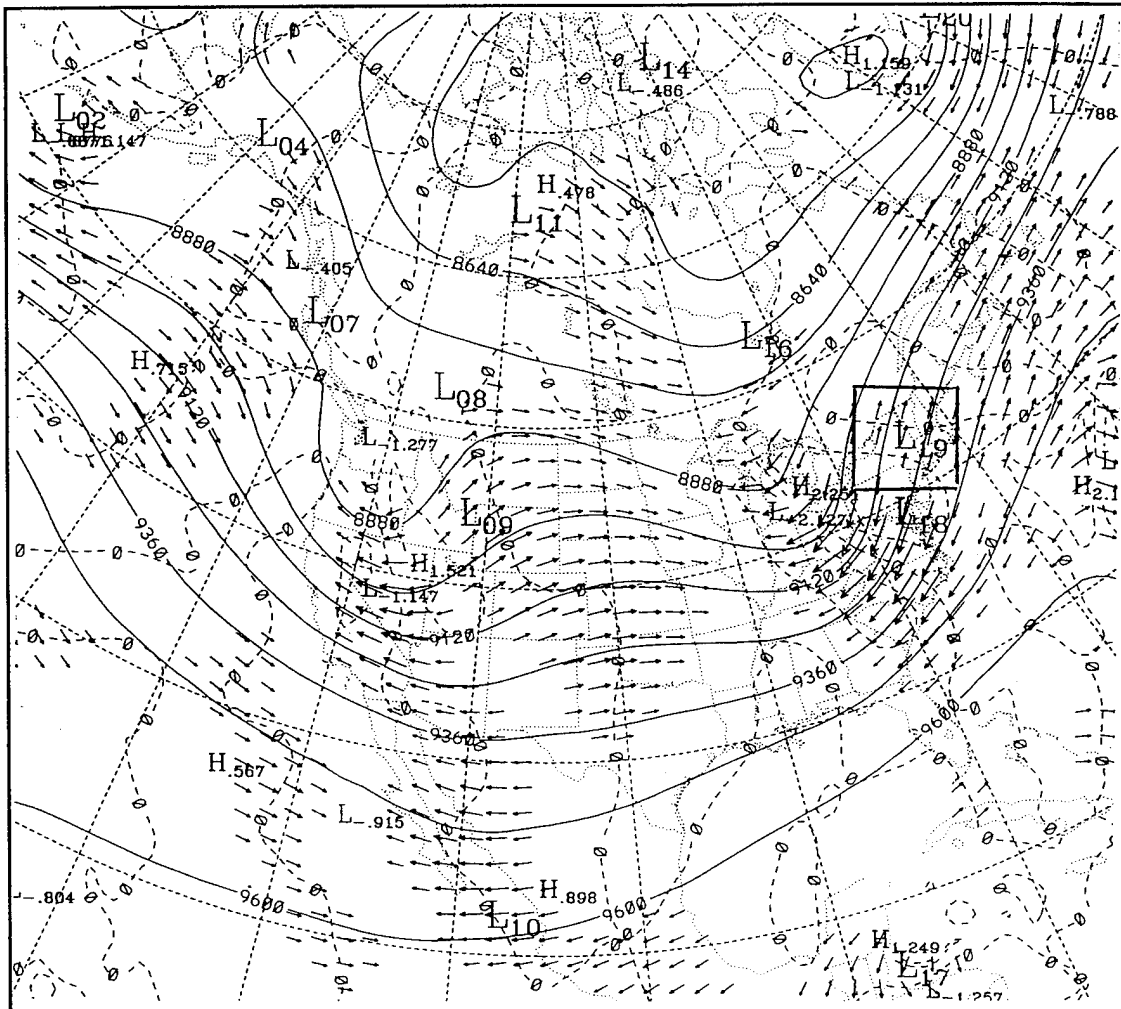


**Figure 58.** As in Figure 57, except for 12 h forecast valid at 1200 UTC 7 April 1994.

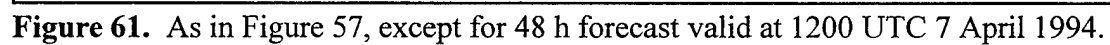


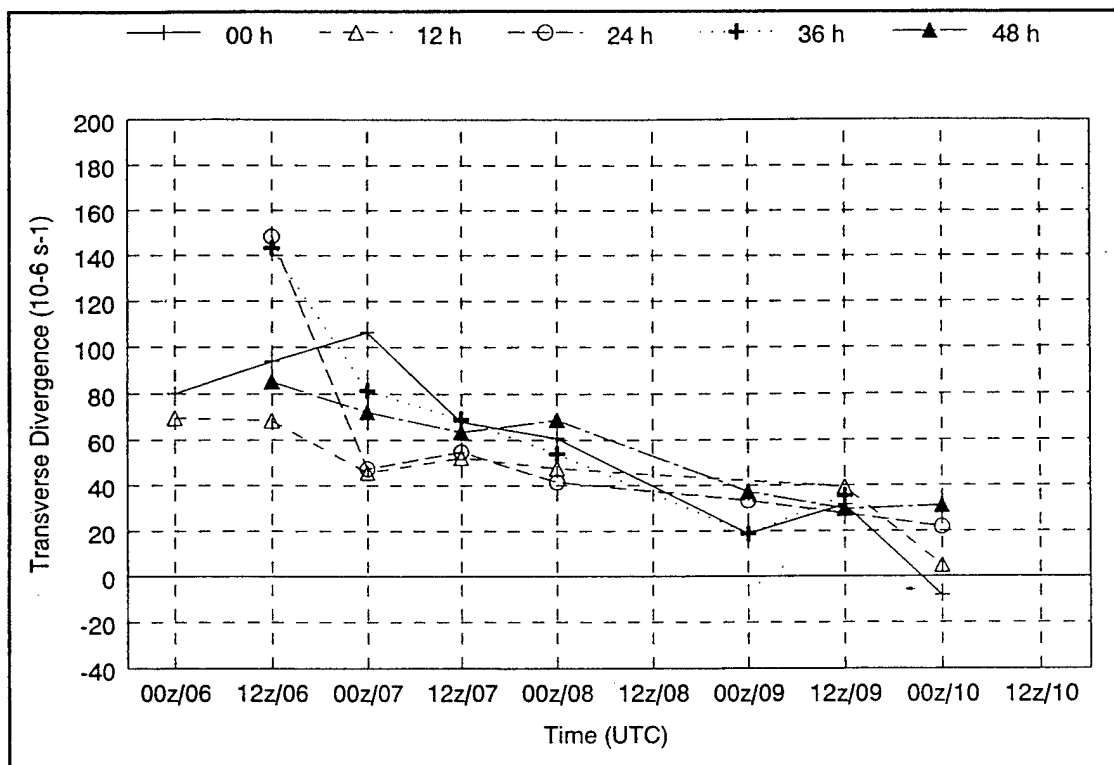


**Figure 59.** As in Figure 57, except for 24 h forecast valid at 1200 UTC 7 April 1994.

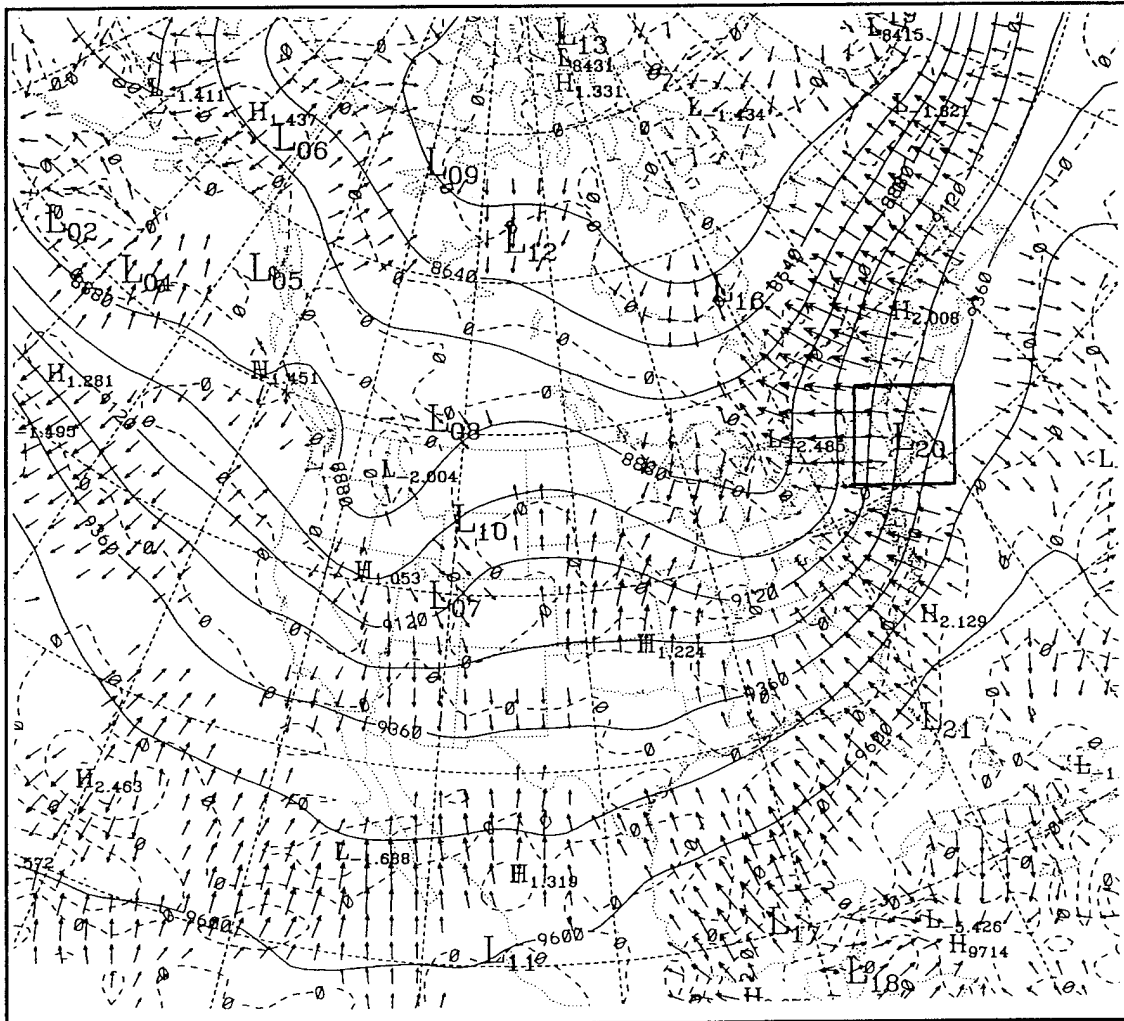


**Figure 60.** As in Figure 57, except for 36 h forecast valid at 1200 UTC 7 April 1994.





**Figure 62.** Cyclone 165 transverse divergence trace from 0000 UTC 6 April to 0000 UTC 10 April 1994.



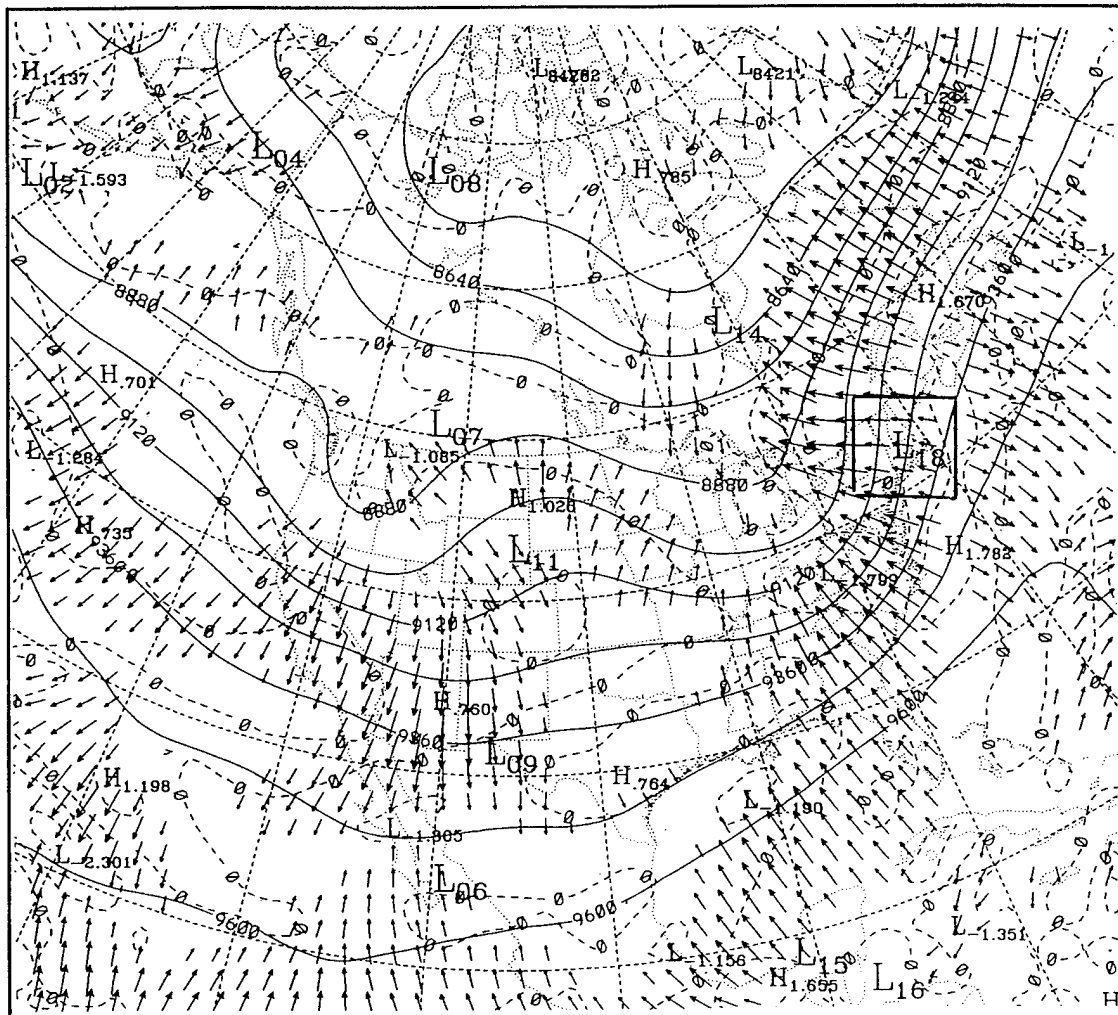


Figure 64. As in Figure 63, except for 12 h forecast valid at 1200 UTC 7 April 1994.

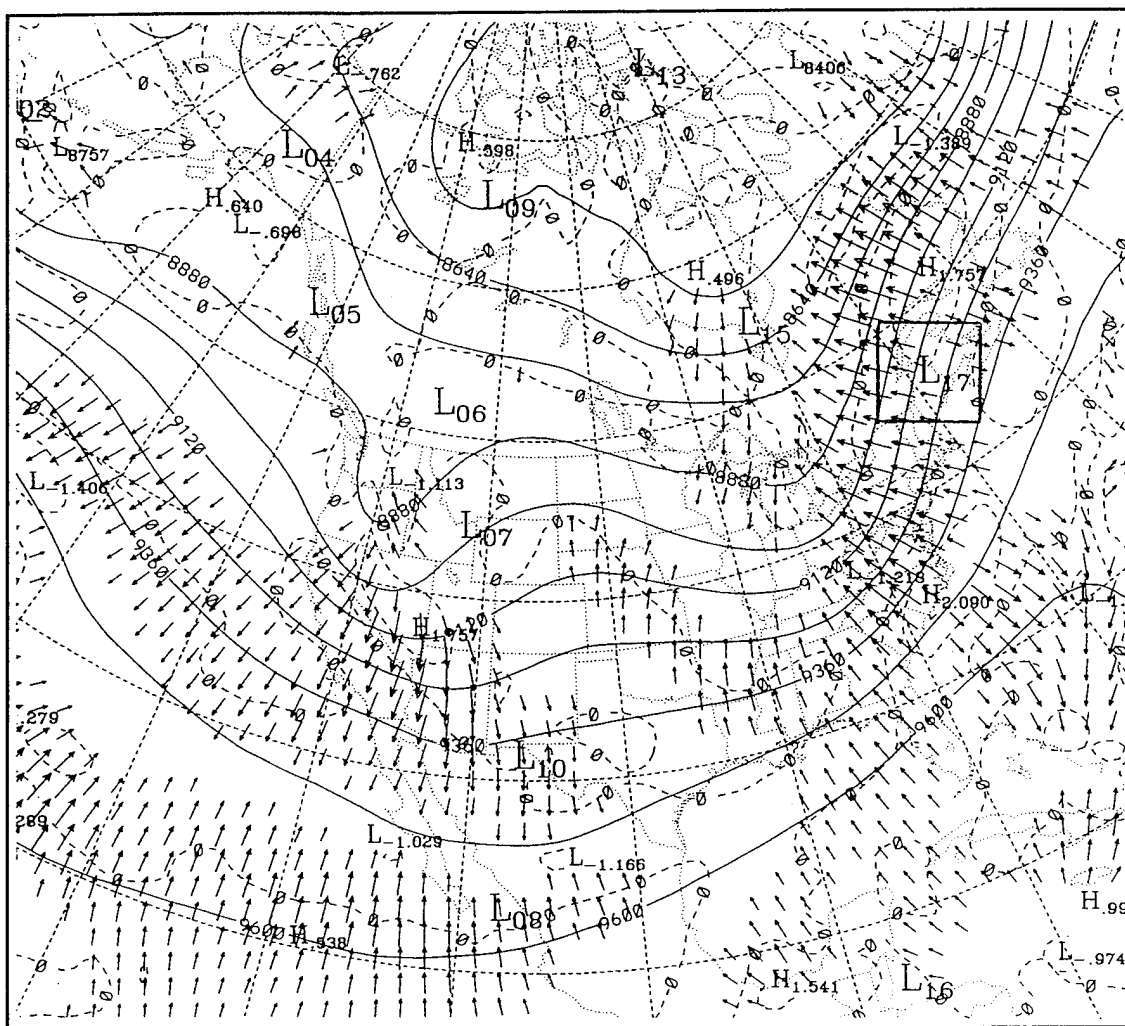
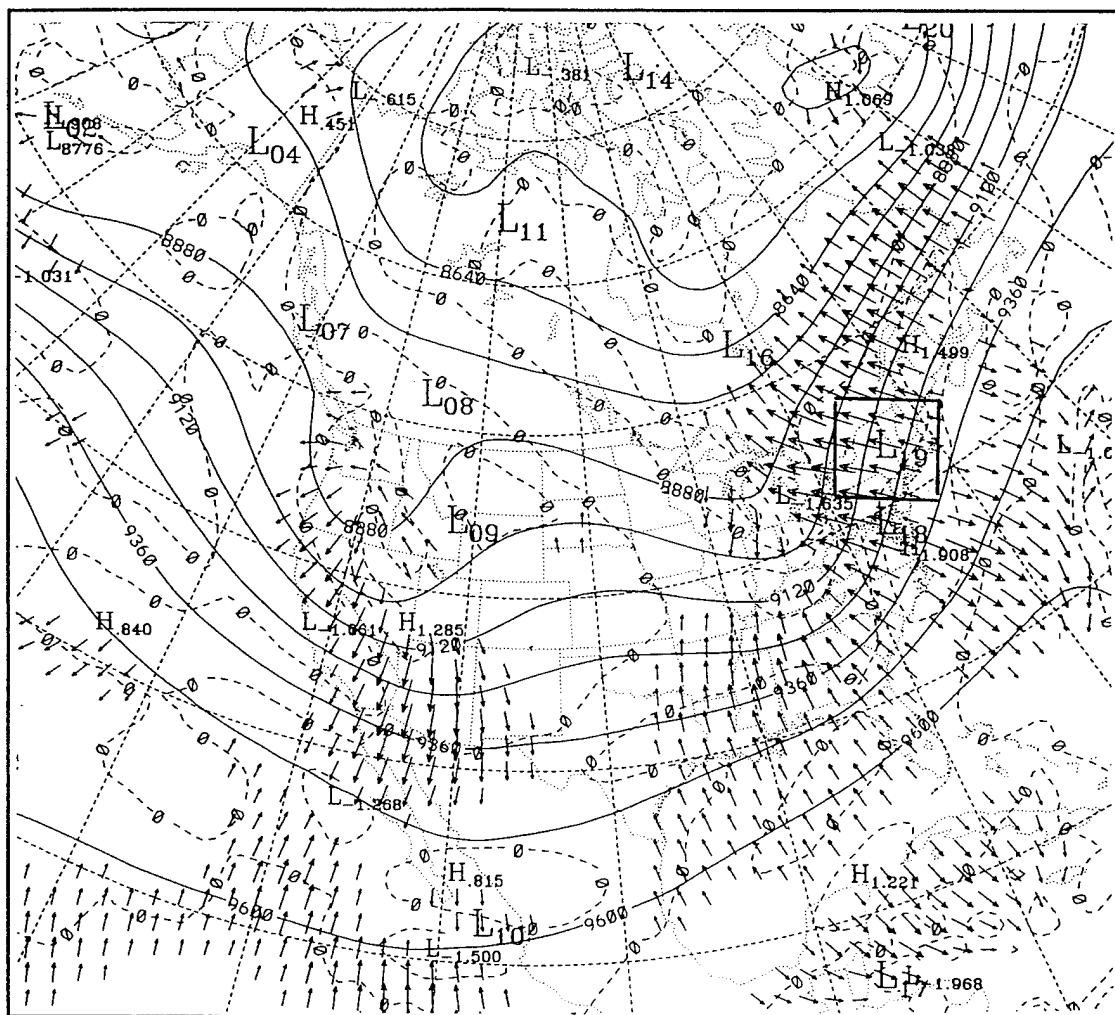


Figure 65. As in Figure 63, except for 24 h forecast valid at 1200 UTC 7 April 1994.



**Figure 66.** As in Figure 63, except for 36 h forecast valid at 1200 UTC 7 April 1994.



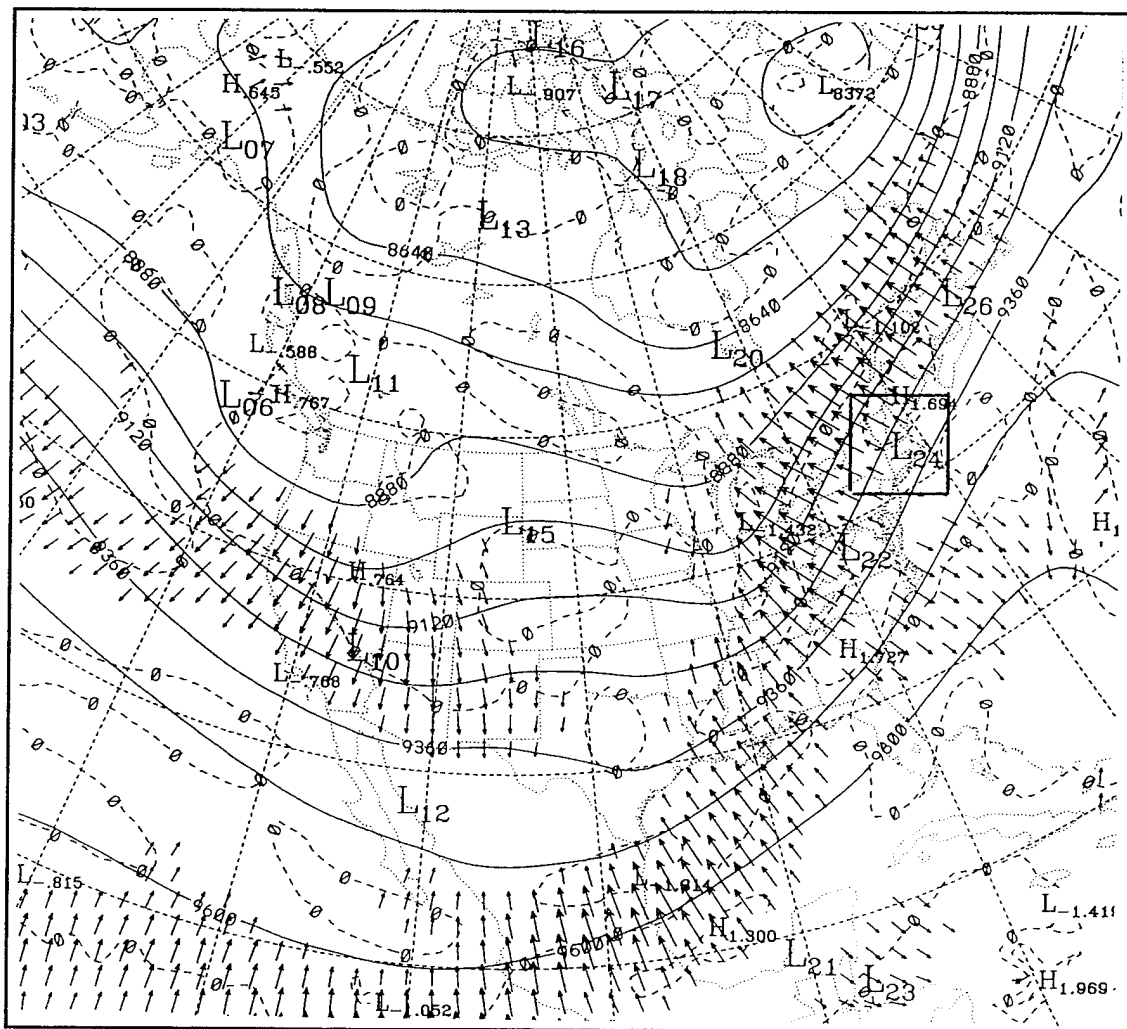
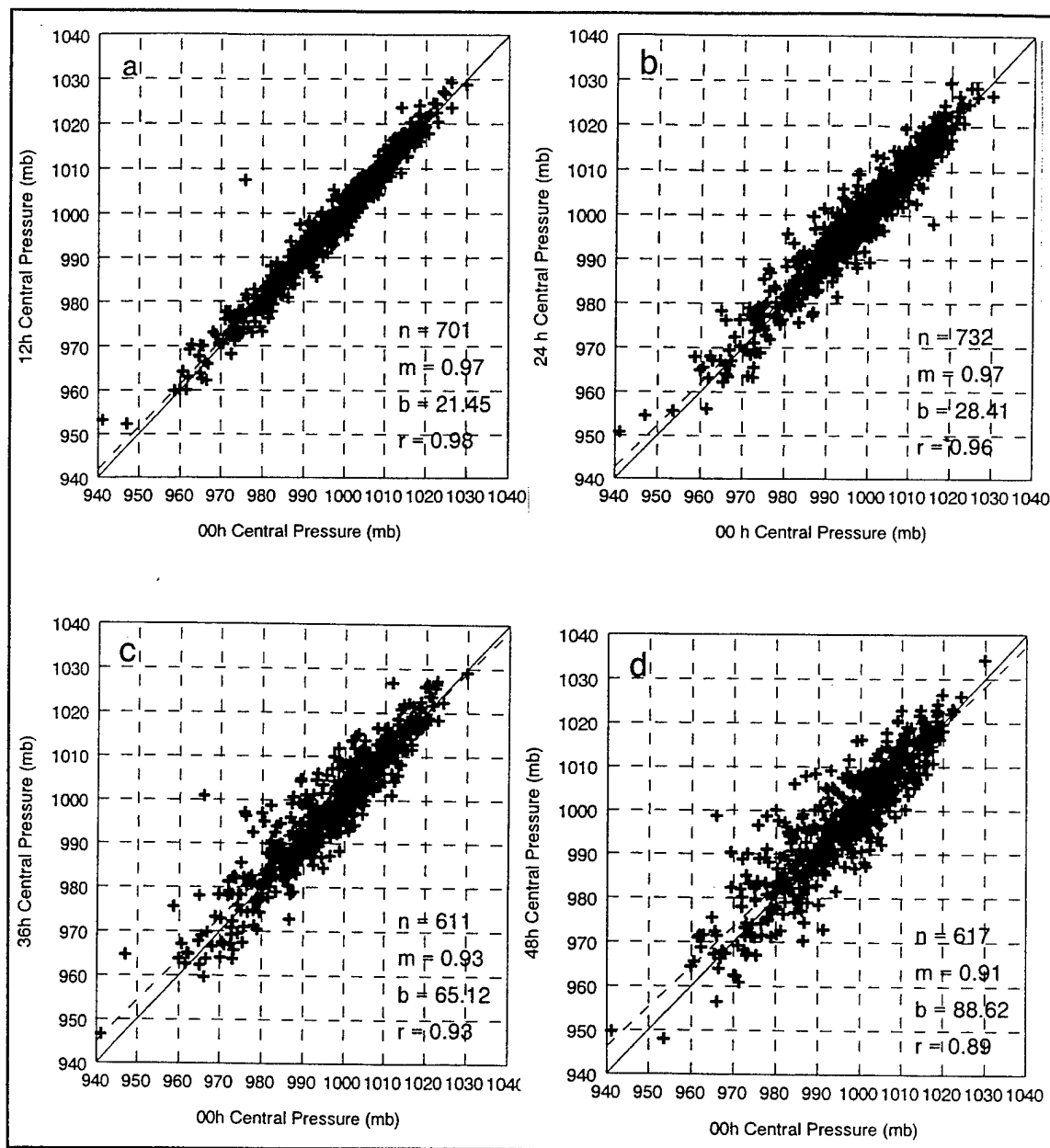
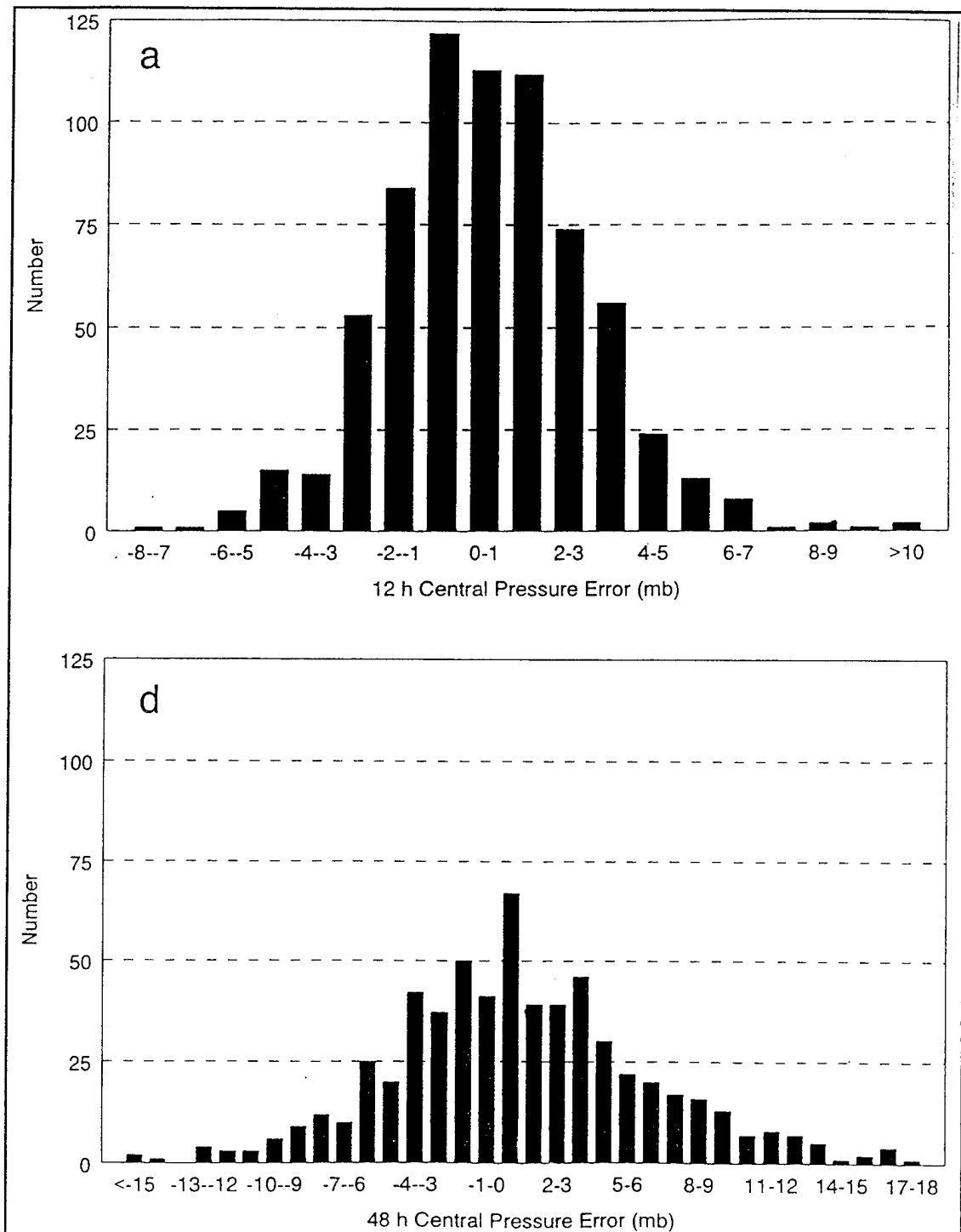


Figure 67. As in Figure 63, except for 48 h forecast valid at 1200 UTC 7 April 1994.



**Figure 68.** Scatter diagrams depicting Eta model analyzed (00 h) cyclone central pressure vs forecast values; (a) 12 h forecast; (b) 24 h forecast; (c) 36 h forecast; and (d) 48 h forecast. ("n" is the number of points, "m" is the slope of the solid line, "b" is the y-intercept, and "r" is the correlation coefficient.) The diagonal (solid) is the least-square best fit, and the diagonal (dashed) is the perfect least-square fit with a slope of one and a y-intercept of zero.



**Figure 69.** Central pressure error (mb) vs number of points: (a) 12 h forecast; (b) 48 h forecast.

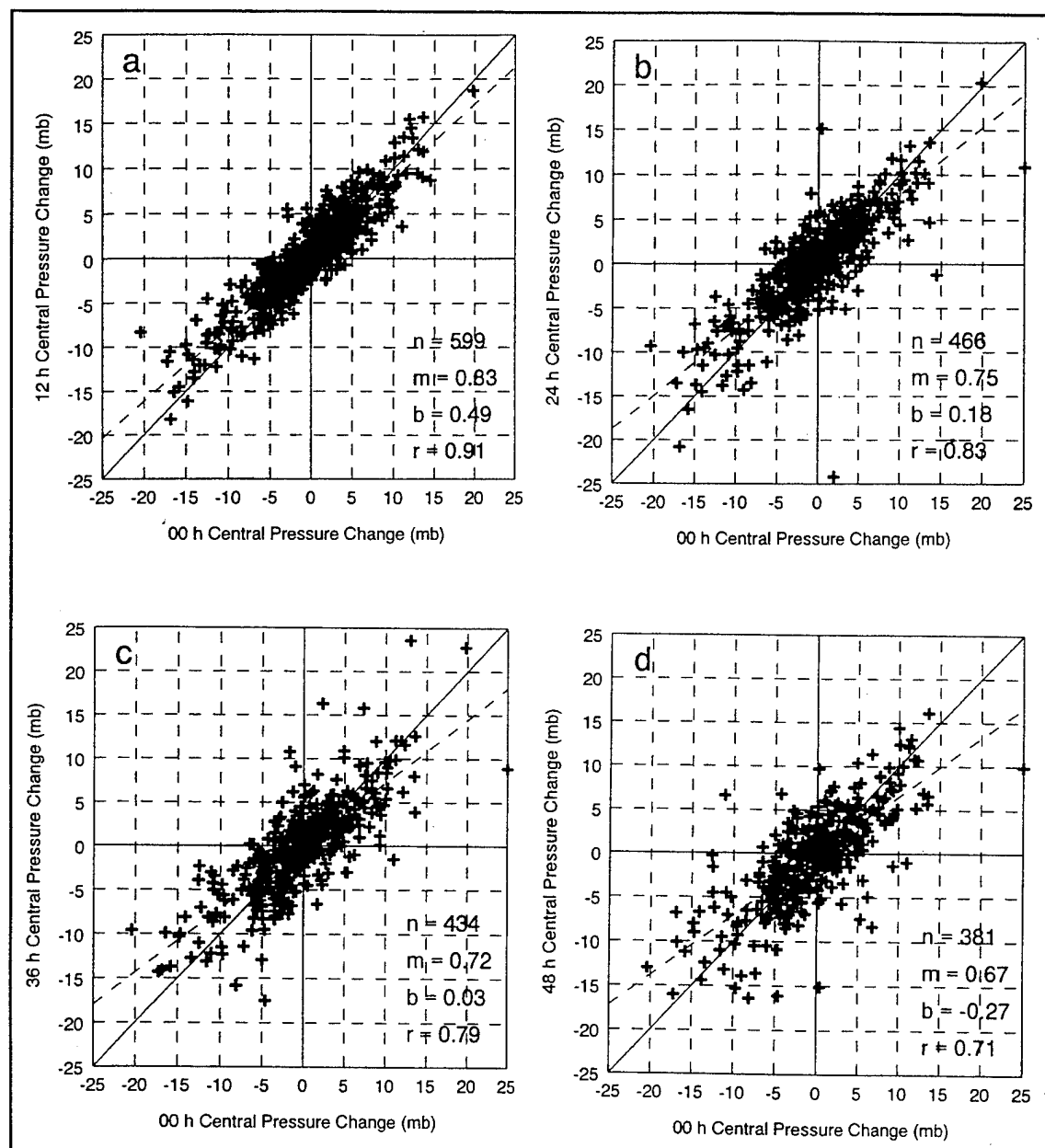


**Figure 70.** Scatter diagrams depicting Eta model analyzed (00 h) cyclone 12 h central pressure change vs forecast values; (a) 12 h forecast; (b) 24 h forecast; (c) 36 h forecast; and (d) 48 h forecast.

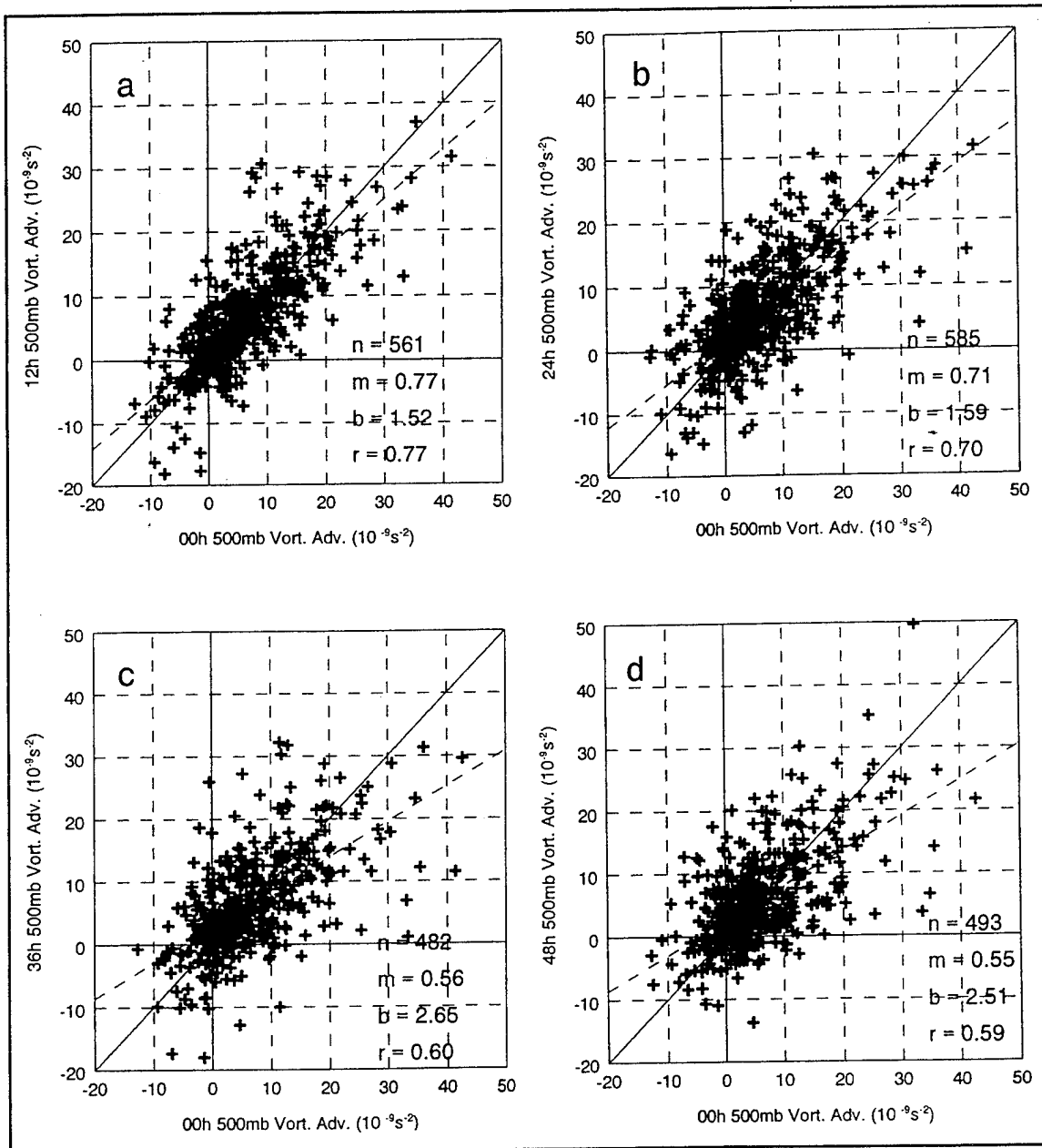


**Figure 71.** Scatter diagrams depicting Eta model analyzed (00 h) cyclone-average vorticity advection vs forecast values; (a) 12 h forecast; (b) 24 h forecast; (c) 36 h forecast; and (d) 48 h forecast.

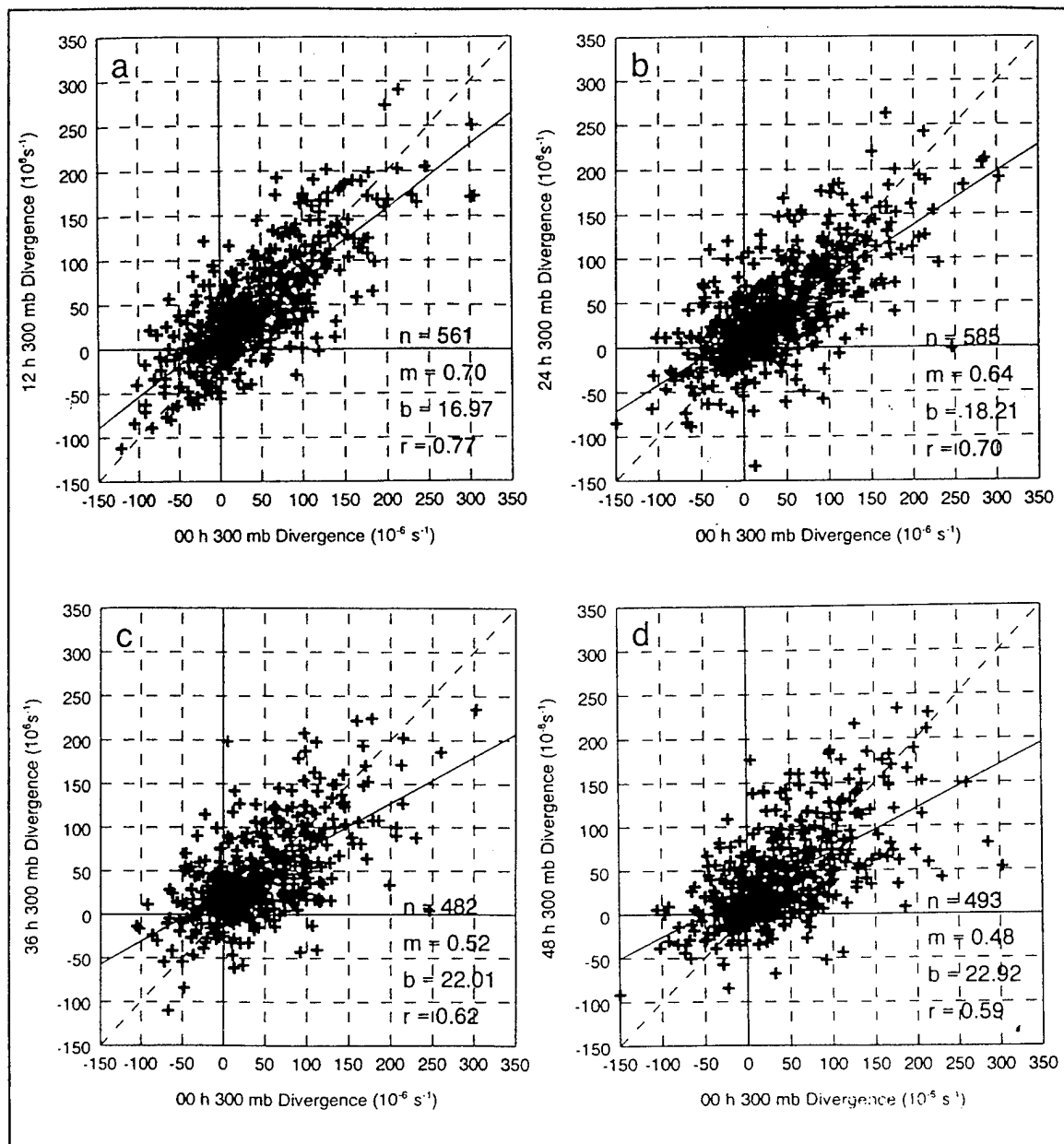


**Figure 72.** Scatter diagrams depicting Eta model analyzed (00 h) cyclone-average total divergence vs forecast values; (a) 12 h forecast; (b) 24 h forecast; (c) 36 h forecast; and (d) 48 h forecast.

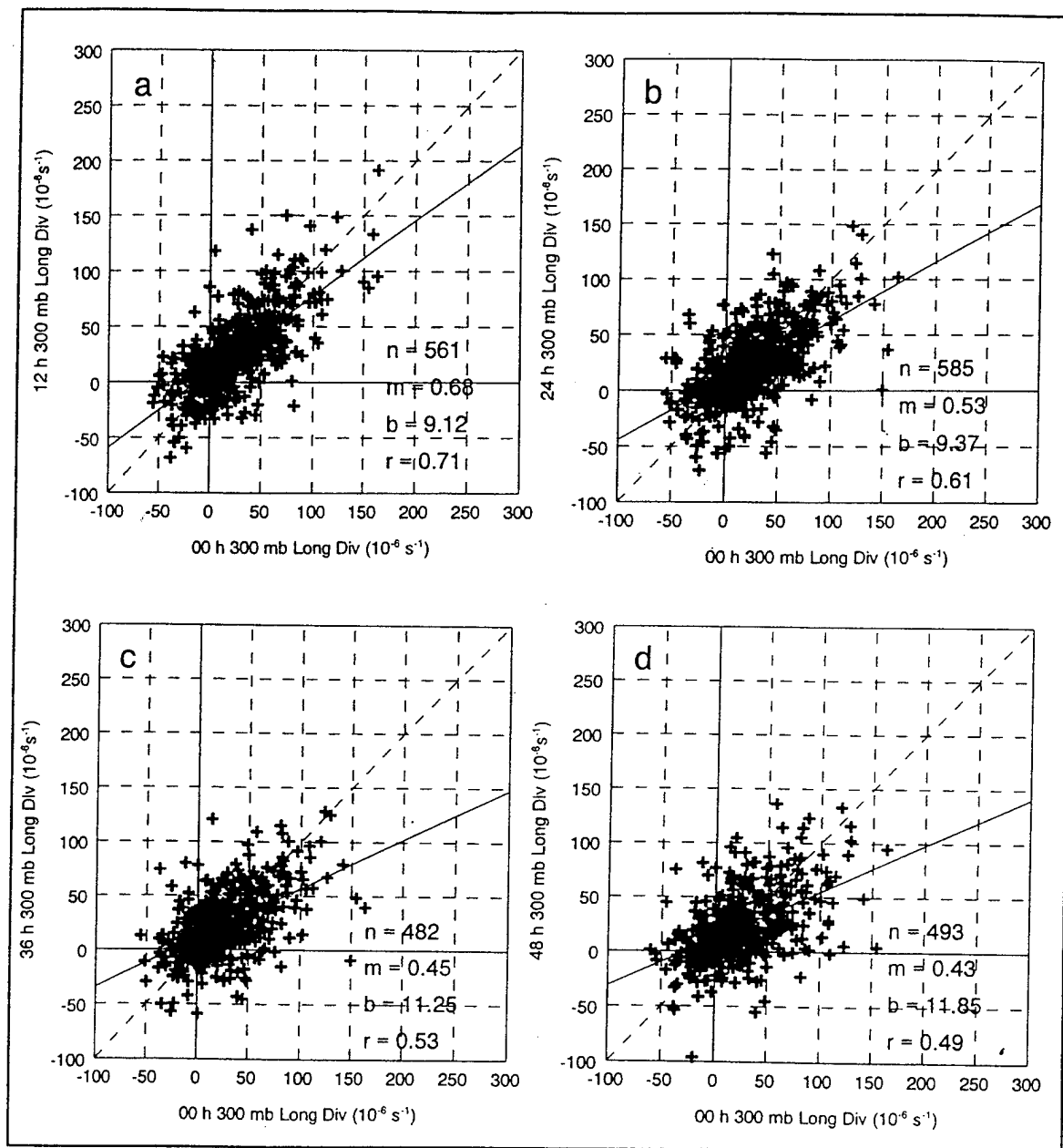


**Figure 73.** Scatter diagrams depicting Eta model analyzed (00 h) cyclone-average longitudinal divergence vs forecast values; (a) 12 h forecast; (b) 24 h forecast; (c) 36 h forecast; and (d) 48 h forecast.

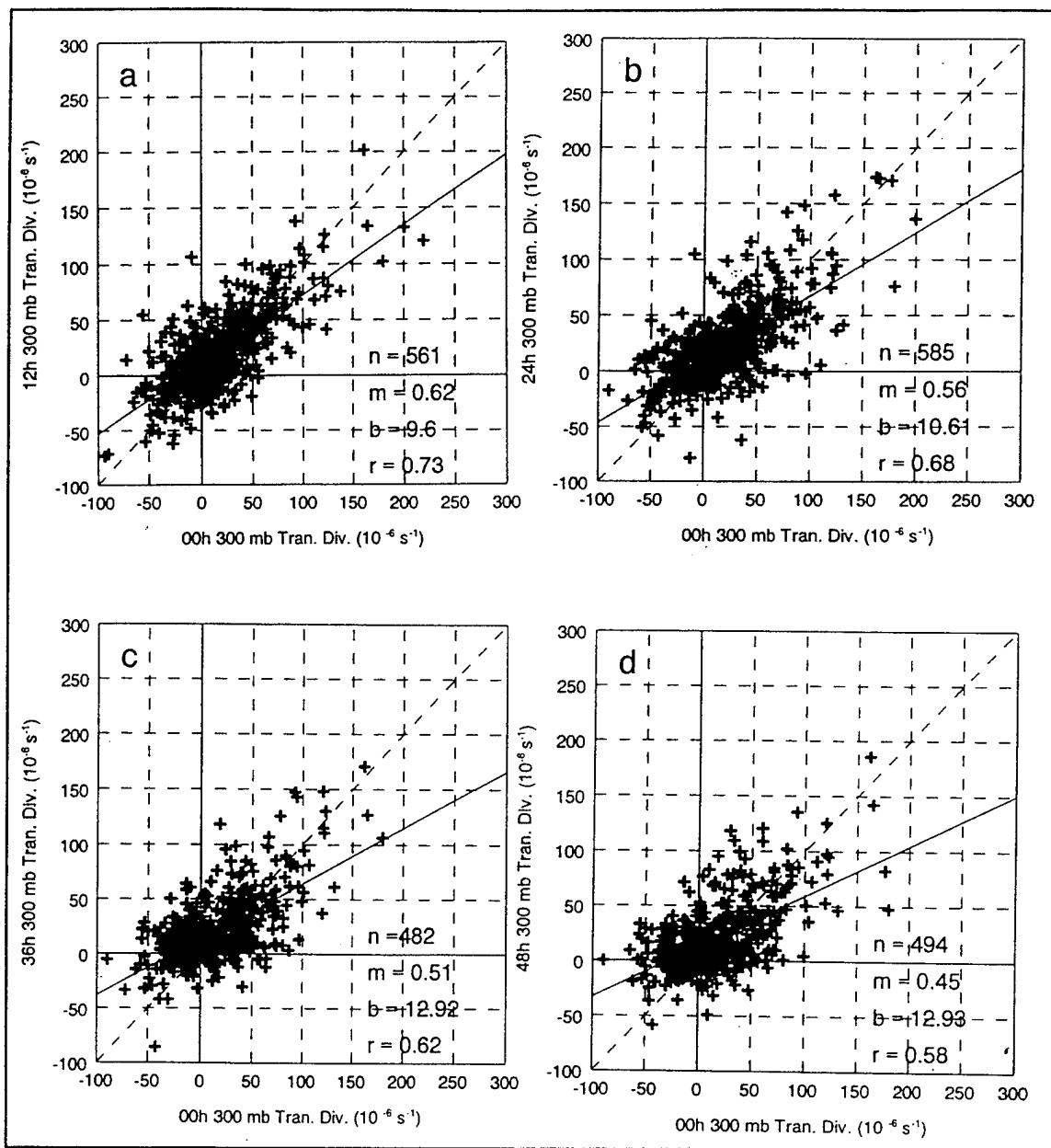


**Figure 74.** Scatter diagrams depicting Eta model analyzed (00 h) cyclone-average transverse divergence vs forecast values; (a) 12 h forecast; (b) 24 h forecast; (c) 36 h forecast; and (d) 48 h forecast.



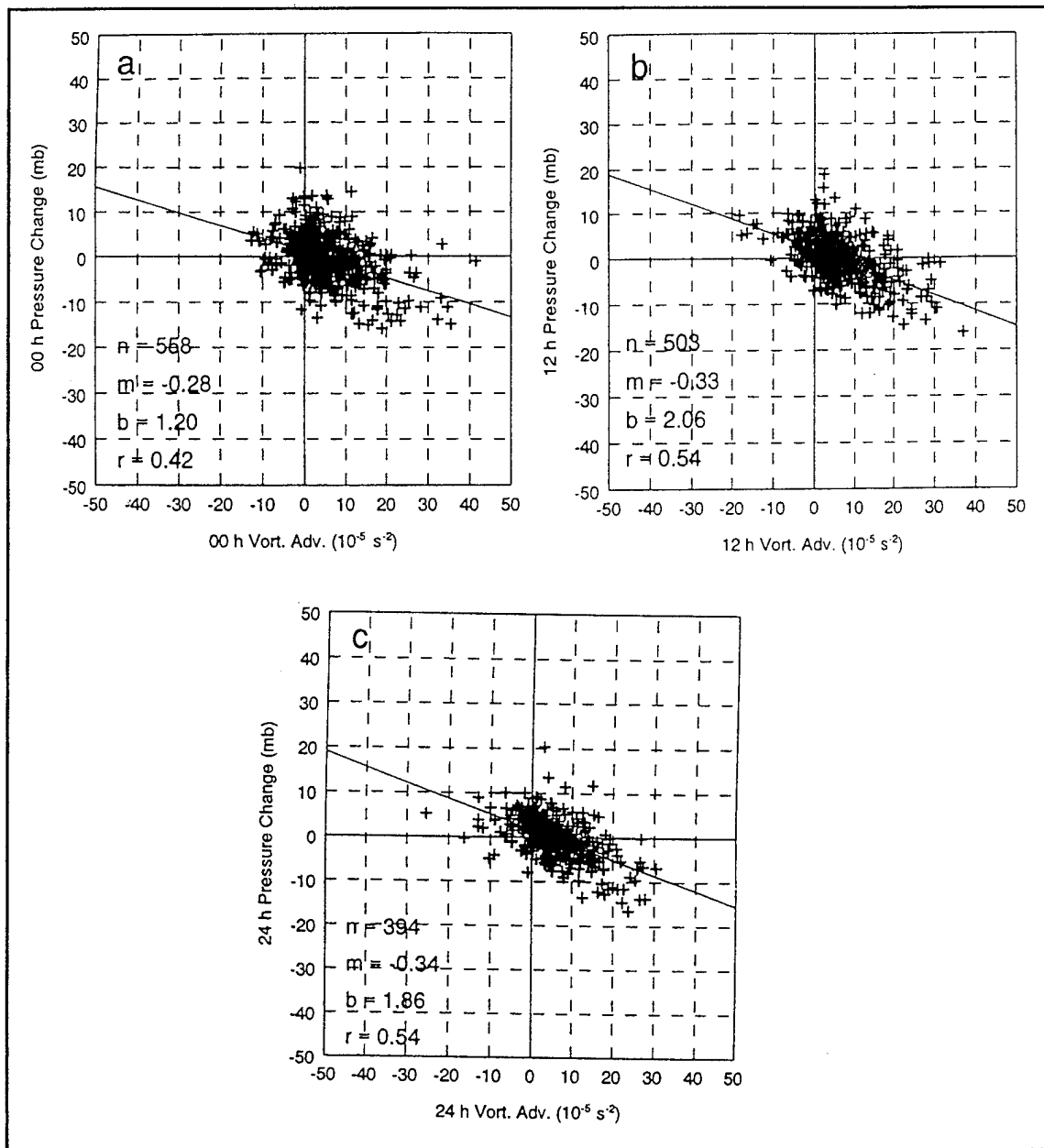


**Figure 75.** Scatter diagrams depicting Eta model cyclone-average vorticity advection vs 12 h central pressure change; (a) 00 h initialized analysis; (b) 12 h forecast; (c) 24 h forecast; and (d) 36 h forecast; (e) 48 h forecast.

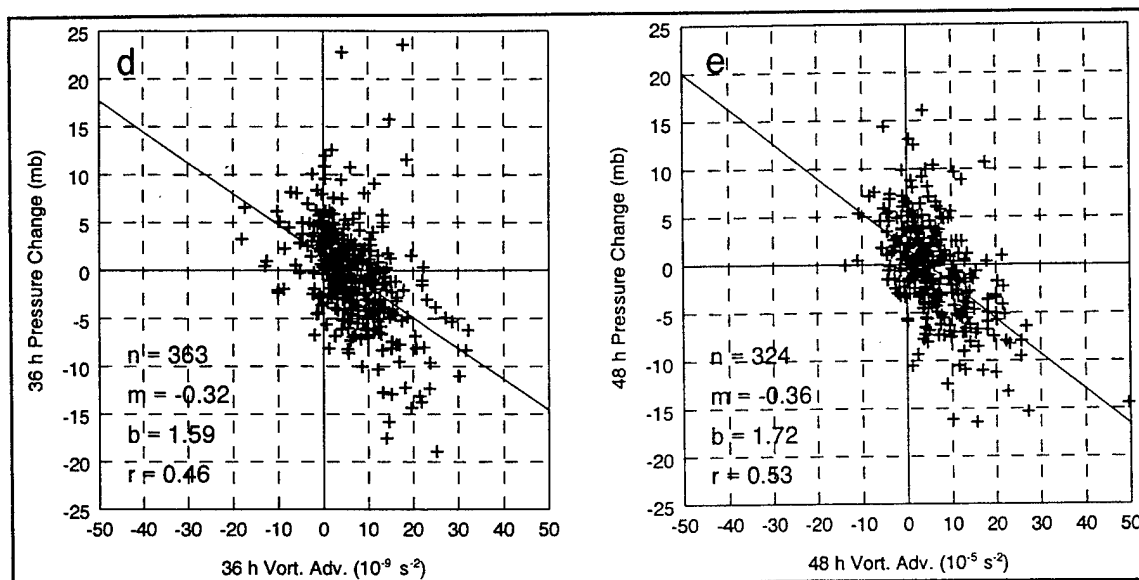


**Figure 75.** Continued.

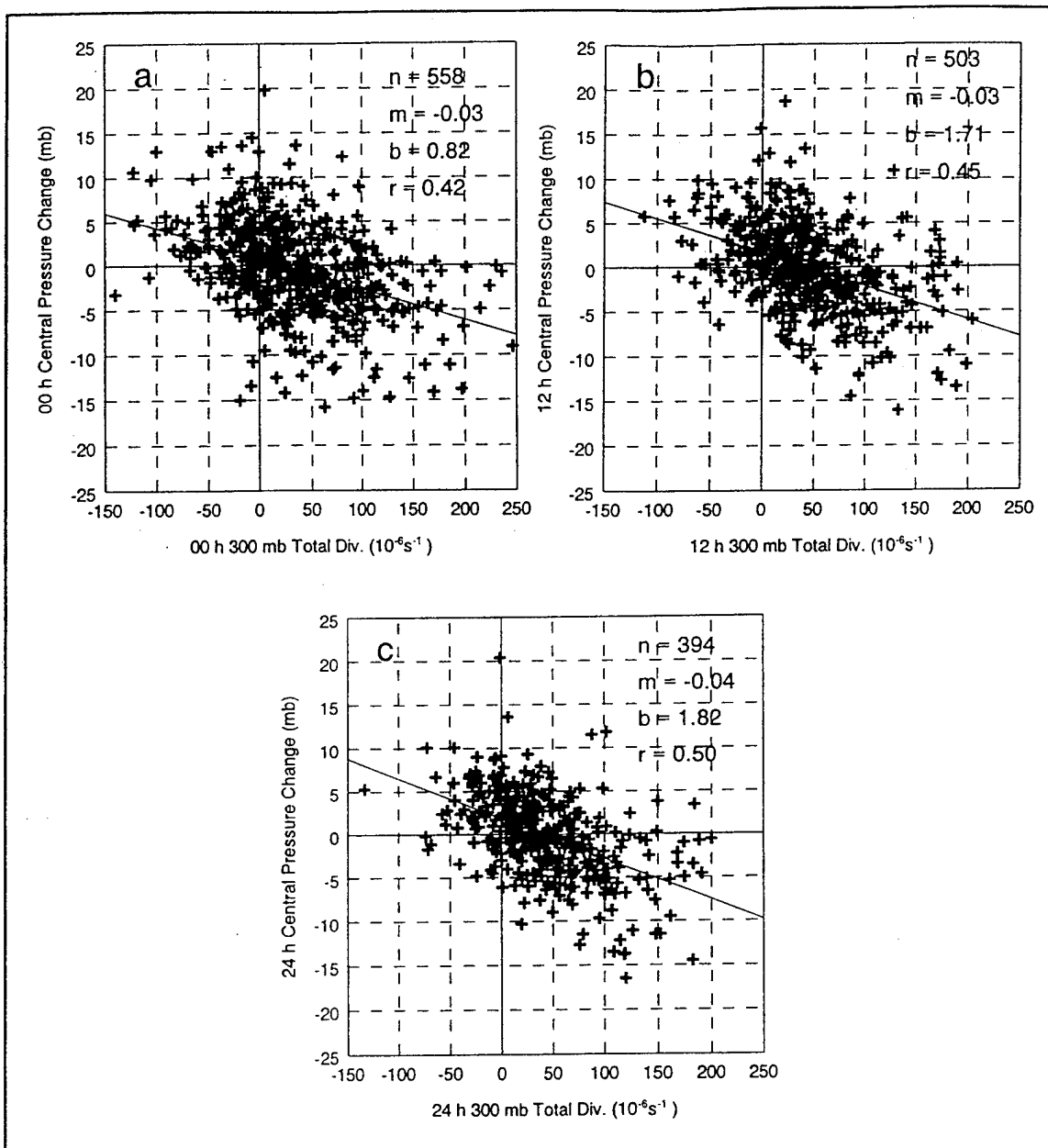


**Figure 76.** Scatter diagrams depicting Eta model cyclone-average total divergence vs 12 h central pressure change; (a) 00 h initialized analysis; (b) 12 h forecast; (c) 24 h forecast; and (d) 36 h forecast; (e) 48 h forecast.

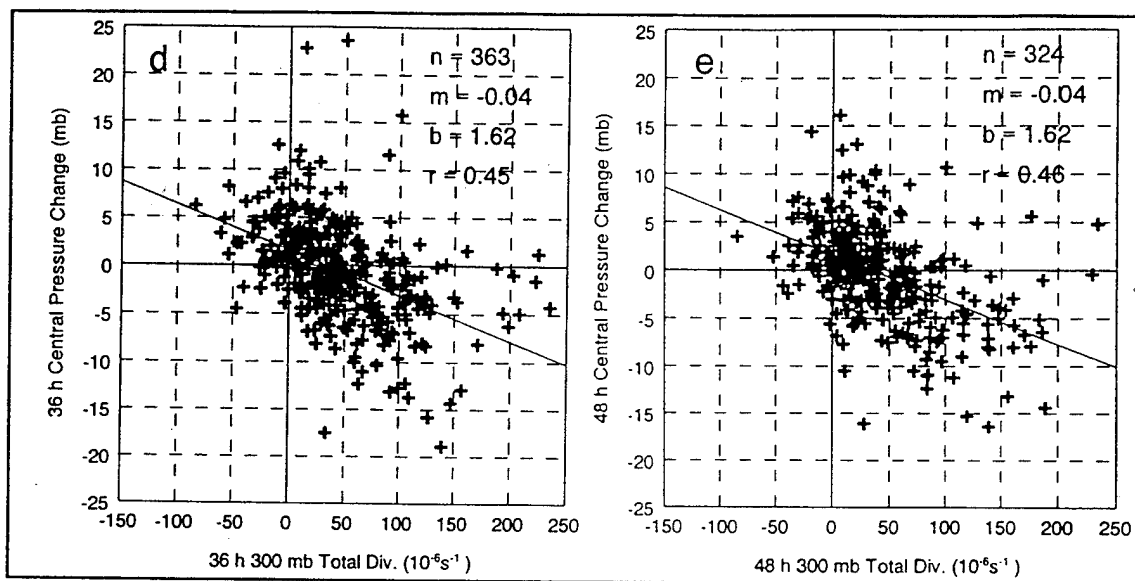
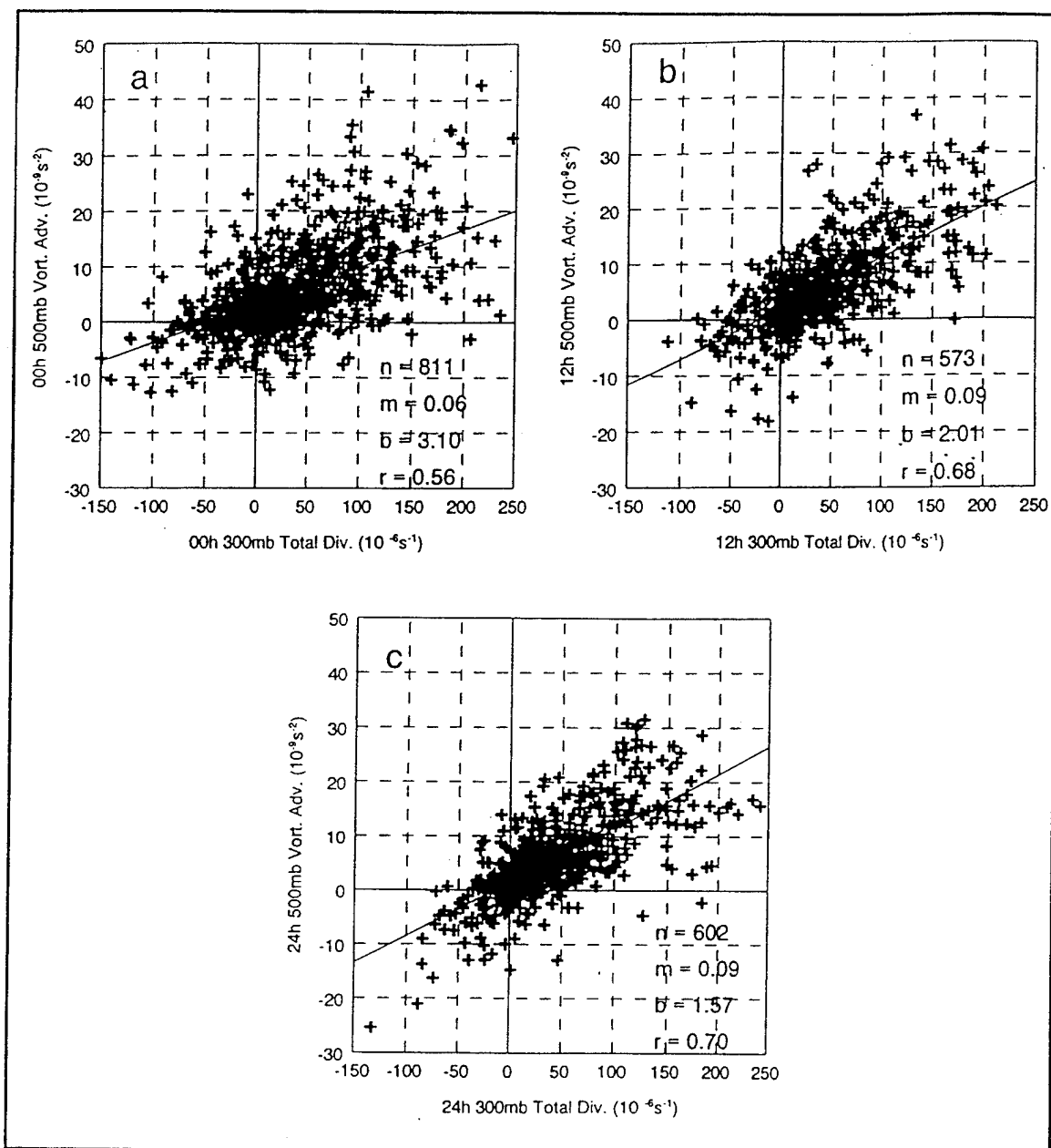


Figure 76. Continued.



**Figure 77.** Scatter diagrams depicting Eta model cyclone-average total divergence vs cyclone-average vorticity advection; (a) 00 h initialized analysis; (b) 12 h forecast; (c) 24 h forecast; and (d) 36 h forecast; (e) 48 h forecast.

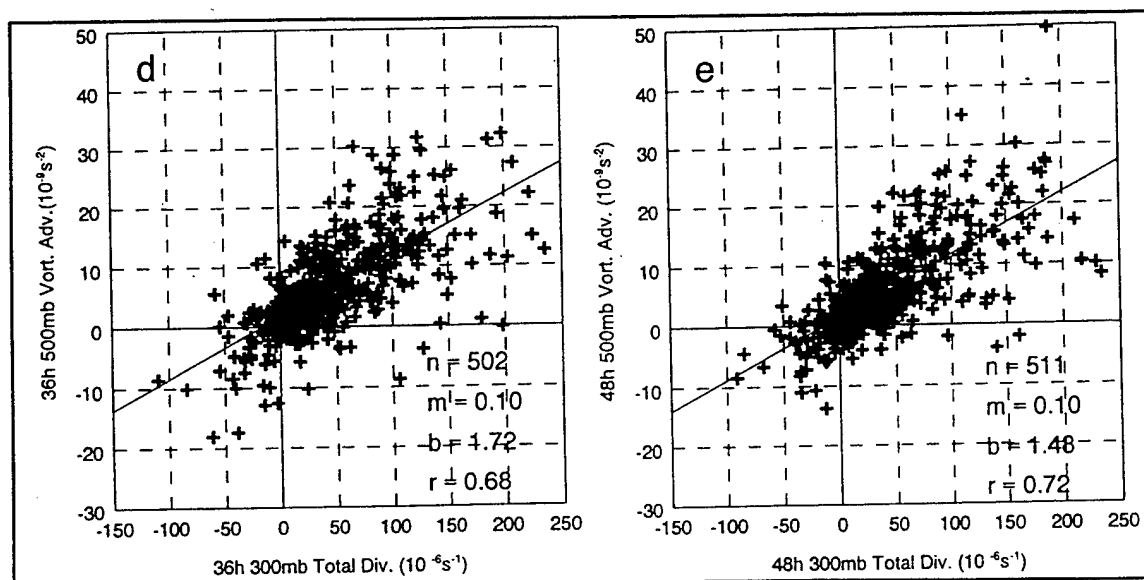
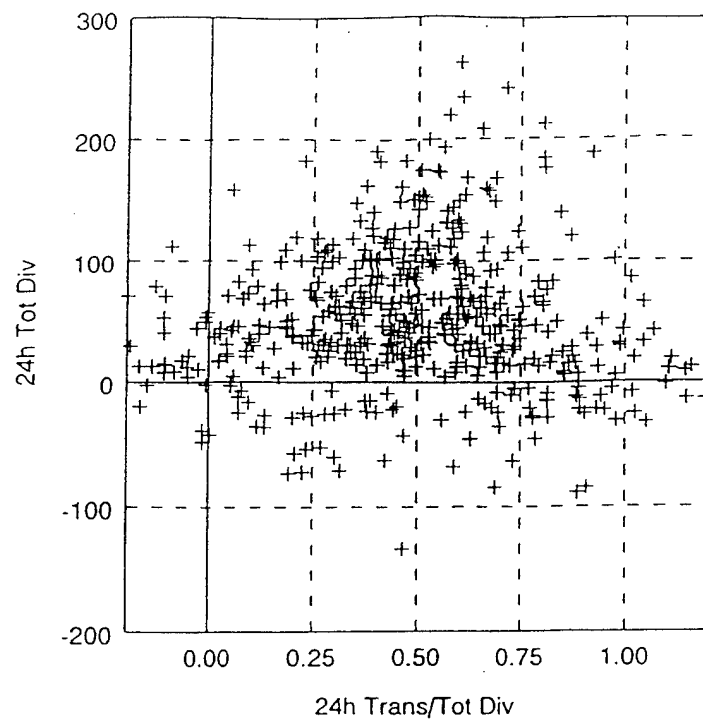
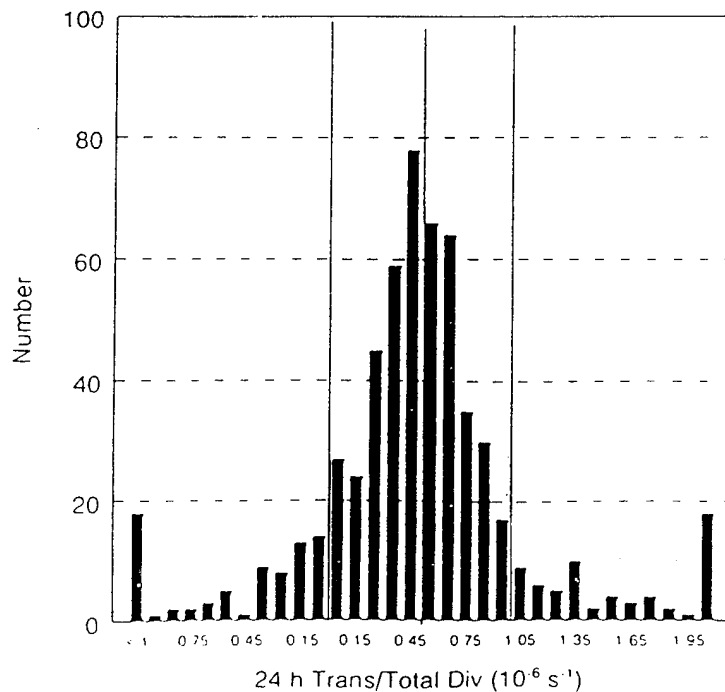


Figure 77. Continued.



**Figure 78.** Scatter diagram depicting the 24 h forecast ratio of transverse divergence to total divergence vs total divergence values.



**Figure 79.** Histogram depicting the 24 h forecast ratio of transverse divergence to total divergence vs total number of points.

## LIST OF REFERENCES

- Achter, T.H., and L.H. Horn, 1985: Spring season Colorado cyclones. Part I: Use of composites to relate upper and lower tropospheric wind fields. *J. Climate Appl. Meteor.*, **25**, 732-743.
- Bjerknes, J., and J. Holmboe, 1944: On the theory of cyclones. *J. Meteor.*, **1**, 1-22.
- Black, T., D. Deaven, and G. DiMego, 1993: The step-mountain eta coordinate model: 80 km 'early' version and objective verifications. *Technical Procedures Bulletin* **412**. Development Division, National Meteorological Center, World Weather Building, Washington, DC 20233.
- Colucci, J.W., 1994: A comparison of model performance between the Nested Grid and Eta models. M.S. Thesis, Naval Postgraduate School, 18-20 pp.
- Haltiner, G.J., and F.L. Martin, 1957: *Dynamical and Physical Meteorology*, McGraw-Hill, 311, 388 pp.
- Haltiner, G.J., and R.T. Williams, 1980: *Numerical Prediction and Dynamic Meteorology*, 2nd Ed., John Wiley and Sons, 17 pp.
- Keyser, D., B.D. Schmidt, and D.G. Duffy, 1989: A technique for representing three-dimensional vertical circulations in baroclinic disturbances. *Mon. Wea. Rev.*, **117**, 2463-2494.
- Loughe, A.F., C.-C. Lai, and D. Keyser, 1994: A technique for diagnosing three-dimensional ageostrophic circulations in baroclinic disturbances on limited-area domains. *Mon. Wea. Rev.*, **123**, 1476-1504.
- Sanders, F., and J.R. Gyakum, 1980: Synoptic-dynamic climatology of the "bomb". *Mon. Wea. Rev.*, **108**, 1589-1606.
- Uccellini, L.W., 1990: Processes contributing to the rapid development of extratropical cyclones. *Extratropical Cyclones: The Erik Palmén Memorial Volume*, C. Newton and E.O. Holopainen, Eds., Amer. Meteor. Soc., 81-105.
- Uccellini, L.W., and P.J. Kocin, 1987: The interaction of jet streak circulations during heavy snow events along the East Coast of the United States. *Weather and Forecasting*, **2**, 289-308.



Wash, C.H., R.A. Hale, P.H. Dobos, and E.J. Wright, 1991: Study of explosive and nonexplosive cyclogenesis during FGGE. *Mon. Wea. Rev.*, **120**, 40-51.

## INITIAL DISTRIBUTION LIST

		No. Copies
1.	Defense Technical Information Center 8725 John J. Kingman Rd., STE 0944 FT Belvoir, VA 22060-6218	2
2.	Library, Code 13 Naval Postgraduate School Monterey, CA 93943-5122	2
3.	Meteorology Department Code MR/CO Naval Postgraduate School 589 Dyer Rd Rm 252 Monterey, CA 93943-5122	1
4.	Oceanography Department Code OC/CO Naval Postgraduate School 589 Dyer Rd Rm 252 Monterey, CA 93943-5122	1
5.	Dr. Patricia M. Pauley Code MR/PA Naval Postgraduate School 589 Dyer Rd Rm 252 Monterey, CA 93943-5122	4
6.	Dr. Wendell A. Nuss Code MR/NU Naval Postgraduate School 589 Dyer Rd Rm 252 Monterey, CA 93943-5122	1
7.	LT Erika L. Sauer, USN OPS/OA Division USS BelleauWood (LHA-3) FPO AP 96623-1610	2

- |     |                                                                                                                                   |   |
|-----|-----------------------------------------------------------------------------------------------------------------------------------|---|
| 8.  | Commander<br>Naval Meteorology and Oceanography Command<br>Stennis Space Center<br>MS 39529-5001                                  | 1 |
| 9.  | Commanding Officer<br>Naval Oceanographic Office<br>Stennis Space Center<br>MS 39529-5001                                         | 1 |
| 10. | Commanding Officer<br>Fleet Numerical Meteorology and Oceanography Center<br>7 Grace Hopper Ave Stop 1<br>Monterey, CA 93943-5001 | 1 |
| 11. | Superintendent<br>Naval Research Laboratory<br>7 Grace Hopper Way Stop 2<br>Monterey, CA 93943-5502                               | 1 |